FABRICATION AND CHARACTERIZATION OF METAL NANOSTRUCTURES AND GRAPHENE NANOLAYERS AND THEIR APPLICATION IN OPTICAL SENSING

MEZHER H MEZHER

INSTITUTE OF GRADUATE STUDIES
UNIVERSITY OF MALAYA
KUALA LUMPUR

2018

FABRICATION AND CHARACTERIZATION OF METAL NANOSTRUCTURES AND GRAPHENE NANOLAYERS AND THEIR APPLICATION IN OPTICAL SENSING

MEZHER H MEZHER

THESIS SUBMITTED IN FULFILMENT OF THE REQUIREMENTS FOR THE DEGREE OF DOCTOR OF PHILOSOPHY

INSTITUTE OF GRADUATE STUDIES
UNIVERSITY OF MALAYA
KUALA LUMPUR

2018

UNIVERSITY OF MALAYA

ORIGINAL LITERARY WORK DECLARATION

Name of Candidate: MEZHER H MEZHER

Matric No: HHE 130008

Name of Degree: Doctor of Philosophy

Title of Thesis ("this Work"):

Fabrication and Characterization of Metal Nanostructures and Graphene Nanolayers and Their Application in Optical Sensing

Field of Study: Photonic Engineering

I do solemnly and sincerely declare that:

(1) I am the sole author/writer of this Work;
(2) This Work is original;
(3) Any use of any work in which copyright exists was done by way of fair dealing and for permitted purposes and any excerpt or extract from, or reference to or reproduction of any copyright work has been disclosed expressly and sufficiently and the title of the Work and its authorship have been acknowledged in this Work;
(4) I do not have any actual knowledge nor do I ought reasonably to know that the making of this work constitutes an infringement of any copyright work;
(5) I hereby assign all and every rights in the copyright to this Work to the University of Malaya ("UM"), who henceforth shall be owner of the copyright in this Work and that any reproduction or use in any form or by any means whatsoever is prohibited without the written consent of UM having been first had and obtained;
(6) I am fully aware that if in the course of making this Work I have infringed any copyright whether intentionally or otherwise, I may be subject to legal action or any other action as may be determined by UM.

Candidate's Signature Date:

Subscribed and solemnly declared before,

Witness's Signature Date:

Name:

Designation:

FABRICATION AND CHARACTERIZATION OF METAL NANOSTRUCTURES AND GRAPHENE NANOLAYERS AND THEIR APPLICATION IN OPTICAL SENSING

ABSTRACT

We present a study of optical characteristics of metal and graphene oxide nano-layers and their application in optical sensing. The nano-layers are coated using different approaches such as electron beam evaporation, electrochemical deposition and drop casting technique. Gold and silver nanoparticle layers were fabricated using electron beam evaporation followed by subsequent thermal annealing at different temperature and duration to achieve de-wetting of the metal thin film. Morphological analysis was carried out to study the shape and size of the produced nanoparticles. The gold and silver nanoparticles have sizes ranging from 11 nm to 45 nm and 15 nm to 54 nm, respectively. Meanwhile, bilayer Au/Ag-NPs have also been fabricated with particle size in the range between 23nm and 26 nm. On the other hand, the effects of nanostructures were studied using silver micro-flowers (Ag-MFs) with sizes of ~150-500 nm and platinum 'dome-like' nanostructures (Pt-NSs). Absorption spectroscopy was carried out to study the Surface Plasmon Resonance (SPR) of the nanoparticle layers. The shape and size of the nanoparticles are observed to affect the shifting of SPR wavelengths. Nonlinear optical properties was obtained for different structures of nano-layers using Z-scan technique. The nonlinear refractive index and nonlinear absorption coefficient of the nano-layers were determined. The Au-NPs show increase in the NLA and NLR with the increase in nanoparticle size. Meanwhile, The Au/Ag-NPs exhibit NLA and NLR between Au-NPs and Ag-NPs. The nonlinear optical properties of Ag-MFs with increase the size of microflower show increase in the NLA and NLR. Due to thermal effect, nonlinear absorption and nonlinear refraction index are not constant

values and depend on the incident intensity. Increases the intensity that apply on Pt-NSs show reduce NLA and NLR value and also for nitrogen doped graphene show reduce in NLA and NLR when increase the incident intensity. From the state of increasing the incident intensity can decreasing in the NLR due to thermal nonlinearity. The GO show increase in NLA and NLR with the increase in thickness. Selected nano layers (Platinum and Graphene oxide) are applied on optical waveguides for detection the water content in transformer oil. Pt-NPs coated planar waveguide sensor shows the sensitivity to dissolved water in transformer oil of -0.561 dB/ppm, while Pt-NPs coated D-Fiber sensor shows a sensitivity of -0.88 dB/ppm. GO have been coated on planar waveguide and D-Fiber to measure the water content in transformer oil. Depending on the GO coating thickness, the sensitivity range from 0.3 dB/ppm of water content in transformer oil to 1.86 dB/ppm of water content in transformer oil. The stability of the sensor output is inversely proportionate to the sensitivity, meaning there is a compromise between the two parameters when considering devising optical sensors in this configuration. The GO-coated waveguide sensor is further tested with continuous varying water content in transformer oil using a fluidic channel structure, and the result shows that the sensor is able to discern changes in water content in transformer oil in simulated environment.

Keywords: nonlinear, nanolayers and optical waveguide

FABRIKASI DAN PENCIRIAN NANOSTRUKTUR LOGAM DAN NANOLAPISAN GRAFIN DAN APLIKASINYA DALAM PENDERIAAN OPTIK

ABSTRAK

Kami membentangkan ciri-ciri kajian optik lapisan nano logam dan grafin oksida serta aplikasinya dalam penderiaan optik. Lapisan nano disalut menggunakan pendekatan yang berbeza seperti penyejatan hentaman elektron, pemendapan elektrokimia dan teknik pemutus jatuh. Lapisan- lapisan nanopartikel emas dan perak telah dibuat menggunakan penyejatan hentaman elektron diikuti oleh penyepuhlindapan haba seterusnya pada suhu dan jangka masa yang berlainan untuk mencapai penyebaran filem logam yang nipis. Analisis morfologi dijalankan untuk mengkaji bentuk dan saiz nanopartikel yang dihasilkan. Nanopartikel emas dan perak mempunyai saiz antara 11 nm hingga 45 nm dan 15 nm kepada 54 nm. Sementara itu, dua lapisan Au / Ag-NP juga telah direka dengan saiz zarah di antara 23 dan 26 nm. Sebaliknya, kesan struktur nano dikaji dengan menggunakan bunga mikro perak (Ag-MFs) pada saiz ~ 150-500 nm dan struktur nano-struktur seperti 'kubah' platinum (Pt-NSs). Penyerapan spektroskopi telah dijalankan untuk mengkaji lapisan nano-partikel Permukaan Plasmon Resonan (SPR). Bentuk dan saiz nanopartikel diperhatikan sekiranya ia memberi kesan kepada peralihan gelombang SPR. Ciri optik tidak linear diperolehi untuk struktur lapisan nano yang berbeza yang menggunakan teknik Z-scan. Indeks bias tidak linear dan pekali penyerapan tidak linear lapisan nano telah ditentukan. Nano-partikel emas, Au-NPs menunjukkan peningkatan dalam NLA dan NLR dengan peningkatan saiz nano-partikel. Sementara itu, Au / Ag-NPs mempamerkan NLA dan NLR antara Au-NP dan Ag-NPs. Sifat optik bukan linear Ag-MFs meningkatkan saiz peningkatan mikrobunga dalam NLA dan NLR. Oleh kerana kesan haba, penyerapan tidak linear dan indeks pembiasan tidak linear bukan nilai malar dan bergantung kepada intensiti sewaktu kejadian.

Peningkatan intensiti yang berlaku pada Pt-NSs menunjukkan pengurangan nilai NLA dan NLR juga grafin yang diletakkan nitrogen telah mengurangkan NLA dan NLR apabila intensiti kejadian ditingkatkan. Dari peningkatan intensiti kejadian dapat menurunkan NLR oleh kerana termal yang tidak linear. GO menunjukkan peningkatan pada NLA dan NLR dengan bertambahnya ketebalan. Lapisan nano yang dipilih (Platinum dan Grafin oxide) digunakan pada pandu gelombang optik untuk mengesan kandungan air dalam minyak pengubah. Pandu gelombang yang bersalut Pt-NPs menunjukkan kepekaan kepada air larut dalam minyak pengubah sebanyak -0.561 dB / ppm, manakala Pt-NPs bersalut sensor gentian-D menunjukkan kepekaan -0.88 dB / ppm. GO telah menyaluti pandu gelombang dan gentian-D bagi mengukur kandungan air dalam minyak pengubah. Bergantung pada ketebalan salutan GO, kepekaan berkisar dari 0.3 dB / ppm kandungan air dalam minyak pengubah kepada 1.86 dB / ppm kandungan air dalam minyak pengubah. Kestabilan sensor pada pengeluaran adalah berkadar songsang dengan kepekaan, bermakna terdapat kompromi antara kedua-dua parameter apabila mempertimbangkan penciptaan sensor optik dalam konfigurasi ini. Sensor pandu gelombang GO-bersalut terus diuji dengan kandungan air yang berlainan yang berbeza dalam minyak pengubah dengan menggunakan struktur saluran cecair dan hasilnya menunjukkan bahawa sensor dapat melihat perubahan dalam kandungan air dalam minyak pengubah dalam persekitaran yang telah disimulasi.

Kata Kunci: tidak linear, lapisan nano dan pandu arah optik

ACKNOWLEDGEMENTS

The accomplishment of this work required a lot of guidance and assistance from many people and I am extremely fortunate to have got this all along the completion of my research work. Whatever I have done is only due to such guidance and assistance and I would not forget to thank them. Alhamdulillah, all praises be to Allah the almighty God who has put me in this beautiful journey of life and has given me the strength to keep me going on through this work until the end.

A special appreciation goes to my supervisor, Dr. Rozalina Zakaria, for giving me an opportunity to do this project under her supervision in PhD level. She has provided all the support and guidance that I need to dedicatedly work on this research. I feel very lucky and grateful to have an endless support from Dr. Chong Wu Yi. As another supervisor of mine he always helps me a lot in many ways in making sure that I can keep doing my research smoothly.

I am grateful to my research group mates, Dr Khairus Syifa Hamdan, Siti Munirah Che Noh, Kam Wern and Ong Yong Sheng who would always lend a hand whenever I need their help either in my work or for moral support. I would also like to thank my new lab members, Fatimah, Aina'a, Wani, Afiqah and CK who always share constructive ideas on my research journey. I would like to give special thanks to my friends from outside of my university Soh kum you, Dr Abu Ebudah, Dr Haneen Abdwahab and special thanks to my lovely family in Malaysia specially Fanny wong and her family.

I am thankful to and fortunate enough to get constant encouragement and moral support from my family especially my parents, Haimed Mezher and Eltfat Abbas, my oldest brother Ali and Laith, my oldest sister shymaa and afya, my youngest brother Haider . Who always keep tabs on my research progress and give endless moral support throughout my PhD work.

TABLE OF CONTENTS

LIST OF FIGURES

LIST OF TABLES

LIST OF SYMBOLS AND ABBREVIATIONS

Ag	:	Silver
AgNPs	:	Silver Nanoparticles
Ag-MFs	:	Silver micro flower
Au	:	Gold
AuNPs	:	Gold Nanoparticles
Pt	:	Platinum
Pt-NSs	:	Platinum nanostructures
Pt-NPs	:	Platinum nanoparticles
Au/AgNPs	:	Gold and Silver Nanoparticles
GO	:	Graphene Oxide
FESEM	:	Field emission electron scanning microscopy
UV/VIS	:	Ultraviolet/Visible
NIR	:	Near Infrared
SPR	:	Surface Plasmons Resonance
EDX	:	Energy dispersive X-ray
λ_0:	:	wavelength of light in free space
θ n_{Core}	:	refractive index of core
$n_{Cladding}$:	:	refractive index of cladding
B	:	nonlinear absorption
n_2	;	nonlinear refraction
EDX	:	Energy dispersive X-ray
L	:	sample thickness
L_{eff}	:	Effective thickness of the sample
w_o	:	Beam waist

CHAPTER 1: INTRODUCTION

1.1 A Brief History of Nanotechnology

Nanotechnology -Art and the science of manipulating atoms and molecules to create new system, materials, and devices where unique phenomena observed at this scale enable many novel applications. The concept of nanotechnology was first proposed by Richard Zsigmondy (1925 Nobel Prize Laureate). He had made detailed studies on gold hydrosols and other nanomaterials with sizes down to 10 nm using an microscope which was capable of visualizing particles at much smaller than the light wavelength (Bhushan, 2017; Sattler, 2010). Modern nanotechnology was the brain child of Richard Feynman, winner of the 1965 Nobel Prize Physics. During 1959 American Physical Society meeting at California Institute of Technology (Caltech), he presented a lecture entitled, ‘‘There’s Plenty of Room at the Bottom’’, in which he introduced the concept of manipulating matter at the atomic scale (Hulla, Sahu, & Hayes, 2015; Romer, 1993). This novel idea demonstrated new ways of thinking and Feynman’s hypotheses have been proven right. This is the reason why he is considered to be the father of modern nanotechnology. 15 years after Feynman’s lecture, a Japanese scientist, Norio Taniguchi, used a word of ‘‘nanotechnology’’ to describe semiconductor processes that occurred at the nanometer scale. He proposed that nanotechnology should consist of the processing, separation, consolidation and deformation of materials by one atom or one molecule. (The nanotechnology at golden era began in the 1980s when Kroto, Smalley and Curl discovered fullerene and Eric Drexler from Massachusetts Institute of Technology (MIT) manipulating ideas from Feynman’s famous lecture and Taniguchi’s term nanotechnology in his 1986 book titled, “Engines of Creation: The Coming Era of Nanotechnology”).

Drexler interpretation of nanotechnology was based on the idea of an “assembler” which is able to build a copy of itself and other items of arbitrary complexity. Drexler’s vision of nanotechnology is often called “molecular nanotechnology”. nanotechnology science has achieved a major milestone with the development of carbon nanotube (CNT) by Iijima et al. in the year 1991 (Iijima, 1991). Since then, development of nanotechnology has been seen tremendous pace with the fabrication of many nanomaterials including graphene, metal nanoparticles and carbon nanotubes.

1.2 Enabling Technology for Nanoscience

Nanotechnology represents a rather broad interdisciplinary field of research and industrial activity involving particles with sizes of less than 100 nm. Nanoparticles are the most fundamental component in the fabrication of nanostructures and are much smaller than most objects in our everyday life typically described by Newton’s laws of motion (Horikoshi & Serpone, 2013). These nanoscale particles can be tubular (nanotubes), spherical, or irregularly shaped, and may also exist in aggregated forms. Such small particles have properties that are different from their conventional bulk forms and can affect their physical, chemical, and biological behavior. Metallic nanoparticles, for example, have different physical and chemical properties from bulk metals (e.g., lower melting points, higher specific surface areas, specific optical properties, mechanical strengths, and specific magnetizations); these properties have proven attractive in various industrial applications. Few examples are given below (Sargent Jr, 2016) such as:

- Nanoparticles can be used in electrical applications. For example, copper nanoparticle suspensions have been developed as a safer, cheaper and more reliable alternative to lead-based solder and other hazardous materials commonly used to fuse electronics interconnections in the assembly process.
- Nanoparticles can be used in medicine and healthcare for diagnosis and treatment. For example, gold nanoparticles can be used to diagnose lung cancer from exhaled breath and cancer treatment by mediated dermal therapies.
- For environmental remediation, nanoparticles are being developed to purify industrial water pollutants in groundwater through chemical reactions.
- In the oil and gas sector, nanotechnologies are used to improve oil and gas extraction by reducing energy consumption and reducing toxicity burdens on the environment. Examples include the use of nanotechnology-enabled gas lifts valves in offshore operations and nano-drilling fluids as high-temperature lubricants. In addition, nanoparticles are also enabling to detect microscopic down-well oil pipeline fractures and environmental remediation.

In addition, nanotechnology plays an important role in the evolution of today's information technology, homeland security, medicine, energy, food safety and environmental science. There is increasing number of commercial products currently in the market and in daily use that rely on nanomaterials and many inventions to be produced (Sargent Jr, 2016).

1.3 Nanotechnology in Photonics

Nanophotonics is one of the three main branches of nanotechnology as shown in Figure 1.1. It involves the study of light interaction at Nanometer scale particles or structures. These include the fabrication of these structures, the determination of their physical and optical properties, and their utilization in different applications (Ghoshal, Sahar, Rohani, & Sharma, 2011).

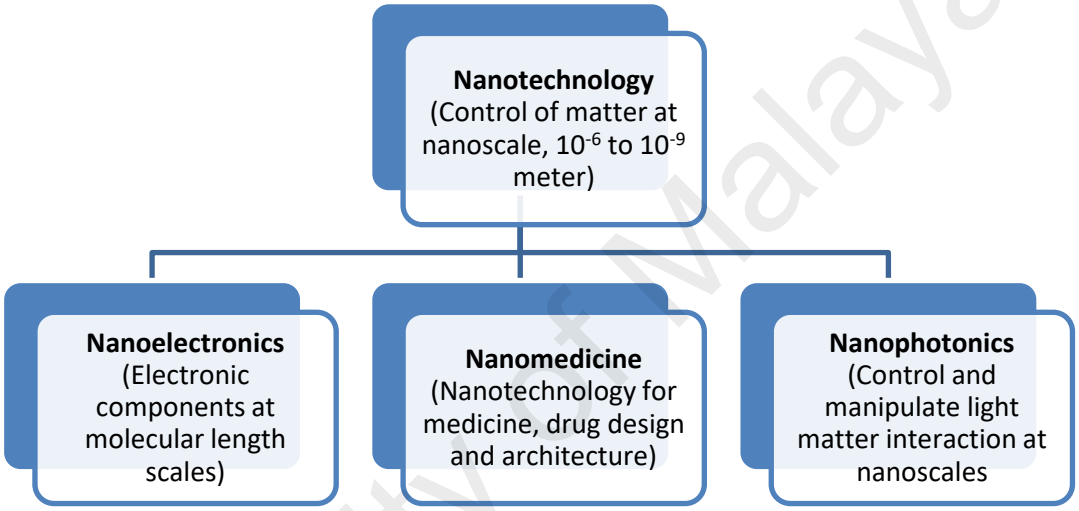

Figure 1.1: Block diagram depicting three main branches of nanotechnology (Ghoshal et al., 2011).

Nanophotonics concerns the investigation of building, manipulating and characterizing optically active nanostructures. Nanophotonics is an enabling technology that has the potential of impacting across a wide range of photonics application ranging from high efficiency solar cells, optical sensors, lasers, optoelectronic chips, optical communication and optical microscopy (E. L. Hu, Brongersma, & Baca, 2011). Figure 1.2 shows the classification of nanophotonics into three main physical phenomena, namely confinement of matter, confinement of radiation/photon, photo processes and synthesis at nanometer scale (Ghoshal et al., 2011).

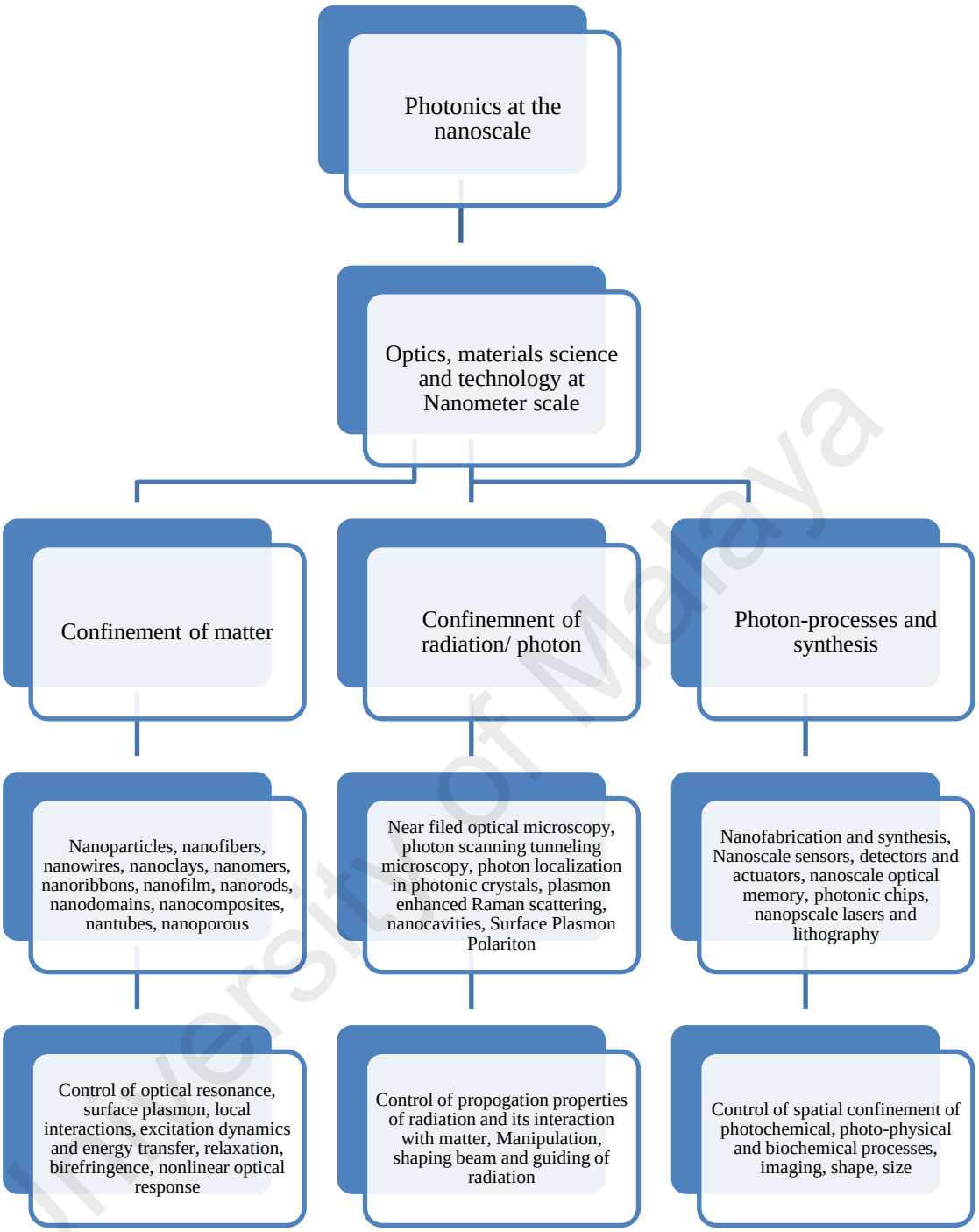

Figure 1.2: A block diagram representing various major processes and techniques of nanophotonics (Ghoshal et al., 2011).

Almost any materials (metal, organic, semiconductor, organo-metallic, polymers and dielectric) can be used to fabricate nanomaterials. In this work, focus will be given to the study of metal- and carbon-based nanomaterials and their applications in photonics technologies. The studies include the fabrication, characterization and application of nano-particle excited surface plasmon polaritons, while the extensive studies will focus on the study of optical properties of graphene-based 2D materials in sensor applications.

1.4 Surface Plasmon Resonance (SPR)

Surface plasmon resonance (SPR) is the collective oscillations of the free electron gas in metals that exist at the interface between two materials with different dielectric constants, such as a metal and a dielectric (Jiří Homola, 2006). When the propagation constant of the excitation photons match that of the electron oscillations, SPR will occur. The SPR excitation occurs by transferring the energy from incident light to metallic nanostructures. Over the past few decades, researchers have shown immense interest in the study of (SPR). A chronological event of important developments in SPR research is given in Table 1.1. SPR was first discovered by Wood in 1902 (Wood, 1902), where he found that when polarized light was shone on a mirror with a diffraction grating on its surface (a reflection grating), an anomalous pattern of dark and bright band is observed in the reflected light. In 1907, Zenneck (Zenneck, 1907) showed that radio waves include a solution of Maxwell's Equations which travels without a change in pattern over a flat surface bounded by two homogeneous media at different conductivity and dielectric constants. When the upper medium is air and the lower medium is a homogeneous dissipative ground, the wave is characterized by a phase velocity greater than the light and a small attenuation appeared in the direction along the interface. Furthermore, the surface wave's phenomena is highly attenuated height above the surface (Norton, 1937).

In 1909, Somerfield observed that the field amplitudes of the surface waves present on the metal dielectric interface vary inversely with the square root of the distance from the source dipole (Norton, 1937). In 1941, Fano concluded theoretically that the anomalies reported by Wood (in 1902) were due to the excitation of surface waves on the surface of diffraction grating (Fano, 1941; Lalanne & Liu, 2013). Ritchie, Powell and Swan is also observed that electrons can excite surface plasmon at the metal dielectric interface (Stefan A Maier, 2007; Powell & Swan, 1960). Stern and Ferrell has also revealed that the electromagnetic waves at the metallic surface involved electromagnetic radiation coupled to the surface plasmons (Stern & Ferrell, 1960). The end of the sixties saw the application of SPR excitation for optical sensing. Two prism-based configurations, the Otto configuration and Kretschmann configuration, was developed (Kretschmann, 1971; Andreas Otto, 1968). In 1980, Nylander et al, demonstrated that SPR generation in the Kretschmann configuration is well suited for both gas and biomolecular sensing (Liedberg, Nylander, & Lundström, 1995; Liedberg, Nylander, & Lunström, 1983; Luong, Male, & Glennon, 2008). This demonstration was later developed into a commercial system by Pharmacia Biosensor (Sweden) (BIA core for GE Healthcare, USA) in 1990 (Lundström, 2014). Cullen et al., on the other hand, advocated the use of metal-coated diffraction grating for SPR sensing to achieve field enhancements around the grooves and allow efficient conversion of evanescent waves into evanescent wave are radiation (Cullen, Brown, & Lowe, 1987). In 1988 Markatos proposed the first fiber-based SPR sensing by etching an optical fiber cladding to expose the fiber core and then depositing a gold thin metal layer on the etched core surface. Two years later, Villuendas and Palayo further developed the fiber-based SPR sensors to achieve high sensitivity and dynamic range in the measurement of sucrose concentration in aqueous solution (Villuendas & Pelayo, 1990).

Table 1.1: Major milestones of SPR development.

Year	Major milestones	Remarks
1902	Williams Wood observed that when polarized light incident on a *diffraction* grating, an anomalous pattern of dark and bright bands appears in the reflected light (Wood, 1902) .	The first observation of surface plasmon.
1907	Jonathan Adolf Wilhelm Zenneck. Theoretically formulated a special surface wave solution of the Maxwell's Equations and predicted that radio frequency surface electromagnetic waves occur at the interface of a lossy dielectric or a metal and a lossless dielectric (Zenneck, 1907).	Theoretically studied the boundary conditions between two different media.
1909	Arnold Johannes Wilhelm Sommerfeld. Found that the field amplitudes of surface waves postulated by Zenneck varied inversely as the square root of the horizontal distance from the source dipole (Norton, 1937; A Sommerfeld, 1909).	Improvement on Zenneck's model.
1941	Fano. Concluded that the anomalies reported by Wood (1902) were due to excitation of surface waves on the surface of the diffraction grating (Fano, 1941).	Explanation to Wood's observations in 1902.
1957	Richie Ashburn. First coined the word "surface plasmon" and demonstrate theoretically that surface Plasmon could be excited on the surface of thin metal film by interact with photon.	Theoretical prediction of the excitation of surface plasmons using thin film coated on prism
1960	Powell and Swan. They observed the excitation of surface plasmons at the metal surface using electrons(Powell & Swan, 1960).	Excitation of surface plasmons.
After 1960	Stern and Ferrell. They concluded that the electromagnetic waves at the metallic surface possessed electromagnetic radiation intermingled with surface plasmons (Gramotnev & Bozhevolnyi, 2010; Stern & Ferrell, 1960).	Cooperation of surface plasmons.
1968	Prism-based SPR configurations.	Principle SPR sensor and excitation of SPR
1971	Grating-based SPR configuration.	Other types of SPR configuration.
1980	Nylander and Liedberg et al, They demonstrated that SPR in the Kretschmann-configuration was well suited for both gas and biomolecular sensing purposes and many other application	SPR sensor application
1988	Markotas. Proposed SPR sensor by etching the cladding to expose the core and deposit a thin layer on the core.	Optical fiber base SPR sensor
1990	Villuendas and Palayo proposed development of fiber-optic SPR sensors. They presented the experimental results for sensitivity and dynamic range in the measurement of sucrose	Developing optical fiber base SPR sensor
After 1990	Cullen et. advocated The application of metallic diffraction for SPR sensing	Grating base SPR sensor

1.5 Application of SPR in sensing

SPR sensor technology has been produced in 1990 and SPR biosensors have become a central tool for characterizing and quantifying biomolecular interactions, most notably to determine association and dissociation kinetics, protein-ligand, protein-protein, or nucleic acid hybridization interactions (Daghestani & Day, 2010; Mao et al., 2011). The applications of SPR-based biosensors range from laboratory assays for immunoreactions measurements, to continuous or spot monitoring in food industries and monitoring of environmental pollutants and agents of bioterrorism (Bahadır & Sezgintürk, 2015; da Costa Silva, dos Santos, Salgado, & Pereira, 2013). The sensing principle is based on SPR sensors capability of measuring minute changes in refractive index (RI) with a high precision.

Pioneering works of SPR sensing was carried out by Kretschmann et al. (Erwin Kretschmann & Heinz Raether, 1968) and Otto (Andreas Otto, 1968) in the late 1960s. They demonstrated that optical excitation of Surface Plasmon Resonance (SPR) can be achieved by bringing into contact a thin layer of metallic structure with a dielectric surface, e.g. the surface of a prism. SPR excitation is dependent wavelength as well as on the dielectric constants of the two materials (Jiří Homola, Yee, & Gauglitz, 1999).

There are two prism-based SPR configurations as shown in Figure 1.3:

- The Otto configurations, where a prism is brought into contact with a metal thin film for SPR excitation. A thin metal film (for example gold) is positioned close enough to the prism surface where total internal reflection (TIR) occurs so that an evanescent wave can interact with the plasma waves on the metal thin film to excite the surface plasmons. The sensing media is placed in metallic substrate. This configuration is useful in the study of SPR in solid phase media due to lower refractive index medium between metal and prism surface. However, the

gap between the total internal reflection (TIR) surface and metal thin film causes the SPR efficiency to be relatively low (Andreas Otto, 1968; A Otto, 1968).

- The Kretschmann configuration, which is an improvement from the Otto configuration. It has the metal thin film coated directly on the TIR surface of prism to eliminate the gap and to enhance the SPR sensitivity (Erwin Kretschmann & Heinz Raether, 1968).

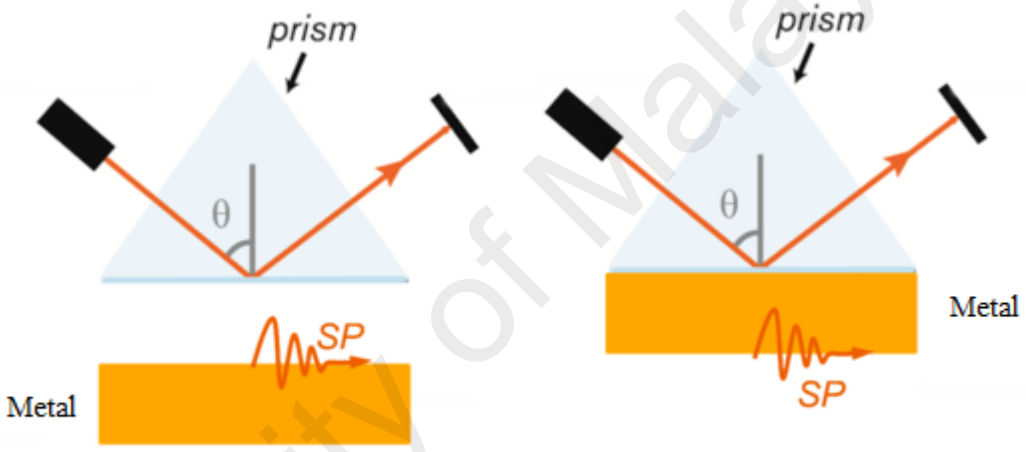

(a) Otto configuration (b) Kretschmann configuration

Figure 1.3: SPR sensors based on (a) Otto configuration and (b) Kretschmann configuration (Erwin Kretschmann & Heinz Raether, 1968; Yanase et al., 2014).

The principle of SPR sensing is based on the resonance angle where reduced light reflected intensity at some particular angle of incidence which is known as resonance angle. This resonance angle is very sensitive to any difference of the refractive index on the sensing medium. The small change in the refractive index will alters resonance condition significantly.

There are two sensing mechanisms:

- The angular interrogation method is known as the dielectric constant of the sensing medium is obtained by changing the incidence angle of the incident light and keeping the wavelength of the light fixed (Gupta, Shrivastav, & Usha, 2016; Gupta & Verma, 2009; Jiří Homola, 2003; Sharma, Jha, & Gupta, 2007).
- The spectral interrogation (wavelength interrogation) method, in which the wavelength of the light beam is varied while the angle of incidence fixed. In the spectral interrogation method, white light from a polychromatic source is launched on the metal layer through the prism at a particular angle of incidence greater than the critical angle.

Despite their successes conventional prism-based SPR sensor has number of limitations. Some of the drawbacks that prevent optimization and commercialization on a large scale include the bulk size of the prism and the presence of various optical and mechanical. In addition, remote sensing cannot be realized using prism based SPR sensing device. These short comings have spurned the efforts towards the development of optical fiber and planar waveguide based SPR sensors. The miniaturization of the SPR probe can be achieved using optical fiber due to their capability to confine light into a small volume. Furthermore, fiber optic SPR sensing offers simplified optical design and the capability for remote sensing. Other advantages inherent from the fiber optic sensor (FOS) technologies include: immediate response, compact size, high levels of safety, high stability, advances, flexibility, and are the ability to operate in harsh environments. Meaningful efforts have been taken since the year 1977 (Cole, Johnson, & Bhuta, 1977) by research groups around the world to develop (non-SPR-based) optical fiber–based sensing system for the purpose of simultaneous monitoring of multi-parameters, such as in strain, temperature, vibration and refractive index (Cusano,

Cutolo, & Giordano, 2008; Qazi, Mohammad, Ahmad, & Zulkifli, 2016). The fiber-based SPR sensors was first demonstrated in 1988.

1.6 Principles of SPR generation

SPR is generated at a metal-dielectric interface. Light interaction with a metal-dielectric interface is governed by the Equation $\varepsilon = 1 - \frac{\omega_p^2}{\omega^2}$, where ε the dielectric is constant; ω_p is the plasma frequency can be defined the highest frequency which electron could be able to respond with, being equal to highest for plasma too and ω the light frequency.

There are three different conditions:

1. Light with frequencies above the plasma frequency of the metal ($\omega > \omega_p$) so the dielectric constant will be positive. The electromagnetic wave will be transmitted through the interface because the electrons at the interface cannot respond fast enough to block it.
2. Light of frequencies below the plasma frequency of the metal ($\omega < \omega_p$) so the dielectric constant will be negative. The electromagnetic wave will be reflected at the interface, due to the exponentially decay of the electrons inside the metal.
3. When the light frequency equals plasma frequency ($\omega = \omega_p$), the collective oscillation appears as SPR.

The plasma frequency of metallic elements is usually situated in the ultraviolet spectrum, thus making most metals shiny (reflective) within the visible range (Bai et al., 2015; Diest, Liberman, Lennon, Welander, & Rothschild, 2013; Mubeen et al., 2012). To date, many new technologies explores the fascinating light-matter interaction of

SPR. Surface plasmons are very sensitive to the properties of the interfacing material due to their unique capacity in confining light to a very small dimension. The highly sensitive SPR response has enabled the development of many new applications.

1.7 SPR materials and their optical properties

Generally, a thin layer of gold and silver can be used as the SPR sensor due to their strong SPR absorption peaks in the visible region. Silver has a small value at the imaginary part of the dielectric constant, which gives a sharp resonance dip leading to better detection accuracy. On the other hand, gold is another option of metal. Though exhibiting less sensitivity than silver, it is more stable and does not oxidize over time. To combine the advantages of both metals into a single metallic layer can be extremely advantageous. Zynio et al. have proposed the idea of using a combination of gold and silver layers as a bimetallic coating for prism based sensors (Zynio, Samoylov, Surovtseva, Mirsky, & Shirshov, 2002). To enhance the sensitivity of SPR, a variety of metal nanostructures have been proposed and demonstrated. These nanostructures include metal diffraction gratings, micro-hole arrays and nanoparticle layers (Cai, Lu, Lin, Wang, & Ming, 2008; Couture, Zhao, & Masson, 2013).

1.8 Graphene Oxide – 2D nanomaterial

Exfoliation of graphene, the first practical production of a 2-D material, was reported in 2004 by Geim and Novoselov (Gibney, 2015; Novoselov, 2010). 2-D materials possess remarkable properties in their ability to be exceptionally strong, lightweight, flexible and is an excellent conductors of heat and electricity (Brownson & Banks, 2014). Graphene attracts significant attention for photo detection due to their strong interaction with photons in a wide range of energy and its high carrier mobility, making it a promising candidate for high speed applications in a broad wavelength range (Mak,

Ju, Wang, & Heinz, 2012; Xia, Wang, Xiao, Dubey, & Ramasubramaniam, 2014; Xia, Yan, & Avouris, 2013).

The synthesis of GO is relatively simple and cost effective. It's being with the chemical oxidation of graphite into graphite oxide using strong oxidizers such as sulphuric acid. This reaction is known as a redox (a portmanteau of reduction and oxidization) reaction, as the oxidizing agent is reduced and the reactant is oxidized. There are two general oxidation approaches of graphite into graphite oxide, namely the Brodie method and the Hummers method (Boehm & Scholz, 1965; Brodie, 1859; Hummers Jr & Offeman, 1958; Kovtyukhova et al., 1999; Marcano et al., 2010; You, Luzan, Szabó, & Talyzin, 2013). Graphite oxides demonstrate considerable variations in their properties depending on the degree of oxidation and the synthesis method (H. V. Kumar, Woltornist, & Adamson, 2016). For example, the temperature point of explosive exfoliation is generally higher for graphite oxide prepared by Brodie method compared to Hummers method, (Boehm & Scholz, 1965; You et al., 2013). The Hummers' method, developed by Hummers and Offeman in the year of 1957, is considered as safer, quicker, and more efficient compared to the Brodie method of synthesis use to a mixture of potassium permanganate and sulfuric acid sodium nitrate. The main difference between graphite oxide and graphene oxide is the inter-planar spacing between the individual atomic layers of the compounds caused by water intercalation. Graphite oxide is three dimensional, whereas graphene oxide is two dimensional. The oxidation process results in (space formation) and also disrupts the sp^2 bonding network, which means that both graphite oxide and graphene oxide are electrical insulators (Norazlina & Kamal, 2015).

GO is considered easy to process since it is dispersible in water (and other solvents). GO films can be deposited on essentially any substrate surfaces and reduced to

graphene. GO can be easily mixed with different polymers and other materials and enhance the properties of composite materials like tensile strength, elasticity, conductivity and more (Brownson & Banks, 2014). In solid form, GO flakes attach one to another to form thin and stable flat structures that can be folded, wrinkled and stretched. Such GO structures can be used for applications like hydrogen storage, ion conductors and nano-filtration membranes. GO is also fluorescent, which makes it especially appropriate for various medical applications such as bio-sensing and disease detection, drug-carriers and as antibacterial materials (Brownson & Banks, 2014; Kosasih, 2012). In addition, GO coating has been used in numerous sensing applications such as hydrogen sulfide gas sensing, humidity sensor, and many more application (Dash & Jha, 2016; Rani, Kumar, Garg, Sharma, & Kumar, 2016).

1.9 Motivation

Although SPR sensing has been demonstrated almost two decades ago in the year 1968, most systems are in bulk form. This research aims to transfer the SPR sensing capability onto an optical waveguide platform to achieve high sensitivity and remote sensing. Planar waveguides and D-fibers will be used as platforms to study the applicability of SPR sensing. The sensing performance of the developed waveguide-based SPR sensor will be studied with the measurement of water content in transformer oil. As the water content limit in transformer oil must be less than 16 ppm, it presents a real challenge for such low-level detection. With the high sensitivity of SPR sensor and the fact that the dielectric constant of transformer oil changes with water content, this work aims to study and develop a practical remote sensor for transformer oil water content monitoring.

Distributed remote sensing, especially in cascaded sensing structures, presents a variation of power levels incident upon each sensing probe. Where high power is used,

there is a possibility of excitation of nonlinear optical effects, which may affect the accuracy of SPR measurement. Therefore, it is important to study the nonlinear optical properties of the nanomaterials used to determine the maximum power that can be applied on this sensor to avoid the excitation of these nonlinear effects.

1.10 Research Objectives

The objectives of this study have been designed to meet the motivation discussed the earlier section. The following is a list of the research objective for this study.

1. To investigate the physical and optical properties of different nanomaterials to be used for the development of optical sensors.
2. To design and characterize the performance of waveguide-based optical sensors using:
    - ❖ Planar waveguide.
    - ❖ Side polished optical fiber (D-shaped fiber).
3. To demonstrate waveguide-based optical sensing of water content in transformer oil.

1.11 Thesis Framework

This thesis comprises of seven chapters that begin with a brief introduction of general background of the research study, followed by the sub sections; motivation and objectives in the first chapter.

Chapter 2 provides a discussion of theory and literature review with an overview of the recent developments in the field of plasmonics, as well as a comprehensive introduction of both nonlinear, graphene and the optical sensors.

Chapter 3 presents a discussion of the techniques used in the fabrication and characterization of metal nanoparticles. This chapter also introduces materials used for this study with an outline on the experimental fabrication techniques and the procedure for optical characterization that are utilized in the present research work.

Chapter 4 reports on optical response of fabricated materials. This chapter also presents the overview introduction of optical response of metals nanoparticles of different sizes, shapes and space between the nanoparticles. Nonlinear optical properties have been carried out to investigate this nanoparticle effects.

Chapter 5 reports on the optical properties of arbitrarily shape of metallic structures at different sizes and thickness layer which involves in nonlinear optical studies.

Chapter 6 demonstrates the applications of an optical sensor that has been fabricated using side polished optical fiber and planar waveguide. The device has been constructed based on application of water detection in transformer oil using metallic nanostructures and graphene oxide.

Finally, the research work reported in this dissertation is summarized in Chapter 7.

CHAPTER 2: THEORY AND LITERATURE

2.1 INTRODUCTION

This chapter discusses theory and literature review related to the plasmonics field and the application as optical sensors. This chapter traces the historical development of the plasmonics field in terms of past theoretical consideration that has given rise in the past, along with a brief review of the physics underlying the plasmonics works in an optical system. This is followed by a brief overview of the principles of basic modes for the optical sensors. The operation of these devices is based on the excitations of surface plasmons at a metal-surface interface. Surface modes that propagate at metal-dielectric interfaces and surface plasmons (SPs), are known as surface plasmon polaritons (SPPs). The surface modes from an electromagnetic field together with oscillations of the conduction electrons on the metal surface will enhance the field associated with the SPPs. In the recent year, interest in research of Surface Plasmon Resonance (SPR) combined with a new technology that utilizes fascinating light-matter interaction at a metal -dielectric interface is growing at a rapid pace among researchers.

2.2 Plasmonics

Study of the interaction between electromagnetic field and free electrons in a metal and exploit surface plasmons to achieve optical properties which are not seen in nature. This field of study is to confine the light dimensions of electromagnetic fields at the order or smaller than the wavelength of light (Atwater & Polman, 2010).

The basic study of plasmonics is focused into the interaction process of electromagnetic radiation with the conduction electrons in the metallic boundaries ranging from corrugated surfaces to structures in nanometres. Consequently, the plasmons which are confined in nanoparticles can lead to enhance optical near-field of sub-wavelength dimensions. As such, scientists are encouraged to utilize this resonant

interaction to control light on a sub-wavelength scale in order to manipulate interactions between light and matter. In other words; the concept of plasmonics is a description of meta-based optics in a scientific and technological manner.

The study of plasmonics as a field of science and technology is a new phenomenon, less than a decade old. Yet, the historical background in this field clearly traces back the two main ingredients of this field, namely surface plasmon polaritons and localized surface plasmons, back to 1900 (Adel, Alexandre, Xavier, Jean-Jacques, & Olivier; S. Maier, 2007). It is indeed important to appreciate the interlinked nature of numerous phenomena and applications involved in this field of study. Some research's works have been devoted to the theoretical study of electromagnetic surface modes on metal wires and calculation of the solutions of Maxwell's Equations for wave propagation along a cylindrical metal surface (Arnold Sommerfeld, 1952).

The findings revealed that surface modes are electromagnetically equivalent to surface plasmons polaritons in the visible domain. In 1908, Gustav Mie established a clear mathematical basis on light scattering of small spherical particles. Later, this concept was adopted by other researchers as the fundamentals for the description of localized surface plasmon resonances in metallic nanoparticles. By the exploitation of the surface, it is possible to achieve the localization of light at a nanometre scale. The infrared counterpart of surface plasmon resonance is considered as plasmon resonance in polar dielectrics. Meanwhile coupling between phonon and plasmon resonances can enhance infrared absorption as is known to be useful in application in such as near-field microscopy, imaging and sensing (Mandal & Chaudhuri, 2013).

2.3 Theoretical Considerations on Plasmonics

This section introduces three theoretical models; Mie, Gans, and Drude to emphasize on their importance to the field of plasmonics. This is followed by a description of surface plasmon and their dispersion relationship.

2.3.1 Mie Theory

Gustav Mie (1908) introduced the classical, but relatively simple and versatile. Mie theory describes the mechanism of light absorption by small metal particles through solving Maxwell's Equations, which the theory is based on the assumptions that successive induction of a charge separation on the surface of the particle which occurs electromagnetic field interacts with the particle. As a result of this charge separation, a there is an occurring restoring force. It has been found that varying geometrical and environmental factor causes the absorption of light by metallic particles in the ultraviolet-visible region. In the case of metallic nanoparticles, the use of Maxwell's Equations has resulted in a relationship of the cross-section extinction.

$$\sigma_{ext} = \sigma_{sca} + \sigma_{abs} \tag{2.1}$$

where σ_{ext}, σ_{sca} and σ_{abs} are the parameters extinction, scattering and absorption cross-section respectively.

Both absorption and scattering processes occur simultaneously. However, there are situations where either one of them dominate the process. Only absorption is significant when small particles are taken into consideration as compared to the wavelengths of light (particle radius $a \ll \lambda$). A complex expression is used for the dielectric constant:

$$\varepsilon(\omega) = \varepsilon'(\omega) + i\varepsilon''(\omega) \tag{2.2}$$

Where ε' and ε'' are the real and imaginary part of the dielectric function of the metallic

nanoparticles respectively, while ω is the angular frequency of the exciting radiation in accordance to the Drude model (Adel et al.; Jones, 1957; Stefan Alexander Maier, 2007; Sukharev & Nitzan, 2017). Based on the assumptions that the particles are spherical, small, and embedded in an isotropic and non-absorbing medium with a dielectric constant of $\varepsilon_m = n_m^2$, Mie solved the extinction cross section of such solution where by its "real part" is given by Equation. (2.3):

$$\varepsilon(\omega) = 9\frac{\omega}{c}\varepsilon_m^{\frac{3}{2}}V_o\frac{\varepsilon''(\omega)}{[\varepsilon'(m)+2\varepsilon_m]^2+\varepsilon''(m)^2} \quad (2.3)$$

Where $V_o = (4/3)a^3$ is the volume for spherical nanoparticle, c is the vacuum velocity of light, and ε_m is the dielectric constant of the host medium. Equation 2.3 determines the line shape of the absorption band of the particles. The bandwidth and height of peak are well approximated by $\varepsilon''(\omega)$. Maximum absorption occurs when $\varepsilon'(\omega) \approx -2\varepsilon_m$. Assuming that $\varepsilon''(\omega)$ is small value or $\varepsilon''(\omega)$ is only slightly dependent on ω. Nevertheless, are experimental result has shown that size dependence is observable to the theory (U. Kreibig & Genzel, 1985; Uwe Kreibig & Volmer, 1995; Link & El-Sayed, 1999; Mulvaney, 1996). Again, from Equation 2.3, two limiting cases can be deduced for which σ_{ext} is equal to zero. In the first case, when the complex part of the dielectric constant is zero $\varepsilon'(\omega) = 0$, it mean the particle is non-absorbing. This is a suitable feature for application in dielectric materials. In other condition of $\varepsilon''(\omega) \rightarrow \infty$, it means that the material reflects all incoming radiation at this wavelength.

2.3.2 Gans Theory

Richard Gans (1912) modified Mie's theory, to include the expression for the extinction cross-section of spheres to ellipsoidal particles (M. Hu et al., 2006). This modified expression has enabled Gans to calculate for the absorption resonance of rod-like nanoparticles. However, it is mandatory to consider two fundamental oscillation

directions for the conduction electrons due to ellipsoidal shape. The first oscillation direction is along the short axis of the ellipsoid while the second one is along the long axis. Since both oscillations induce a charge separation; the occurrence of a localized plasmon resonance in the nanoparticle is sensitive. Hence, the extinction cross-section proposed by Gans is considered an ellipsoid dimension that fulfils the condition: $a > (b = c)$ show in Figure 2.1.

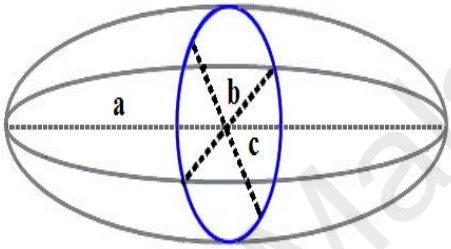

Figure 2.1: Schematic of an ellipsoidal particle with dimensions: $a > b = c$, where a, is the dimension of the longitudinal axis, b and c are the dimensions of the transverse axes.

These modifications for ellipsoidal nanoparticles give rise to two possible plasmon modes (longitudinal and transverse). The longitudinal mode is strongly dependant on the aspect ratio. For the case of many metals, the absorption region that is up to the bulk plasma frequency, ω_p, is dominated by the free electron behaviour. Thus, the dielectric response is well described by the simple Drude model, as introduced in the following section.

2.3.3 Drude Model

In 1900 Paul Drude, a German physicist introduce a new and bold theory of electrical and thermal conduction of metals. The application of this theory is based on the successful kinetic theory of gases to metal, then has been considered as a gas of

electrons (Drude, 1900a, 1900b). The assumption of Drude's model is the conduction of electrons in the metal can be treated like molecules.

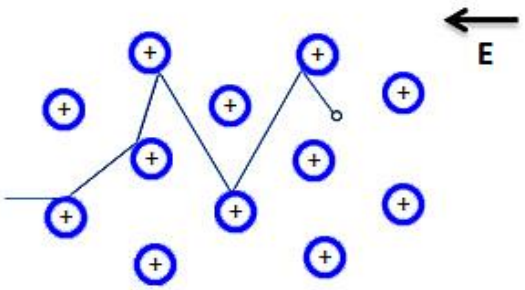

Figure 2.2: Drude's model of electrons constantly collides between heavier and stationary ions.

The formula of the dielectric function of the free electron gas in this model is as follow:

$$\varepsilon(\omega) = 1 - \frac{ne^2}{\varepsilon_o m\omega^2} \tag{2.4}$$

where n is the electron density, ε_o is the vacuum permittivity, e and m are electron charges and mass respectively.

When the concentration of positive and negative charges is equal in medium of the bulk frequency of bulk plasmon is as follow:

$$\omega_p{}^2 = \frac{ne^2}{\varepsilon_o m} \tag{2.5}$$

Resulting rewriting Equation (2.4) with Equation (2.5) below is the:

$$\varepsilon(\omega) = 1 - \frac{\omega_p{}^2}{\omega^2} \tag{2.6}$$

As the Drude model does not include Introducing frequencies above that of plasma, it is necessary to introduce a constant offset, ε_∞, which add to the effect of inter-band transitions. In this case, the dielectric function is becomes:

$$\varepsilon(\omega) = \varepsilon_\infty - \frac{{\omega_p}^2}{\omega^2} \tag{2.7}$$

All the models that have been discussed are used to interpret the plasmonics interaction with various nanostructures.

2.4 Plasmons

The definition of plasmon in metals is oscillation of free conduction electron density against a fixed positive ionic background. The source of this longitudinal oscillation is the long-range correlations of the electrons caused by the Coulomb forces. In order to visualize this phenomenon, picture a rectangular metal slab that is placed towards the left in an external electric field see Figure 2.3. In this position, the electrons will start to more towards the right side. When this takes place, it exposes the positive nuclei (ions) on the left side. The electron movement continues until the field inside the metal is the same value as the internal field. If the given external field is switched off, the electrons will start to repel each other, attracted to the bare left positive ions on the left side. This occurrence will make the electrons oscillate back and forth at the frequency given by equation 2.5.

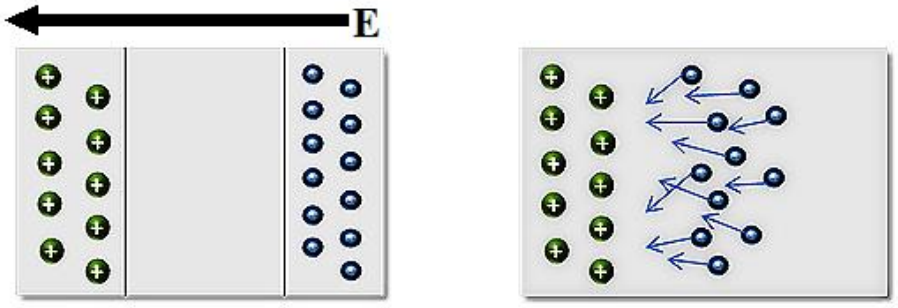

(a) (b)

Figure 2.3: Simple schematic of plasma oscillations. Green spheres represent fixed positive background of ions and blue spheres represent the electron gas. (a) The charges are separated because of the applied external electric field. (b) Situation without external field. The electrons move back to cancel the charge separation.

Many researchers have carried out the electrical and experimental works on these oscillations in gaseous discharges (Langmuir, 1928). There is a strong interaction occurs between the free conduction electrons in the metal and the electromagnetic radiation that are the same size or the wavelength of the incident light. In other words, plasmons are the oscillations of these free conductions that generate dipole into particles when they interact with light in the context of a particle picture. As such plasmons play a major role in the optical properties of metals.

2.4.1 Surface Plasmons

The study on "surface plasmons" (SPs) has been extended to the physical phenomenon. This study is a result of the solution for Maxwell's Equation that has given surface bound mode at the interface between a metal and a dielectric. Surface plasmons are oscillations of electrons that may exist at the interface of two media where the dielectric function of the material is required to change sign across the interface. In this interaction, the free electrons respond collectively by oscillating in the same resonance as the frequency of light wave. A comparison of the level of SPs and bulk

plasmons, it is found that SPs have a lower energy level than bulk plasmons. The strong localized excited SPs are situated across the interface and propagating along the interface and decay exponentially within a normal distance to the interface. SP waves are tightly bound to metal–dielectric, to the extent that they penetrate up to 10 nm into the metal (the so-called skin depth) and typically more than 100 nm into the dielectric (S. Maier, 2007; Murray & Barnes, 2007). Hence, the concentration of EM waves is seen in a region that is considerably smaller than their wavelength. This feature makes the use of SPs desirable for the fabrication of nanoscale photonic circuits operating at optical frequencies (Freise, 2012; Ozbay, 2006). It was RH Ritchie (1957) who first predicted the existence of surface plasmons (Ritchie, 1957). For the next two decades many scientists caught up with the interest to pursue the study of surface plasmons (E. Kretschmann & H. Raether, 1968; A. Otto, 1968).The two main types of SPs in terms of propagation behaviours are the extended or propagating SP and localized SP. The propagating SP belongs to more classical group, since it has been known for a longer time period. However, localized SPR has been advancements in nanotechnology due to advantages in making the fabrication of structures with nanometre scale features more compatible with endless application..

2.4.2 Localized Surface Plasmon Resonance

As mentioned earlier, a strong interaction occurs between the free conduction electrons in metal and EM radiation. This condition occurs when the size of the metallic particles much smaller than excitation laser light wavelength. Plasmons are the oscillations of these free conduction electrons resulting in the generation of dipole in the particles due to the interaction with the light Figure 2.4. A resonant state occurs when the frequency of the light matches the frequency of the oscillating electrons. This types of resonance is defined as localized surface plasmon resonance (LSPR) in the case of nanometre-sized structures (Murray & Barnes, 2007).

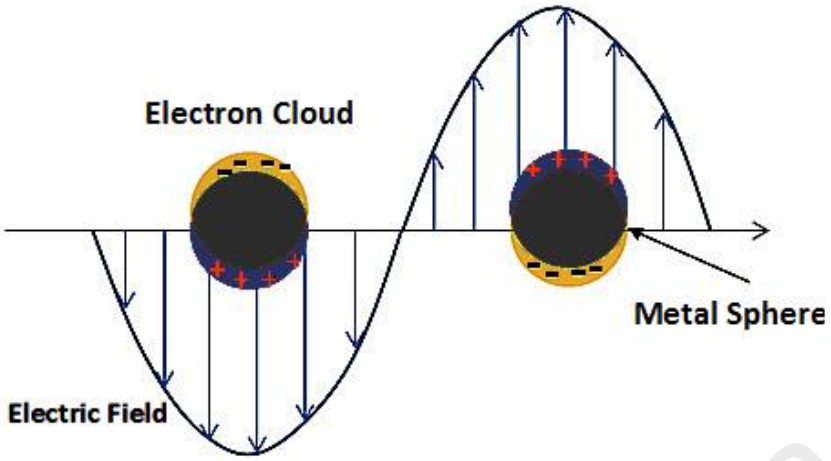

Figure 2.4: Schematic resonance of surface plasmon resonance where by the free conduction electrons in the metal nanoparticle are driven into oscillation due to strong coupling with incident light.

The energy of plasmons in a free electron model is defined as (S. Maier, 2007):

$$E_p = \hbar\sqrt{\frac{ne^2}{m\varepsilon_0}} = \hbar{\omega_p}^2 \tag{2.8}$$

where, n is the density of free electrons, e is the elementary charge, m is the electron mass, ε_o is the permittivity of free space, $\hbar$ is the Planck constant, and ω_p is the frequency of bulk plasmon. For metals with low inter-band absorption, the proposed Drude models is used to sure be the dielectric function, which explains the response of damped, free electrons to an applied electromagnetic field with a frequency of ω (S. Maier, 2007):

$$\varepsilon_r(\omega) = 1 - \frac{\omega_p}{\omega^2 + i\gamma\omega} \tag{2.9}$$

where $\tau = \frac{1}{\gamma}$ the relaxation time and ω is is the angular frequency of an applied electromagnetic field.

There are several factors that influence the LSPR modes such as particle size, shapes, and particles distribution (Murray & Barnes, 2007). In other words, the LSPR can be supported by wide variety of structural features. For instance, the individual particles could have shapes ranging from the simple sphere to ellipsoids, rods, stars and cubes. As result, new types of resonance behaviours can be achieved with interaction on pairs of particles. Sometimes the LSPR modes are considered as holes or voids instead of particles, when their geometry is inverted. Besides that, there are also localized modes that are associated with particle distribution. The specific inter-particle distance of these modes is used for tuning the resonance modes.

There is an increase in the amount of absorption and scattering whenever there is an increase in particle size. Both these factors contribute to the optical extinction of metallic nanoparticles. However, when the particle size increases sufficiently scattering takes over from absorption to be Lorne the dominant force to the extinction (Bohren & Huffman, 1998; Rukshan Fernando, 2012), when this happens the position and width of the LSPR changes. These changes are caused by the way the surface charges induce the polarization field which affects the amplitude and relative phase of the scattered and incident fields.

Another important factor that influences the LPSR modes is the shape of the particles. Researchers have conducted optical studies on a wide variety of different shaped particles. But recently, there was a rapider development of sophisticated methods for the fabrication of nanostructure. As mentioned earlier, the more typical fabrication methods involved either growing the particles from a solution or depositing the material through a patterned mask in lithographic techniques. The main aim of most studies in this field is the atom of optimizing the localization and enhancement of the field associated with LSPR. This can be achieved by designing structures with an

inhomogeneous configuration, such as core-shell particles or with sharp geometrical features such as nano prisms, nanotubes and star-shaped particles (Das & Raj, 2010; Qadir, Ahmad, & Sulaiman, 2014; Sabuktagin, Hamdan, Sulaiman, Zakaria, & Ahmad, 2014; Sherry et al., 2005). The LSPR modes can be also be tuned by the interaction between two or more particles separated at near distances. Usually, the distance allowed is within the decay length of the electromagnetic (EM) field associated with the mode. The coupling between LSPR modes can cause hybridization effect and produce the high and low energy modes with differing EM field distributions (Murray & Barnes, 2007). The primary motivation for the study of pairs of particles is the presence with strong EM field enhancements within the gap between particles (Kinnan & Chumanov, 2010; Quidant, Zelenina, & Nieto-Vesperinas, 2007).

2.5 Plasmonics optical properties

The branch of optics that describes the behavior of light in nonlinear media in which the dielectric polarization P responds nonlinearly to the electric field E of the light, its impact is not only extensive in technology, but also specific in industrial applications. The progress in nonlinear optics has been on the move since the first demonstration of an all-optical nonlinear effect in the early sixties. The main focus was on the physical aspects of the interaction of nonlinear radiation matter till now. In the last decade, the interest in nonlinear optics has been extended including various aspects of nonlinear optics. This widening interest can be attributed to the improvement of the performances in nonlinear optical materials. Consequently, the understanding of the nonlinear polarization mechanisms and their relationship to the structural characteristics of the materials has improved considerably. In addition, new development in techniques for the fabrication and growth of artificial materials has dramatically contributes to this evolution. The goal is to find and develop materials that portray nonlinear features and at the same time satisfy all the technological requirements for applications such as wide

transparency range, fast response, high damage threshold and smooth interface with other materials. Improvements, together with the possible rendering of the implementation of nonlinear effects in devices, have opened up avenues of study for new nonlinear optical effects and the introduction of new concepts. This research study describes new emerging concepts in the field of nonlinear optical materials with a focus on materials that may bring good prospects for transmission and processing in applications related to the field in technology of information (Degiorgio & Flytzanis, 1995; Huttunen & Törmä, 2002; Scalora, Dowling, Bowden, & Bloemer, 1994; Soljačić, Ibanescu, Johnson, Fink, & Joannopoulos, 2002; Tran, 1996). In non-linear optics the interaction of light with atoms gives rise to variety of optical processes besides multiphoton absorption and changing in the refractive index (a non-linear phenomenon arising from the excitation of an atom, whereby two or more photons are absorbed during the processes). During an interaction with atoms, the beam of monochromatic light can be partially converted into light of frequency that is in harmony with the fundamental frequency. Similarly, the beams of light with two or more varying frequencies can be combined to produce a light beam that can alter the refractive index of the medium which it passes through an amount of light which is proportionate to the intensity of the beam. As theory of non-linear optics lies in an extensive field, it embodies a wide variety of phenomenon. In fact, the key that opened the door to non-linear optics is the availability of numerous varieties of high-powered lasers that produce monochromatic beams of extremely high intensities. One significant property of the laser beam lies in its high degree of coherence which is due to the synchronization of the stimulated emissions of different radiating atoms. Coherence, an essential feature of non-linear optics enables one to combine the weak contributions of non- linear interaction from widely separated parts of an excited medium, so as to produce a favorable result.

2.6 Theory of nonlinear optics

The explanation of nonlinear effects lies in the manner a beam of light propagates through a solid. The nuclei and associated electrons of the atoms in the solid form an electric dipole. The electromagnetic radiation that interacts with these dipoles causes them to oscillate. Based on the classical laws of electromagnetism, the dipoles themselves act as sources of electromagnetic radiation. If the amplitude of vibration is small, the intensity of the incident radiation increases the relationship between irradiance and the amplitude of vibration to become nonlinear. Therefore, as the intensity of incident radiation increases, frequency doubling or second harmonic generation (SHG) and effects of higher order frequency are seen to take place. In a nonlinear medium, the induced polarization is a nonlinear function of the applied field. A medium exhibiting SHG is like to a crystal comprises of molecules with asymmetric charge distributions arranged in the crystal. The arrangement is such that a polar orientation is maintained throughout the crystal. In very low fields, the induced polarization is directly proportionate to the electric field (Nalwa and Miyata 1997).

$$P = \varepsilon 0 \, \chi \, E \tag{2.10}$$

where χ is the linear susceptibility of the material, E is the vector of the electric field; ε0 is the permittivity of free space. In high fields, polarization becomes independent of the field, while susceptibility becomes field dependent. Therefore, this nonlinear response can be expressed by stating the induced polarization as a power series in the field.

$$P = \varepsilon 0 \left\{ \chi^{(1)} . E + \chi^{(2)} : E . E + \chi^{(3)} \vdots E . E . E + \ldots \right\} \tag{2.11}$$

However, the progress in the fabrication of new optical materials with better performance is crucial in the development of photonic technology. Bearing this in mind, materials with a nonlinear optical (NLO) response are expected to be significant in

enabling optoelectronic and photonic technologies. In fact, numerous NLO single crystals have been identified as materials for use in optical sensors and electro-optical devices. Thus, nonlinear optical materials have acquired a dignified status as large number of devices utilizes solid-state laser sources. NLO materials have been singled out as an essential item for the fabrication of electro-optic modulators, which convert an electric signal into an optical one during transmission on a fiber optic cable. Currently, such devices are made from inorganic an NLO material which enhances the operation of the optical devices. As the exchange and processing of information is growing at a rapid pace, it is inevitable for powerful data-systems to accommodate larger networks, electrons in nonlinear crystal are bound in a potential well, holding the electrons at the lattice points in the crystal; faster processors and mass storage devices are under intensive research and development (Suresh, Ramanand, Jayaraman, & Mani, 2012).

2.7 Nonlinear optics materials

Nonlinear optical (NLO) materials play a major role in nonlinear optics especially in applications in information technology and industrial sector. This effort has been fruitful in the applied aspects of nonlinear optics for the past decade. This success has considerably improved the understanding of the nonlinear polarization mechanisms and their relation to the structural characteristics of the materials. However, the net polarization of a material depends on its symmetrical properties, with respect to the orientation of the impinging fields. From Equation 2.11, it can be deduced that the odd order terms are orientation independently, but the even order terms are absent in a centro-symmetric environment. Thus, materials for second order NLO must be orientation friendly and without centrosymmetric in order to be functional. However, these restrictions are not applicable to third order materials. Meanwhile, plasmonics materials that are light dependent with NLO effects are used to make pivotal optical devices. It is expected that these devices yield favorable results in fiber communication

and optical sensor as they maximize the characteristics of light such as parallel and spatial processing capabilities and high speed in their operations. Hence, the aim is to develop materials with many nonlinearity features and at the same time meet all the technological requirements such as wide transparency range, fast response and high damage threshold for all the applications. There are two NLO effect of concern in plasmonics materials, namely nonlinear absorption (NLA) and nonlinear refraction (NLR) and optical induced phase transition. The first two effects are dominant in the current study, and will be explained as follows:

2.7.1 Nonlinear Absorption (NLA)

This phenomenon occurs due to the absorption coefficient is proportionate to the optical intensity. The challenge in plasmonics materials is due to two photon absorption that is driven by thermal process, where by the incident light that is absorbed by the metal film is converted to heat in a free electron cloud. The heat is then transferred over a timescale of a few picosecond or femtosecond to the crystal lattice of the metal. It can be inferred that optical properties of the metal are a function of the electron temperature and the lattice temperature. Absorption happens through a nonlinear process, is due to the excitation of two photon absorptions (TPA) that make the electron jump from the ground level to a high energy level where the energy gap is twice the energy of the incident photon. Two photons are absorbed simultaneously for the occurrence of such transition. The likelihood of this transition is proportionate to the square of the number of incident photons that becomes more significant at high intensities. The two photon absorption can be expressed as $(\alpha + \beta I)$, where α is linear absorption coefficient while β is the nonlinear absorption coefficient (Djellali et al., 2009; Owens, Fuentes-Hernandez, Hales, Perry, & Kippelen, 2010; E. W. Van Stryland & Sheik-Bahae, 1998).

2.7.2 Nonlinear Refraction (NLR)

A phenomenon whereby there are changes in the refractive index of a material due to an applied electrical field (intensity of light) which is known as the Kerr effect. The high intensity laser beam passes through a material, the electric field of the beam can induce a change in the refractive index of the material that is proportional to the square of the applied electric field. The total refractive index of the material is the sum of the refractive index, n_0, with no laser beam present and the term $n_2 I$, where n_2 is the second-order nonlinear refractive index and I is the intensity of the beam as $n = n_0 + n_2 I$. The change in refractive index could be positive or negative. Values of n_2 are generally small so the high beam intensities are required to have a significant effect. However, if the refractive index change is positive, the Kerr effect combined with diffraction can lead to self-focusing of the laser beam since the centre of the beam will have higher. The index changes are equivalent to having a positive gradient index lens.

The negative sign of n_2 indicates the suitability of the sample to be used as an optical limiter for laser radiation due to self-defocusing. According to the results obtained, the sign of n_2 obtained for all as-nanoparticles was negative which means it will diverge the radiation due to the changes in refractive index of the material (self-focusing and self-defocusing) observed in the material, leading to reduction of transmittance at far field (due to distortion of spatial profile of Gaussian beam) (Dancus et al., 2010; E. W. Van Stryland & Sheik-Bahae, 1998). The optical limiting happens when the output power rises initially with an increase in input power for all the samples, but after a certain threshold value the samples start defocusing the beam, resulting in a greater part of the beam cross-section which being cut off by the aperture. The suitability of the sample to be used as an optical limiting depends on the sign and the value of nonlinear refractive index, n_2. Besides, the presence of strong nonlinear absorption produces good optical limiting (R. S. S. Kumar, Rao, Giribabu, & Rao, 2008).

2.8 Optical Sensors

One of the sections in this chapter presents a discussion on the modifications of the optical fiber to form various optimizations of side polished optical fiber sensors. The discussion has included the evanescent mode and mode sensing mechanisms based on the relative transmittance power of the modified cladding and core.

2.8.1 Optical fiber

The waveguide principles of an optical fiber resemble a cylindrical dielectric waveguide that transports energy at wavelengths in the visible and infrared portions of the electromagnetic spectrum. This waveguide uses the Total Internal Reflection (TIR) phenomenon that occurring at the interface between two media with different refractive indices. The propagation of light in an optical fiber occurs through TIR, which is controlled by the refractive indices of the core and cladding. The central core which guides the light is embedded in an outer cladding with a slightly lower RI. The formation of guided rays in the fiber requires the ray to be incidental on the core. Figure 2.5 shows the formation of the guided rays, where θ_a is the acceptance angle and θ_c is the critical angle between the fiber core and cladding.

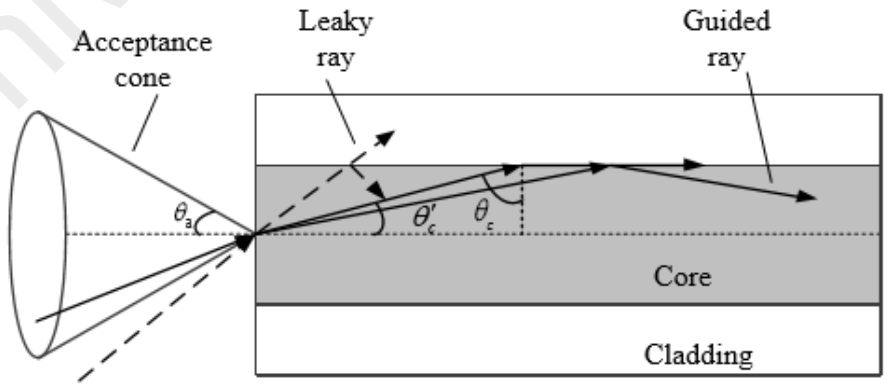

Figure 2.5: Schematic of the propagation of light in an optical fiber launched into the core (Nguyen, 2012).

The light ray incident that is outside of the acceptance cone loses part of its power to the cladding at each reflection. As this is not guided, the modes are known as “leaky” or "refracting". Figure 2.6 (a) shows this refracting ray, whereby it loses a fraction of its power and in doing so; the ray weakens when it propagates during cladding.

The path of a light guided or bound light ray is entirely confined within the core by TIR. Figure 2.6 (b) illustrates the path of a guided or bound ray. Since, a bound ray is contained completely within the core it can propagate indefinitely without any loss of power in the absence of absorption and scattering losses in the core. These rays are categorized by a value of θ_z, based on the condition given below (Nguyen, 2012) :

Bound or guided rays: $0 \leq \theta_z \leq \theta_c$,

Refracting or leaky rays: $\theta_c \leq \theta_z \leq \pi/2$

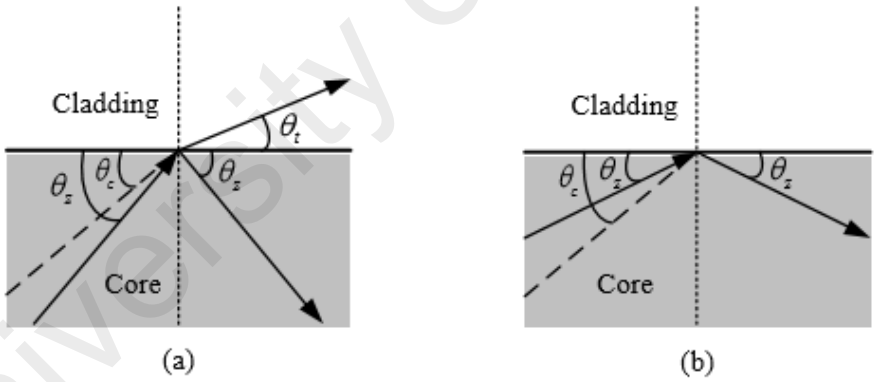

Figure 2.6: Schematic of the (a) refracting or leaky rays and (b) bound or guided rays in an optical fiber waveguide (Nguyen, 2012).

According to Maxwell's Equations, when light undergoes total internal reflection, the electromagnetic field should remain continuous at the boundary of two optical media. Consequently, the formation of a stationary wave takes place, extending into the cladding that is the norm of the interface (Toriumi, Yanagimachi, & Masuhara, 1992).

This is known as the evanescent wave, with the strength of the electric field decaying exponentially away from the boundary. Figure 2.7 illustrates this phenomenon.

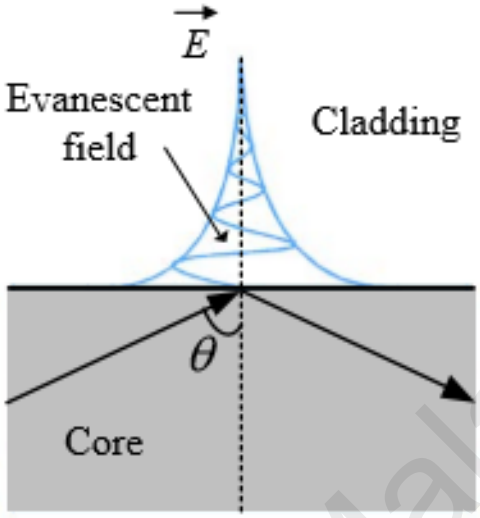

Figure 2.7: Illustration of the evanescent wave formed when light undergoes total internal reflection, showing the variation of the electric field with distance from the interface.

According to Maxwell's Equations, when light undergoes total internal reflection, the electromagnetic field cannot be discontinuous at the boundary of two optical media. Consequently, a stationary wave is formed that extends into the cladding normal to the interface (Z. Zhang & Ewing, 2002). This is known as the evanescent wave, and the electric field strength decays exponentially away from the boundary as illustrated in Figure 2.7. The depth of the penetration of the evanescent field is as follows:

$$dp = \frac{\lambda 0}{2\pi\sqrt{n_{core}^2 \, sin2\theta^2 - n_{cladding}^2)}} \tag{2.12}$$

λ_0: wavelength of light in free space

θ : angle of incident

$n_{Core,}$: refractive index of core

$n_{Cladding}$: refractive index of cladding

The depth of the penetration of the evanescent field is measured by a change in the optical characteristics of the outer medium (i.e. change in the refractive index). Any modification in the optical properties of the guided wave (phase velocity) is induced through the evanescent field. Integrated optical sensors utilize the evanescent field's detection principle extensively in this operation. The evanescent field is a part of the guided light that travels through a region that extends outward at ~100 nanometer in the medium surrounding waveguide, when there is a change in the optical characteristics of the outer medium (i.e. a change in the refractive index) the optical properties of the guided wave (phase velocity) are modified in the region of the evanescent field. In other words, the evanescent field detection principle is used widely for the operations of integrated optical sensors.

2.8.2 Optical fiber as sensors

Many government agencies, commercial bodies and agricultural organization are very concerned about temperature, stress, humidity, and the presence or concentration of a chemical or biological species. It has been reported that optical fiber sensors are able to monitor these environmental factors. The use of optical fiber sensor is highly in demand in sensing technologies.

The reasons for this choice are as follow:

1. Precision and sensitivity: Because of the dielectric nature of glass, the immunity of the Optical Fiber Sensor (OFS) has high immunity to electromagnetic and radio frequency interference is high. As such the use of optical fiber sensor ensures accuracy and precision. Most of these electrical sensors with OFS are sensitive even to the small perturbations in the environment.

2. Remote sensing: It is possible to use a segment of the fiber with a long segment of another fiber (or the same fiber) as a as a sensor gauge convey the sensing information to a remote station. Optical fiber transmission cables offer significantly lower signal loss, in comparison to signal transmission in other sensors. Also, it can maintain a high signal-to-noise ratio (SNR).

3. Distributed measurement: An optical fiber communication network allows the user to carry out measurements at different points along with the transmission line without any significant loss when the signal passes through it. In this way, a parameter can be monitored, control, and analyzed over an extended length or area.

4. Operation in hazardous environments: It has been proven that optical fiber sensor is able to operate under extreme conditions, such as high temperature, high pressure, corrosive and toxic environments, places with high radiation, large electromagnetic fields and other harsh environments.

5. Compactness and flexibility: As optical fibers very compact in size, it becomes an advantage the setting up of a compact measurement and acquisition system. Also, the optical fibers have proven to be very adaptable as they have demonstrated the ability to perform well in many types of measurements.

6. Easy transportation: Optical fibers are very lighter weight so it is easy to transport them to remote locations. These advantages, optical fiber sensors have been employed to replace conventional sensors in some chemical sensing applications. They are also used in laboratories as tools to provide accurate and stable measurements in the experimental research. The use of optical fibers to sense the chemical concentration of analyses has been reported in literature since the 1960s. Optical fiber sensors have found applications in chemical (Chan, Ito, & Inaba, 1984; Stewart, Jin, & Culshaw, 1997; Wolfbeis, 2004), biochemical (Barker, Kopelman, Meyer, & Cusanovich, 1998; El-Sherif, Bansal, & Yuan, 2007; Ferguson, Boles, Adams, & Walt, 1996; Healey, Li, & Walt, 1997), biomedical and environmental (Dietrich, Jensen, & da Costa, 1996; Holst & Mizaikoff, 2001; Mizaikoff, Taga, & Kellner, 1995; Schweizer, Latka, Lehmann, & Willsch, 1997) sensing.

2.8.3 Single mode fiber

Single Mode Step Index Fiber has a uniform refractive index higher than a cladding. The refractive index which changes abruptly at the core cladding boundary is known as step index fiber. The fiber is covered by an opaque protective sheath. The core diameter of a typical SMF-28 is measure as 8 um and cladding 125 um.

CHAPTER 3: EXPERIMENTAL METHOD

3.1 Introduction

This chapter presents a detailed discussion on the implementation of experimental works that begin with development of the nanoparticle layers, followed by the characterization of their physical, linear and nonlinear optical properties and finally their incorporation with optical waveguides to produce optical sensor. The following discussion is presented in three sections: The first segment discusses the different experimental methods used for the fabrication of nanoparticle layers. This section includes description of substrate materials used, preparation of substrates for nanoparticle layer fabrication and methods used to investigate the physical properties of the nanoparticle layer. The second section involves the investigation of the linear and nonlinear optical characteristics of the nanoparticle layers. In the third section, development of the optical sensor by integration of nanoparticle layer with optical waveguides is also been carried out. The integration methods are discussed, following by the description of performance characterization procedures.

3.2 Substrates

Two types of planar substrate materials have been used for all the experiments in this study, namely borosilicate microscope glass slides and indium-tin oxide (ITO) coated silica glass slides. The borosilicate glass substrate was used at the start of the experiment for characterization and optimization purposes while the ITO coated glass substrate was used for the end product of different metallic structures like Micro-flower and Nano-dendrites. The ITO coated substrates were providing from Ossila, while the borosilicate glass substrate was obtained from local laboratory equipment supplier. The substrates are cleaned thoroughly before start of any experiment or deposition processes. It is crucial that the surface stay clean as any impurities may affect the quality of the nanoparticle layer deposition. There are many different methods of

cleaning these two glass substrates. Through they are similar except for the use of cleaning solvent. The steps for cleaning the substrates are listed as follows:

Steps of cleaning glass substrate

1. Mix DI water with detergent in a beaker with a ratio of 2:0.5.
2. Immerse glass substrate in the mixture and sonicate for 15 minutes.
3. Rinse the substrate thoroughly with DI water to remove all the traces of soap.
4. Rinse the substrate with acetone spray, followed by ethanol spray.
5. Rinse the substrate again with DI water.
6. Dry the substrate using nitrogen gas blower to complete the cleaning process.

3.2.1 Steps for cleaning ITO coated glass substrate

1. Mix DI water with detergent in a beaker with a ratio of 2:0.5
2. Immerse glass substrate in the mixture and sonicate for 15 minutes.
3. Rinse the substrate through with DI water to remove all traces of soap.
4. Rinse the substrate with acetone spray, followed by iso-propanol spray.
5. Rinse the substrate again with DI water.
6. Dry the substrate using nitrogen gas blower to complete the cleaning process.

3.3 Deposition process of metal nanoparticles

Various techniques are used to obtain different types of nanoparticle layer to study the effect of these structures on their plasmon resonance behaviour. The factors that affect the choice for the specific technique are included in the discussion below.

3.3.1 Electron Beam Deposition

The fabrication of metal nanoparticles using physical vapour deposition methods involves first depositing a metal thin film on the planar substrate, followed by thermal de-wetting of the metal thin film controlled and elevated temperature which transforms

into the thin film nanoparticle layer. Techniques of metal thin film deposition including electron beam evaporation, thermal evaporation and sputter coating. The method chosen were is electron beam evaporation deposition as it gives the most homogeneous morphology on the surface. This equipment is manufactured by Korea Coating Materials and Components (KCMC, model EB43-T). This process of coating uses electron beams generated from a tungsten filament as a heat source to achieve evaporation of the metal beads placed in a crucible. The substrate is placed on a holder on top of the crucible to avoid contaminant particle on the substrate surface. Metal which may be employed include gold, silver, platinum and many more. This e-beam evaporation machine comprises of two main parts. The first part is the vacuum system and the second part is the deposition system us show in Figure 3.1.

The vacuum system evacuates the deposition chamber to achieve a vacuum environment important as before the start of the deposition process, this is electrons are very light and can be easily deflected upon collision with other molecules in air to have a good control of the e-beam path and focusing, specific vacuum condition is necessary to reduce to frequency of collisions between the e-beam and the air molecules. The mean free path, which is the average distance an atom or molecule travels before it collides with another particle, required is between 10 – 100 mm which can be achieved at a vacuum level of 3.0×10^{-3} Torr or lower. This vacuum system consists of the rotary pump and turbo molecular pump. The rotary pump can be considered as the main vacuum pump for the entire system and it plays two important functions. First, it initiates the pumping process of the chamber from atmospheric pressure to a medium vacuum condition. Secondly, it acts as a backing pump to the turbo molecular pump. Even though the rotary pump is able to evacuate the majority of gas molecules from the initial atmospheric pressure of the deposition chamber, the pressure achieved is only about $\sim 1 \times 10^{-3}$ Torr which is this vacuum insufficient for the deposition process. So, a

second vacuum pump, namely turbo molecular pump, is needed to further reduce the pressure of the deposition chamber.

The turbo molecular pump (TMP) is a high-speed vacuum pump that can reduce the pressure inside a deposition chamber to a lower pressure (~ 1 x 10^{-6} Torr) compared to the rotary pump. The rotation speed of the TMP can go up to a maximum of 633 revolutions per second. However, the TMP cannot be used to initiate the vacuum process at atmospheric pressure as the large amount of gas particles may damage the delicate fan blades of the TMP. This is also the reason to use the rotary pump to initiate the chamber vacuum condition before the operation of the TMP.

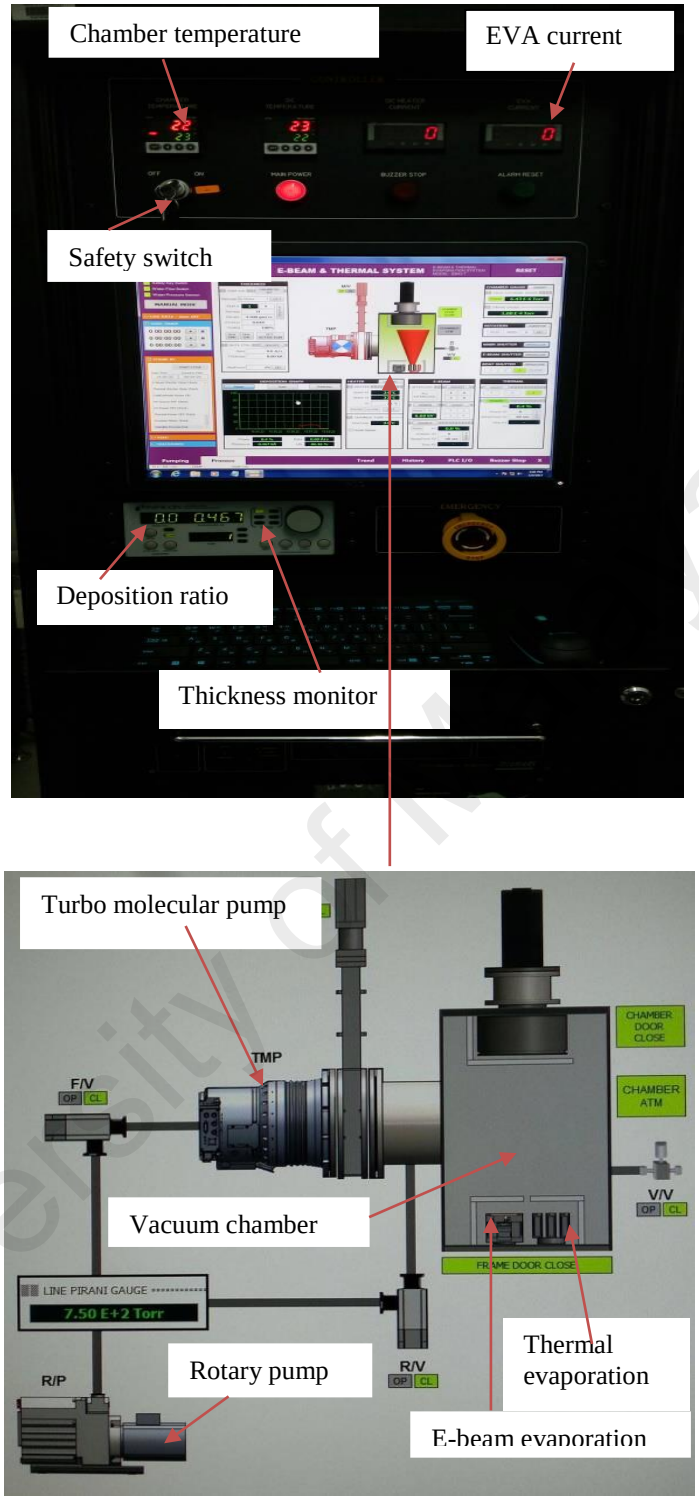

Figure 3.1: Diagram of the whole electron beam evaporation system model EB43-T.

3.3.2 Deposition System

The deposition system is located inside a chamber in the electron-beam machine whereby the deposition process takes place. Figure 3.2 shows the layout of the components inside the chamber. With the help of a built-in substrate holder, the substrates are placed on top, facing downwards, and are protected by a main shutter. The target metal beads are placed inside a copper crucible which is located at about 40 cm below the substrate holder. The deposition systems used can operate in two deposition modes, namely electron beam and thermal deposition. While the electron beam allows for the deposition of homogenous and very thin layer metals of less than 10 nm, the thermal deposition enable the deposition of metal layers with thickness of 200 nm and above. For electron beam deposition, the deposition chamber is first pumped by the vacuum system to a high vacuum condition. When the pressure inside the chamber reaches a reading of ~ 1 x 10^{-3} to ~ 1 x 10^{-6}, the deposition process can be carried out. Then the power supply is turned on to allow current to flow through the tungsten filament inside the deposition chamber (see Figure 3.2).

The current and voltage are increased gradually to sufficiently high level for the tungsten filament to release the electrons. When the electrons are released, a deflecting magnet will bend the pathway of the electrons so that the elements will beam directly onto the metal targets. The heating by electron beam causes the atoms from the target metal to change into a gaseous state. These gaseous atoms will then precipitate upon contact with any solid surfaces, coating everything in the vacuum chamber.

For thermal evaporation deposition, the same vacuum condition need to be first achieved. Boat shutter is equipped with thermal heater, so from the start, the power is increased until it reaches the melting point of the metals. For example, to melt gold the system need to be set as 13KW with chamber temperature of 76^{o}C while for silver, a

power of 10KW with chamber temperature of 55^{o}C required to avoid any contamination of the metal beads, the crucible is protected by an electron beam shutter. A thickness monitor is located at the same level with the substrate holder and it is connected to a programmable control unit (PCU). At the control unit box, a display screen shows the deposition rate (thickness (Å) / time (seconds)) as well as the thickness during the deposition process. Calibration of the PCU is necessary when changing the deposition material to allow accurate and reliable deposition rate and thickness monitoring. The deposition rate can be controlled by setting the amount of current flow. When the deposition system reaches the desired deposition rate, the main shutter protecting the substrate will open and the time taken for the deposition process is recorded simultaneously. When the desired thickness is achieved, the shutter is closed and the recording of the time is stopped.

Figure 3.2: Picture of the inside chamber in the electron beam for the deposition process.

3.4 Electrophoretic Deposition Technique

Electrophoretic deposition (EPD) is a term used in a wide range of industrial processes, which includes electro-coating, cathodic electrodeposition, anodic electrodeposition, and electrophoretic coating, or electrophoretic painting. One significant characteristic of this process is that the movement of the colloidal particles suspended in a liquid medium is under the control of an electric field (electrophoresis) and the materials is deposited onto a substrate electrode. All the materials involved in electrophoretic deposition are made up of colloidal particles that can be used to form stable suspensions and carry a charge. These materials include polymers, pigments, dyes, ceramics, and metals. Figure 3.3 illustrates the set-up of this technique. The set-up consists of an electrical power supply that is connected to a pair of electrodes where one of the electrodes is the substrate for the collection of the deposited materials. Those electrodes must be immersed into the colloidal dispersion of desired materials. In this work, two types of colloids are used for the deposition of silver nanoparticles. One is silver colloid dispersion in aqueous buffer solution that has been obtained directly from the supplier, Sigma Aldrich. The other one is silver nitrate that has undergone several processes to form colloid. Both types of solutions gave different unique types of plasmonics features that will be discussed in detail in Chapter 5.

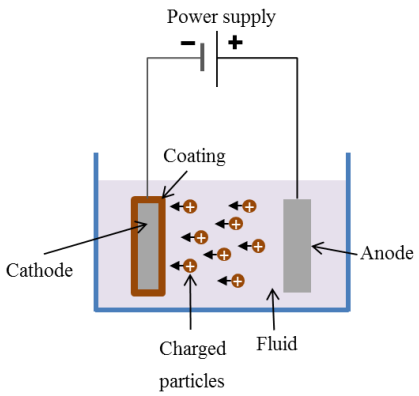

Figure 3.3: Schematic diagram of electrophoretic deposition process.

3.5 Spin Coating Technique

Spin coating is a technique used to deposit uniform thin films onto a flat substrate used a spin coater. The spin coater for spin coating process is shown in Figure 3.4. The procedure begins with dispensing a small and controlled amount of coating material (in a form of liquid) on the centre of the substrate. The substrate may be in a stationary state or it may already be spinning at a low speed. Then, the rate of spinning is increased to a high speed of rotation in order to use the centrifugal force to spread the coating materials evenly on the surface of the substrate. When rotation take place, the spinning spills the fluid off to the edges of the substrate and this continues until the desired thickness of the film is achieved. The solvent used for this step is usually volatile so it evaporates easily. Thus, the higher the angular speed of spinning, the thinner is the film produced. Other than that, the thickness of the film is also depends on some other parameters such as the viscosity and concentration of the solution.

Figure 3.4: Spin coater machine used in this study.

3.6 Production of nanoparticles

De-wetting is a physical phenomenon describing the rupture of a thin liquid film on a substrate to form droplets. Thermal de-wetting is the simple way of using thermal annealing to create nanoparticles from thin layer films. For example, silver nanoparticles layer can be produced from a silver thin film when annealed at 250^{o}C and gold nanoparticles from gold thin film at 600^{o}C, with an annealing duration of 2-3 hours. Thermal de-wetting of metallic thin films is achieved due to the reduction of the surface energy of the thin film and of the interface energy between the film and substrate during at elevated temperature, depending on the metals used (Wang, Ji, & Schaaf, 2011). Thermal de-wetting of various metal thin films have been demonstrated on silica substrate (e.g. Au, Co, Ni, Fe, Cu Ag) (Bischof, Scherer, Herminghaus, & Leiderer, 1996; Herminghaus et al., 1998; Krishna et al., 2010; Michalak, Miller, Yolcu, & Gellman, 2012; Strobel, Kirkendall, Chang, & Berggren, 2010; Wang et al., 2011), as well as on silicon substrate.

There are three dewetting mechanisms:

- Heterogeneous nucleation, which is initiated from defects located at the film surface or the film–substrate interface.
- Homogeneous nucleation, which occurs via a small thermal density fluctuation that acts as a nucleus for holes formation.
- Spinodal dewetting, which occurs by the amplification of periodic film thickness fluctuations such films induce self-correlated dewetting patterns (Wang et al., 2011).

The nanoparticles produced in this work are formed via the homogeneous nucleation mechanism using thermal annealing in a convection oven. The oven used is shown in

Figure 3.5. The temperature can be controlled from room temperature to 300^{o}C via a digital control interface.

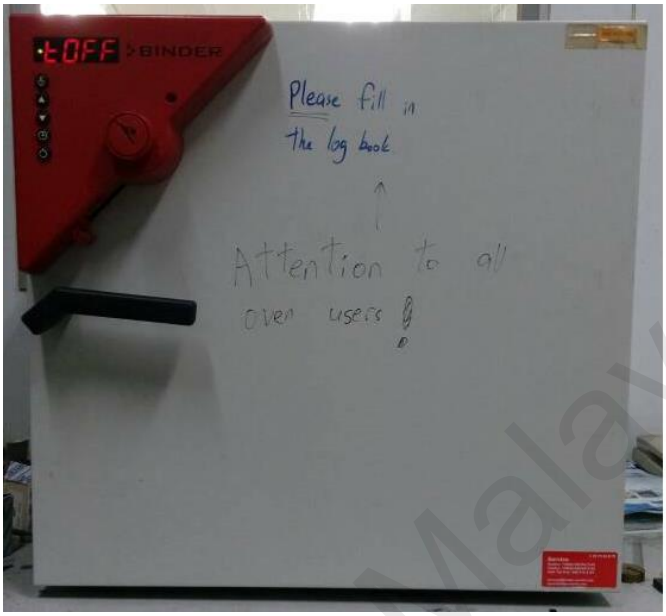

Figure 3.5: Thermal annealing process in the convection oven used in study.

3.7 Characterization of nanoparticle layers

This section explains the general procedures of techniques that have been used in the characterisation of the nanoparticle layers produced. The surface structure of the deposited nanoparticle layers is examined using field emission scanning electron microscopy (FESEM). The information obtained is then been used to calculate the particle size, density and distribution of each nanoparticle layers. Optical absorption of the nanoparticle layers is examined using UV/VIS/NIR spectroscopy to study their plasmon resonance behaviour, while the *Z*-scan technique is used to study the nonlinear optical properties of the layers. These techniques are discussed in detail in the following sections.

3.7.1 Field Emission Scanning Electron Microscopy (FESEM)

FESEM imaging is used in the study of microstructure morphology. FESEM imaging can resolve structures of micro-meter and nano-meter scale. Figure 3.6 shows the FESEM system (model JEOL JBM-7600F) that has been used in this works. In the FESEM, primary electrons are liberated from a field emission source and accelerated in a high electrical field gradient. The FESEM chamber is operated under a vacuum condition for the same reason as the e-beam deposition system. The primary electrons are focused by an objective *lens* to produce a narrow scan beam towards the sample surface. Impingement of the primary electrons on the specimen produces two types of electrons:

- Backscattered electron: BSEs are reflected primary electrons after impingement on the specimen. BSEs from heavy elements (high atomic number) have higher energy than BSEs from light elements (low atomic number) and thus appear brighter in the image camper to secondary electron.
- Secondary electrons: (SEs) are low energy electrons emitted from the specimen due to the energetic passage of beam electrons. Secondary electrons that are ejected from the k-shell of the specimen atoms by inelastic scattering interactions with beam electrons. The first collected by attracting them towards an electrically biased grid at about +400 V, and then further accelerated towards a phosphor or scintillator positively biased to about +2,000. The brightness of the signal depends on the number of secondary electrons reaching the detector.
- Finally, detectors of each type of electrons are placed in the microscopes that collect signals to produce an image of the specimen.

The quality of FESEM images depends on the type of samples. For example, the samples with non-conductive surfaces usually produce poor quality image and

experience difficulty in focusing compared to samples with conductive surfaces due to charging effects, where is reduce as the number of the electrons emitted from the specimen may “charges” lead to decrease incident electrons landing to the specimen image quality. Also to avoid this, the sample is coated fully allowed the accumulated to be charge passed to the ground via the conducting layer. As charging may also carry the samples may experience burning. They for samples with non-conductive surfaces, a thin layer of metal like gold must be coated first before FESEM imaging. The thickness of the film is measured from the cross-section of the SEM image of the sample. The size of particles in the film can be measured directly from the FESEM images using the scale of the scanning magnification.

Figure 3.6: FESEM machine used in this work.

3.7.1.1 Analysis the FESEM images

The FESEM images were analyzed using ImageJ software to determine the population of the nanoparticles, with the following sequence:

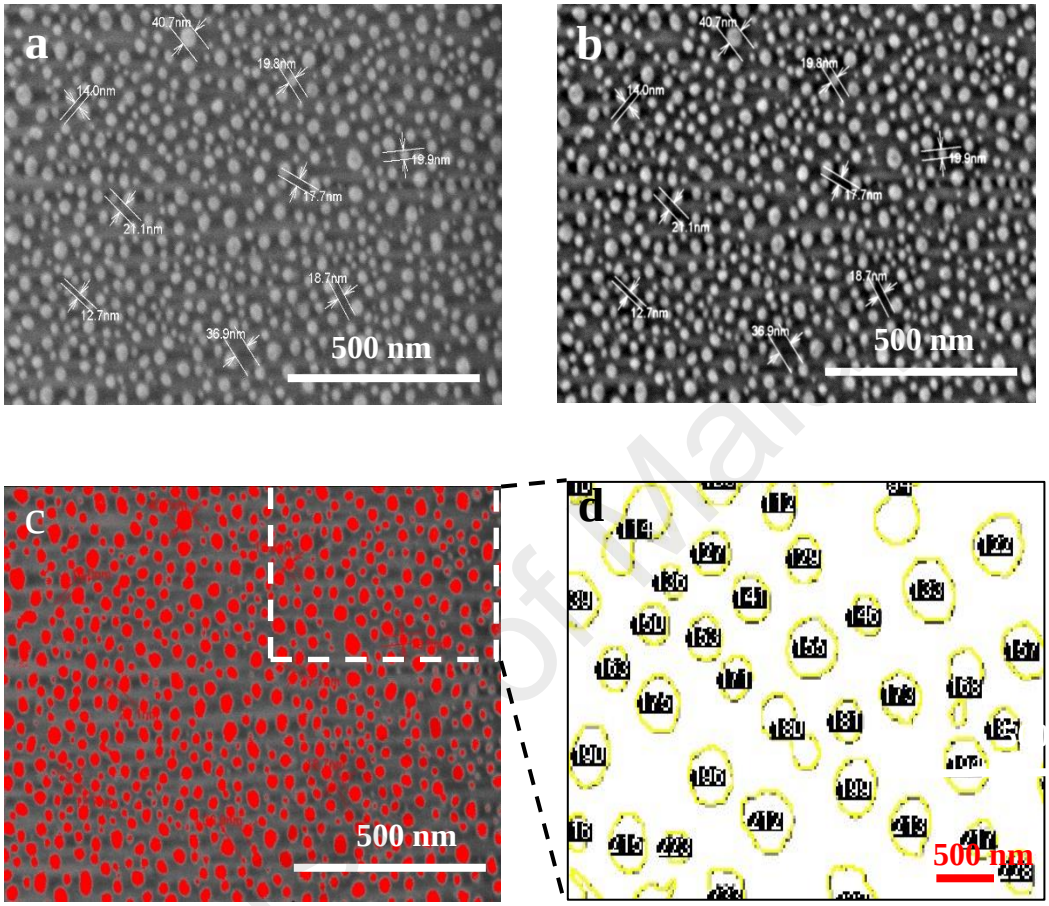

Figure 3.7: Steps taken to analyse the distribution of nanoparticles using ImageJ: (a) Insertion and calibration of FESEM image in ImageJ, (b) Apply band pass filter to increase image contrast (c) Adjust the threshold level for particle sizes and distribution counting (d) analysis of the boundary size of the nanoparticles (Zoom-in view of the top right corner of the FESEM image).

It should be noted that the filtered image is compared with the original image to ensure that the filter and threshold level set reflects the accurate particle distribution to minimize error in particle number and size calculation by the program.

3.7.2 UV/VIS/NIR Spectrophotometer

Spectroscopy is the study of the interaction between electromagnetic radiation (in the range of ultraviolet, visible, and near infrared range) and a matter. A spectrophotometer is used to measure the intensity of light passing through a sample (I) and compares it with the intensity of light before passing through the sample (I_o). The ratio I/I_o are known as *transmittance* and it is usually expressed as percentage (%T). The absorbance, A, is based on the transmittance where $A = -log\frac{T\%}{100\%}$. R% which is the reflectance percentage obtained from the ratio of intensity of light reflected from a sample to the intensity of light reflected for a reflectance material. The PERKIN ELMER LAMBDA 750 UV-Vis spectrometer is used for recording the reflectance spectra in the range of 200-2000 nm and investigation of visible wavelength absorption profile of the photoactive films at room temperature .Meanwhile, the software UV Winlab 6 software was used to control parameters and operation of equipment. The image and technical specifications of PERKIN ELMER LAMBDA 750 UV-vis spectrometer are shown in Figure 3.8 and Table 3.1 below.

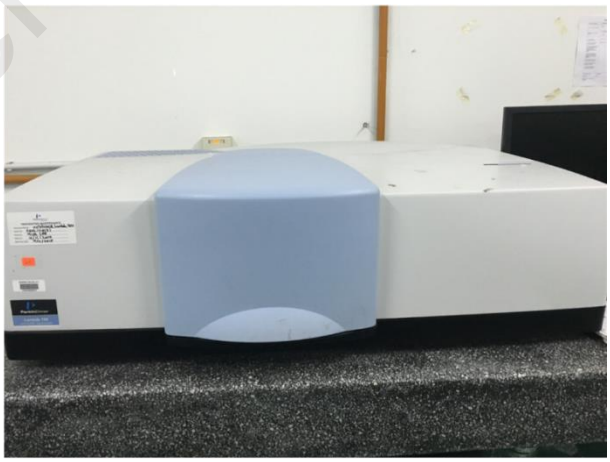

Figure 3.8: The UV/VIS/NIR spectrophotometer model PERKIN ELMER LAMBDA 750.

Table 3.1: Specifications of UV-Vis-NIR spectroscopy.

Wavelength range	190 nm – 3,300 nm
Wavelength accuracy	± 0.15 nm UV-Vis ± 0.5 nm NIR
Wavelength reproducibility	UV-Vis $\leqslant$ 0.06 nm
Light source	Tungsten-Halogen (Vis) and Deuterium (UV)
Light detector	Photomultiplier R955

3.8 *Z*-Scan experimental set-up

The Z-Scan technique used in this work is the easy way and simple method to measure the nonlinear optical properties of the metallic nanoparticles. The *Z*-Scan set-up is show in Figure 3.9 where the samples are scanned in front and behind the focal plane of a focusing lens. The laser employed is femtosecond laser type (Spectra-Physics-Tsunami) with minimum pulse-width 100 fs, repetition rate 82 MHz and wavelength 750 nm to 800 nm. The laser has a plane polarized Gaussian beam profile with initial laser diameter 2.2 mm to 4.5 mm.

The laser propagates in the *Z*-direction (indicated in Figure 3.9) through a bi-convex lens with different focal length like (25 mm, 37.2 mm and 52 mm). The beam waist $w°$ (μm) at the focal point is about 8.8 µm. The average power of output is attenuated to a range between 10 mW and 90 mW using a free space attenuator (model 5215-M new focus), Pulse energy is calculated to be 0.15 – 0.85 nJ, yielding a laser maximum laser intensity from $I_{0 =}$ 107.627-526.807 MWcm^{-2}. As the repetition rate of the laser used is 82 MHz, which can be considered quasi-continuous-wave, heating of samples during the Z-scan measurement may occur and induce thermal nonlinear optical effect (Ara et

al., 2012). This may contribute a non-constant nonlinear absorption and nonlinear refraction index values depending on the maximum incident intensity used in the Z-scan setup, which is determined by the laser incident power and the focusing lens used. Therefore, comparison of NLA and NLR values for the same nanolayers must be made with these considerations methods.

The power meter used for power measurement is Thorlab PM100USB. During the scanning along the Z-direction, the nonlinear effect occurred in the region before and after the beam waist of laser, as the intensity of the laser exceeds the nonlinear optical intensity threshold of the nanoparticle layers. The *Z*-Scan can be setup for open-aperture and closed-aperture measurements as results from both measurements are needed to differentiate the nonlinear refraction (NLR) and nonlinear absorption (NLA) of each metallic nanoparticle layer. Details on the two *Z*-scan setups are given in the following sub sections.

3.8.1 Open aperture

The *Z*-scan open aperture setup is used to measure the nonlinear absorption *(NLA)* of the sample. The measurement is carried out with the aperture being opened fully and not blocking the laser beam *(S=1)*. *NLA* arises when two or more photons are absorbed simultaneously in a single absorption process. In the case of two photons absorption *(TPA)*, the incident photon energy is $1.0 < E < 0.5$ times the bandgap energy. When the sample is moved along the *Z*-axis towards the focal point, the intensity is increased. When the threshold intensity of TPA is achieved, the transmitted power measured will reduce due to additional nonlinear absorption. Conversely, when the sample is moved away from the focal point, the intensity incident onto the sample reduces, and hence, the measured transmitted power will increase to the original value when the incident laser intensity falls below the TPA threshold. The calculation of TPA Nonlinear absorption

coefficient, β can be obtained from the open-aperture *Z*-scan measurement using the expression $\alpha(I) = \alpha_0 + \beta_I$, where α_0 is the linear (low intensity) absorption coefficient, while βI accounts for a phenomenological nonlinear processes such as induced absorption $(\beta > 0)$ or induced transparency (saturation of linear absorption, $\beta < 0$).

3.8.2 Close aperture

The *Z*-scan close aperture setup is the same as the open aperture setup but with the aperture adjusted to a smaller opening to allow only a linear transmittance between *10% to 50% (0.1 < S < 0.5)* (Mezher, Chong, & Zakaria, 2016a; Vivacqua, Espinosa, & Martins Figueiredo Neto, 2012). Depending on whether the sample exhibits a positive of negative nonlinear refraction, the transmitted power will show a peak, followed by a dip, when the sample is translated along the *Z*-axis across the focal point, and vice versa. The is a result of Kerr lensing effect where the refractive index of the sample is dependent on the incident light intensity, $n(I) = n_0 + n_2 I$, where n_0 is the linear refractive index, n_2 is the nonlinear refraction and *I* is the intensity of the incident laser light. Both the effects of *NLR* and *TPA* are measured in the closed-aperture Z-scan. The data obtained from closed aperture *Z*-scan are then divided by the data obtained from open aperture to offset the effects of *TPA* found in the closed aperture measurements. Negative nonlinear refractive index expected from materials that exhibiting plasmonics effect while metal coating usually exhibits positive refractive index (Chapple, Staromlynska, Hermann, Mckay, & McDuff, 1997; Han, Ye, Wu, & Shi, 2008; Majdabadi, Gaeeni, Ghamsari, & Majles-Ara, 2015; E. Van Stryland, Sheik-Bahae, Said, & Hagan, 1993; E. W. Van Stryland & Sheik-Bahae, 1998; X. Yang et al., 2011; Zakaria, Mezher, & Chong, 2016a).

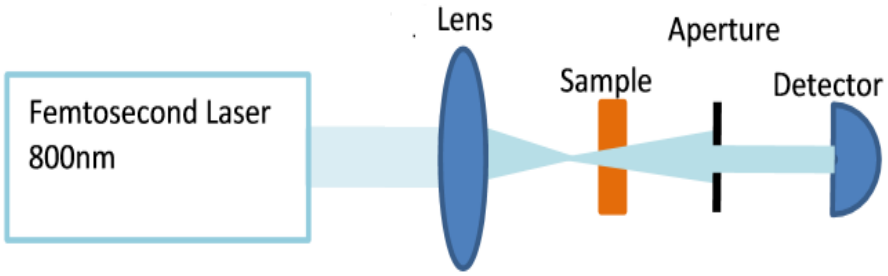

Figure 3.9: Schematic diagram of *Z*-Scan techniques.

3.8.2.1 Analysis the close aperture Z-scan measurement results

To obtain the nonlinear refraction (n_2) for the materials; the divide the data of close aperture on the data of open aperture as show in Figure 3.10 resulting the nonlinear refraction (n_2).

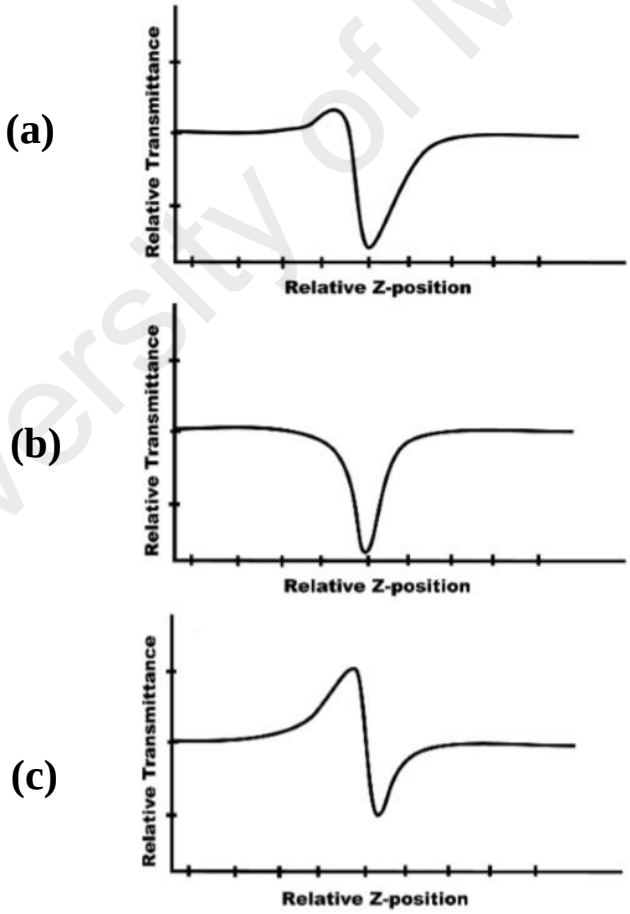

Figure 3.10: Z-Scan (a) Close aperture setup (b) Open aperture setup and (c) nonlinear refraction after subtract the nonlinear absorption (Neethling, 2005).

3.9 Fabrication of Optical Fiber Sensors

This section discusses the structure of optical fibers, principles of light propagation and the modification of the optical fiber structure to develop different types of optical fiber sensors. The discussion includes a description of the sensing mechanisms of the evanescent mode, leaky mode and partially leaky mode. The sensing mechanisms are based on the relative RI of the modified cladding and the core.

3.9.1 Light guiding principle of an optical waveguide

An optical fiber is a cylindrical dielectric waveguide that transports energy at wavelengths in the visible and infrared regions of the electromagnetic spectrum. This waveguide uses the principle of Total Internal Reflection (TIR) that occurs at the interface between two media with different refractive indices. Figure 3.11 illustrates the basic structure of a cylindrical waveguide also known as optical fiber. It consists of a coaxial core, cladding, coating buffer, and an outer jacket. A typical single mode fiber usually has a core diameter of between 8 and 10 μm and a cladding diameter of 125 μm. The condition for TIR is controlled by the refractive indices of the core and cladding. Since light is guided in the core, it is embedded in an outer cladding which has a slightly lower RI. The formation of guided rays in the fiber requires the rays to be incident on the core. It is important to observe this so that upon refraction into the core.

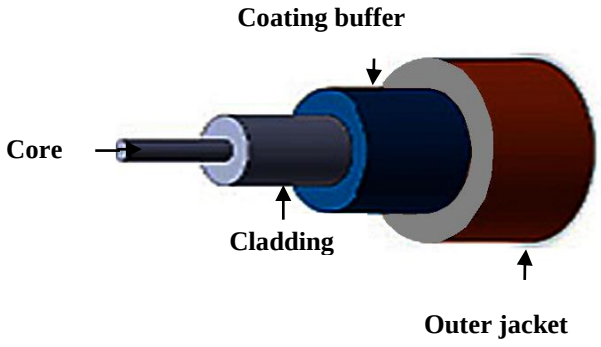

Figure 3.11: Image of optical fiber inner cable.

3.9.2 Fabrication of side polished optical fiber (D- shape fiber)

D-shaped fiber has a non-circular symmetry, where the fiber cross-section resembles a “D” shape. D-shaped fibers can be obtained by polishing the side of a single mode fiber to remove the cladding until the fiber core is exposed. For standard single mode fiber are polished to a depth around ~ 39 μm. The polishing process begins with splicing two terminals of a single mode fiber to the fiber pigtails. While one is connected to a 650 nm red laser source, the other is connected to the optical power meter. A microscope glass slide was used as fiber holder, and the fiber was glued to the glass slide during the polishing process. A sand paper with grit size of 1200 was used to remove the cladding. This manual polishing process begins with rubbing the sand paper back and forth on the fiber until red light propagating in the fiber core appears on the polishing surface. The fiber undergoes fine polishing using a polishing machine (UltraPol TEC 40809) show in Figure 3.12 that used to reduce the roughness of the D-fiber and improve the light transmission.

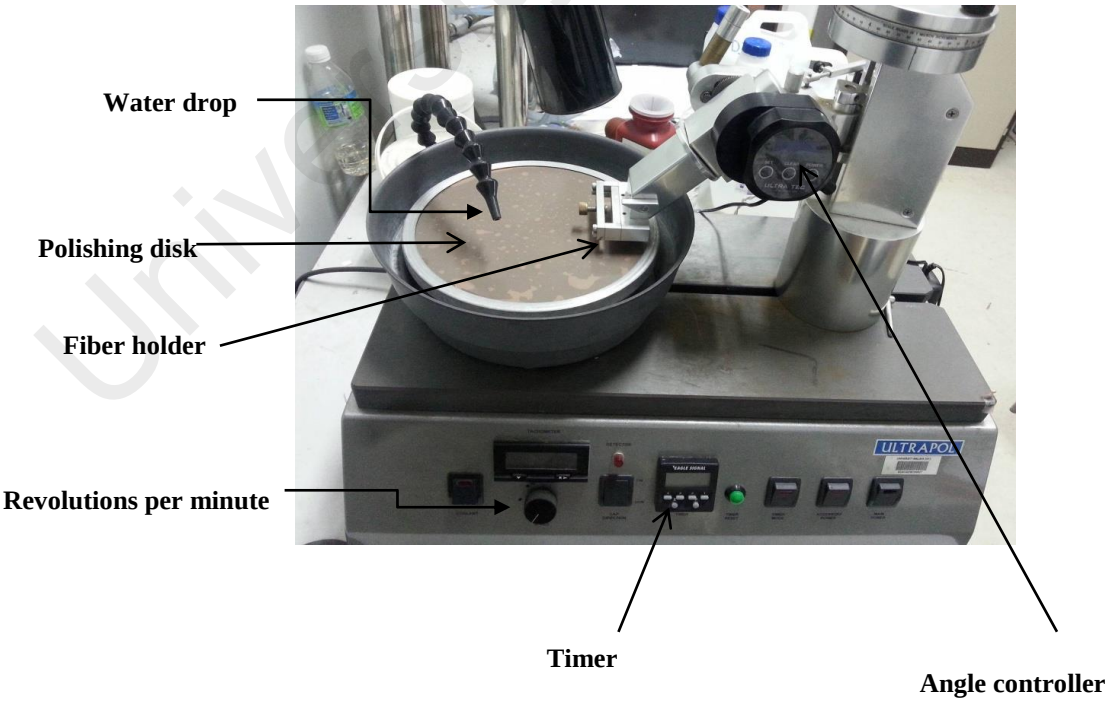

Figure 3.12: Show the ULTRAPOL machine for polishing fiber.

Figure 3.13 (a) and (b) shows an illustration of the D-shape fiber the top view of optical fiber captured using FESEM with 300 magnifications. The polished surface of the D-fiber during the polishing process the transmitted power is monitored in real time. When the polishing surface reaches the evanescent field of the wave guiding mode, the transmitted power will begin to drop as shown in Figure 3.13 (c). Therefore, the change in transmitted power can be used as an indication of the polishing stages. Also, the polarizer controller is used to check the polarization extinction ratio of the D-shape fiber. Two sets of single-mode optical fibers were polished until transmission power loss for both sets become -3.9 dB with polarization extinction ratio of 0.5 dB; and -20 dB with polarization extinction ratio of 3.2 dB, respectively.

There are many other methods of producing D-shape fiber. For example, the V-shaped groove, polishing through the spin coating and wheel polishing (Gao et al., 2012; Luo et al., 2016; Patnaik, Senthilnathan, & Jha, 2015).

The advantages of producing D-shape fiber using the proposed method are:

- No chemical is required for cleaning up when epoxy is used for the adhesion of fiber to microscope glass as the epoxy is heat removable.
- May be applied used for a variety of fibers.
- Better control of polishing location.

The drawback of the manual polishing are:

- It is difficult to control the depth because different people have different hand pressure.
- The fiber can break easily.

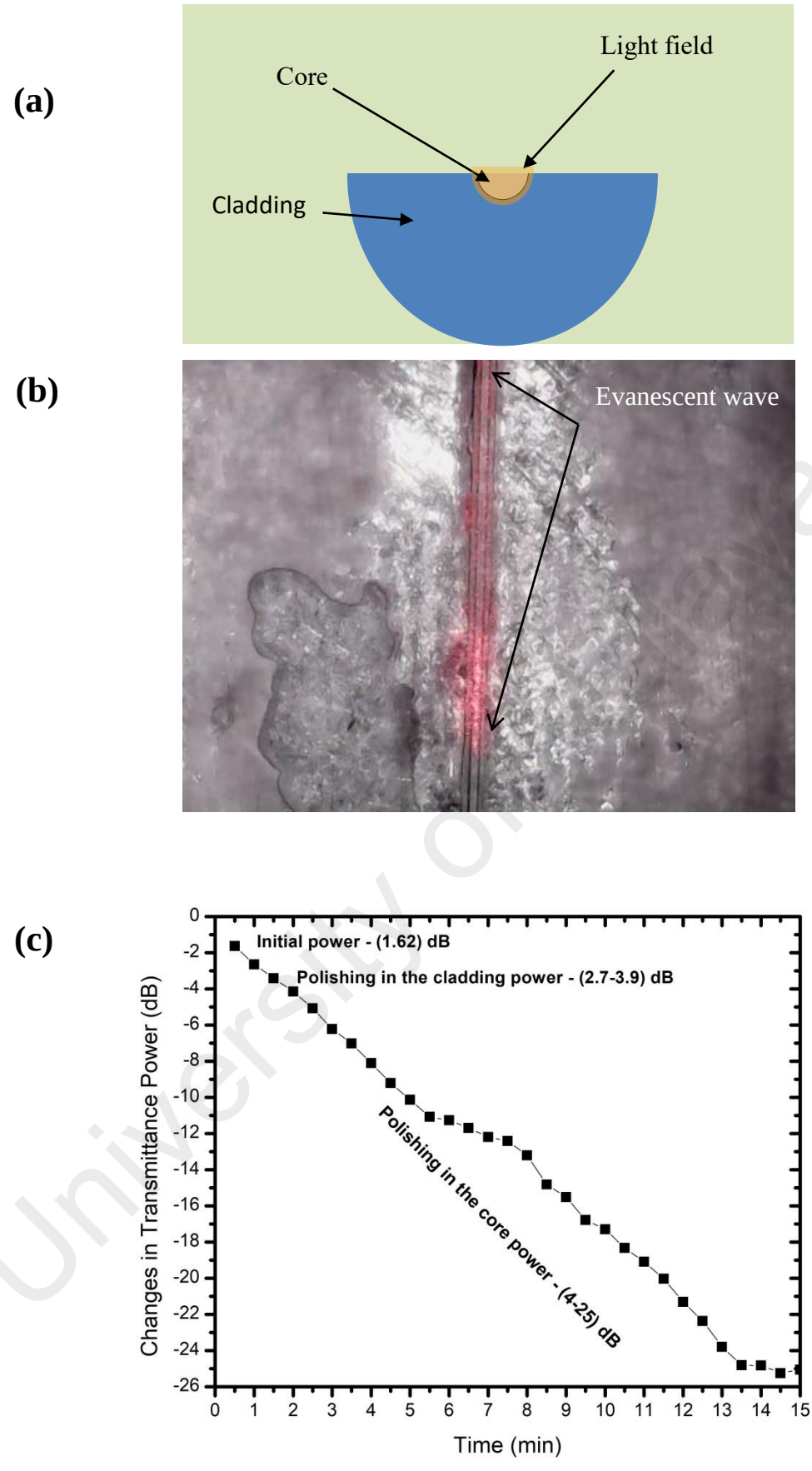

Figure 3.13: (a) Illustration of the side view of a D-shape fiber, (b) FESEM image of the top view of the D-fiber and (c) duration of fiber polishing.

3.9.3 Fabrication of polymer optical waveguide

The fabrication of polymer based waveguide has been done on the substrate coated with silicon dioxide (SiO_2) as under cladding that show in Figure 3.14. The measurement of thickness and refractive index of SiO_2 have been done using Prism coupler (Sairon Technology SPA-4000). The 8 μm is the layer thickness of $SiO_2$with refractive index of 1.444 at 1550 nm. Then, SU8-2010 polymer is spin-coated onto the SiO_2 under-cladding layer. The spin speed is 2500 rpm, with spin duration of 90 seconds. The refractive index of the SU-8 coating is 1.566 at 1550 nm, with a thickness of 5 μm. The spin-coated SU-8 is then subjected to a soft bake process at 80^{o}C for 3 minutes. After the soft bake process, the sample is ready for photolithography process. Contact photolithography technique is used in this work. First; was aligned the photomask with the waveguide channel patterns on the SU-8 sample, followed by ultraviolet light exposure for duration of 8 seconds. It should be noted that photolithography should be carried out immediately after soft bake process to avoid uncertainties due to changes in solvent content in the layer over time. The UV exposed sample then goes through a post exposure bake (PEB) process at a temperature of 80^{o}C for 15 minutes. After PEB, the sample is developed in SU-8 chemical developer to produce ridge waveguides. The cross section of the fabricated SU-8 ridge waveguide is 5 μm in height and 10 μm in width. The waveguide sample was then cut into individual dices of about 1 cm in length. No over-cladding was necessary as the waveguide core needs to be exposed for further functionalization to enable sensing capability.

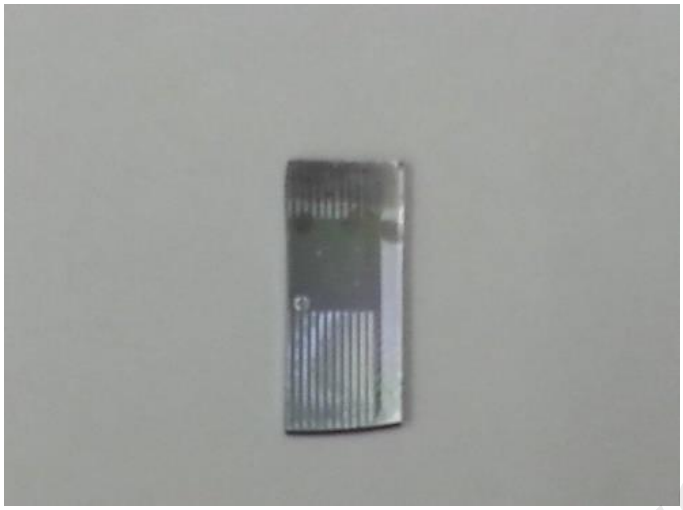

Figure 3.14: Polymer-based waveguide.

3.9.4 Graphene oxide coating

Two drops of 2.4 μL of GO solutions are applied directly onto the microscope glass through drop-casting technique using a micropipette. The sample was then allowed to dry under ambient conditions with the drying process monitored using an optical microscope. To achieve thicker GO coating with the same coating area, multiple-drop-casting of small volume solution droplets onto the same area is applied.

3.9.5 Metal nanoparticles coating

Metal nanoparticles are coated on an optical waveguide to develop waveguide-based surface plasmon resonance sensor. In this case, only D-shape fiber was used as the processes involve elevated temperature treatment beyond the thermal damage point of the polymer waveguide material. The coating process starts with metal thin film deposition. D-shape fiber is first placed onto a fiber holder and the fiber holder is inserted into the deposition chamber. The flat surface of the D-fiber is ensured to be facing up during the placement on the fiber holder so that the evaporated metal from the crucible covers flat fiber surface. The deposition chamber is then pumped down from

atmospheric pressure to a medium pressure at ~ 3×10^{-6} Torr by the rotary pump, before further pumping down to high vacuum at ~ 3×10^{-6} Torr. The pump down process normally takes between 120 minutes to 150 minutes. The chamber is then degassed by applying a heating power lower than the value necessary to initiate e-beam evaporation of the metal in use. This will ensure minimum contamination in the chamber during the deposition process. During degassing, the chamber pressure will increase. After 2 minutes of degassing, the heating power is turned off to allow the chamber pressure to decrease to the base pressure value of ~ 3×10^{-6} Torr. As the chamber achieve its base pressure again, the metal boat shutter is opened and the heating power turned on and increased gradually until the value required achieving the evaporation point of the metal in use. For example, silver requires a heating power of 10 kW to evaporate while gold requires 13 kW. The SPIKES show that the metal is ready to evaporate; this allowing the deposition process to being. The metal thin film coating thickness is monitored using the digital thickness monitor and the ratio of melting point.

The fiber holder together with the D-shape fiber is rotated during the deposition process to ensure uniform coating of the metal thin film. The deposition rate, monitored by the digital thickness monitoring, was kept constant at ~ 0.8 nm s^{-1}. Figure 3.15 shows the D-shape fiber coated with silver thin film on a fiber holder. The thin film coated D-shape fiber, together with the fiber holder is then subjected to thermal annealing process to create nanoparticles via thermal de-wetting. The surface morphology of the thermally de-wetted samples is then measured using FESEM.

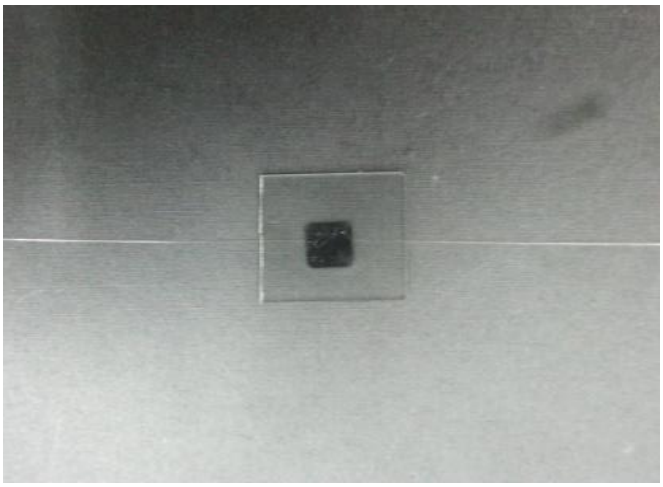

Figure 3.15: Optical fiber coated with metallic layer.

3.9.6 Characterization for GO and metal coated waveguides and side polished optical fiber

To study the optical characteristics of the GO coated planar waveguide, fiber-waveguide-fiber light coupling is necessary. Figure 3.16 shows a standard fiber-waveguide alignment setup for this experiment. The sample is placed on a waveguide holder. The input and output of the waveguide are then connected to optical fibers which are placed on a 3-axis linear alignment stages to allow micro-positioning control relative to the waveguide. The alignment procedure starts with the alignment of the input fiber. In this case, the output fiber is replaced by an objective lens with a numerical aperture of 0.25. The input fiber is connected to a visible laser light (650 nm), while the image of the waveguide output is projected onto a screen using the objective lens. Input fiber-waveguide alignment is confirmed when the waveguide output image showed a bright spot instead of a horizontal line. The objective lens is then replaced by the output fiber and alignment continues with output fiber-waveguide alignment. There will be a sudden increase in measured power when the fiber-waveguide-fiber coupling is achieved. Fine alignment of the input and output fibers are then carried out to obtain

maximum transmitted power. The polarization dependent loss of the waveguide is obtained by measuring the maximum difference in transmitted power when the polarization controller at the input fiber is adjusted. For sensing performance characterization, the transmitted power of the waveguide is measured over time during the application of measure and solutions on the GO-coated waveguide.

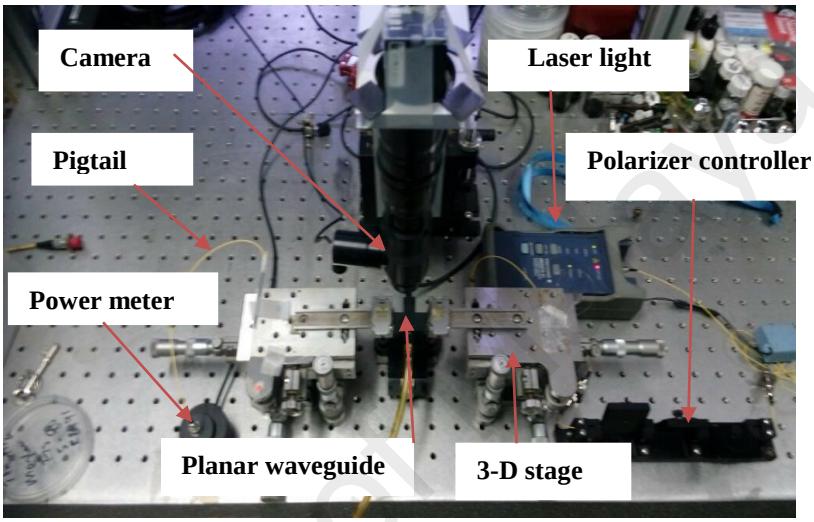

Figure 3.16: Physical view of planar waveguide sensor.

The optical characterization setup of metal coated D-shape fiber is shown in Figure 3.17. As the D-shape fiber is a part of a single mode fiber, no alignment is necessary. The D-fiber are fusion spliced to two fiber pigtails, which are connected to a laser light source (1550 nm) and power meter (Thorlabs PM100 USB) respectively. The polarization extinction ratio of the metal coated D-fiber is obtained by measuring the maximum difference in transmitted power when the polarization controller is adjusted. The sensing performance of the metal coated D-shape fiber is studied by measuring the transmission characteristics of the D-fiber when a measure and solution is applied on the metal coated D-shape optical fiber.

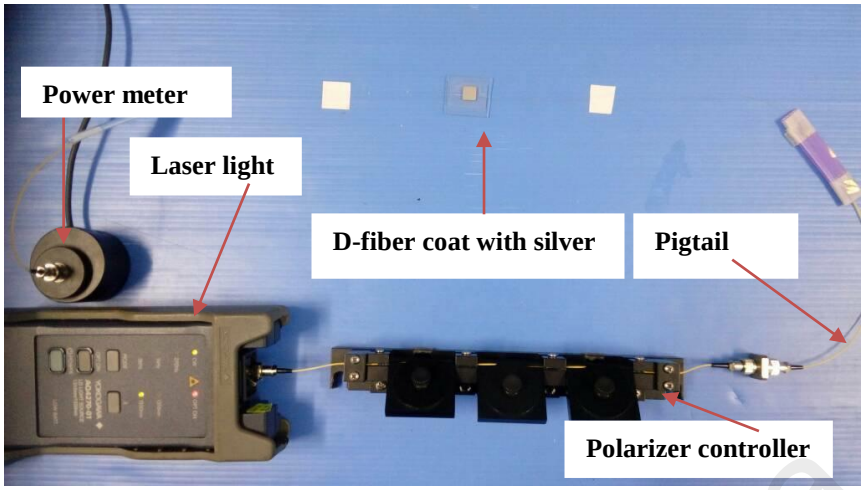

Figure 3.17: Experimental set-up of silver coating on D-shape optical fiber water sensor.

CHAPTER 4: DEPOSITION AND CHARACTERIZATION OF METALLIC NANOSTRUCTURED LAYERS

This chapter presents analysis of metallic nanoparticles layers fabricated using electron beam deposition and subsequent annealing process. The analysis can be divided into three sections, namely Field Emission Scanning Electron Microscopy (FESEM) images analysis, UV-Vis-NIR spectroscopy's analysis and nonlinear optical characterization.

4.1 FESEM analysis of metallic NP layers

FESEM analysis is used to determine the metallic nanoparticles morphology, size distribution and particle density. Nanoparticle layers have been fabricated using different process parameters. This analysis is important because of the particle size and density possibly determines the plasmonics behaviour of the nanoparticle layers.

Table 4.1 summarises the nanoparticle layers deposited and their corresponding process of parameters and labels. Three different groups of nanoparticle layers have been prepared, namely gold nanoparticle layers, silver nanoparticle layers, and hybrid gold/silver nanoparticle layers.

Samples S1 to S5 are gold nanoparticle layers deposited using different e-beam deposition duration to obtain initial gold thin film layer with different thicknesses. The thin film thicknesses fabricated are from 4.2 nm to 13.4 nm. These samples undergo the same annealing temperature of 600^{o}C and annealing duration of 4 hours to create nanoparticles. This fabrication process will allow us to study effects of nanoparticles in relation with the thicknesses layer.

Sample S6 to S9 are referring to silver nanoparticles layer deposited using various deposition durations to examine effects of nanoparticles formed with corresponding

thickness. The initial thin film thicknesses fabricated are from 8 nm to 40 nm. The annealing temperature is set at 270^{o}C and annealing duration of 2 hours enough to create nanoparticles. The annealing temperature for silver nanoparticle is much lower compared to gold samples due to the lower melting temperature of silver relative to gold (Dao, Nguyen, Nguyen, & Nguyen, 2015; Hajakbari & Ensandoust, 2016; Lee et al., 2014).

Samples S11 to S15 are hybrid nanoparticle layers prepared using both gold and silver. The preparation involves a two-step deposition-annealing process, where gold thin film is first deposited and annealed followed by the deposition of silver thin film and subsequent thermal annealing. The gold nanoparticle layers are prepared using the deposition parameters of sample S10. The deposition parameters are adjusted to produce a final gold nanoparticle layer with good surface coverage and suitable particle size. The annealing temperature remains the same with Sample S1 to S5, but the duration is halved to maintain the same total annealing time of 4 hours (2 hours for gold annealing temperature; and 2 hours for silver annealing temperature). On the other hand, silver deposition duration is varied to produce silver thin film with different thicknesses, similar to the thickness range of Sample S6 to S9..

Table 4.1: Process parameters for metal nanoparticle layer deposition.

Sample designation	Deposition material	Thin film thickness (nm)
Gold nanoparticles have different thicknesses and annealing at temperature of 600ºC for 4 hours		
S1	Gold (Au)	4.2
S2	Gold (Au)	4.9
S3	Gold (Au)	7.7
S4	Gold (Au)	9.7
S5	Gold (Au)	13.4
Silver nanoparticles have different thicknesses and annealing at temperature of 270 ºC (2 hours for Ag)		
S6	Silver (Ag)	8
S7	Silver (Ag)	18.5
S8	Silver (Ag)	30
S9	Silver (Ag)	40
Gold/silver nanoparticles annealing at temperature of 600ºC(2 hours for Au) and 270 ºC (2 hours for Ag) with variation of silver thicknesses		
S10	Gold (Au)	11.8
S11	Gold and Silver (Au and Ag)**	11.8 and 8
S12	Gold and Silver (Au and Ag)**	11.8 and 14.9
S13	Gold and Silver (Au and Ag)**	11.8 and 25.9
S14	Gold and Silver (Au and Ag)**	11.8 and 31.6
S15	Gold and Silver (Au and Ag)**	11.8 and 43.6

FESEM images for Sample S1 to S5 are shown in Figure 4.1(a (i) – a(v)). It can be seen that the nanoparticle size increases with the thickness increase of the initial thin films. Using ImageJ analysis software, the nanoparticle size distribution for each Sample are measured and is shown in Figure 4.1(b (i) – b(v)). The average particle size increases from 11 nm to 44 nm for Sample S1 (thickness ~ 4.2 nm) and Sample S5 (thickness ~13.4 nm) respectively. The results agree with the report by Gaspar et.al (Gaspar et al., 2013). The particle density for Sample S1 to S5 is also measured by counting the number of particles within a defined area in the FESEM images using ImageJ software. It is found that the particle density decreases from 1155 μm^2 to 127 μm^2 from Sample S1 to S5, respectively. Therefore, the thicknesses of the samples are

proportional to nanoparticle size and inversely proportional to the particle density. The relationship of average particle size and their corresponding particle density is shown in Figure 4.2, which shows that as particle size increases, the particle density decreases linearly.

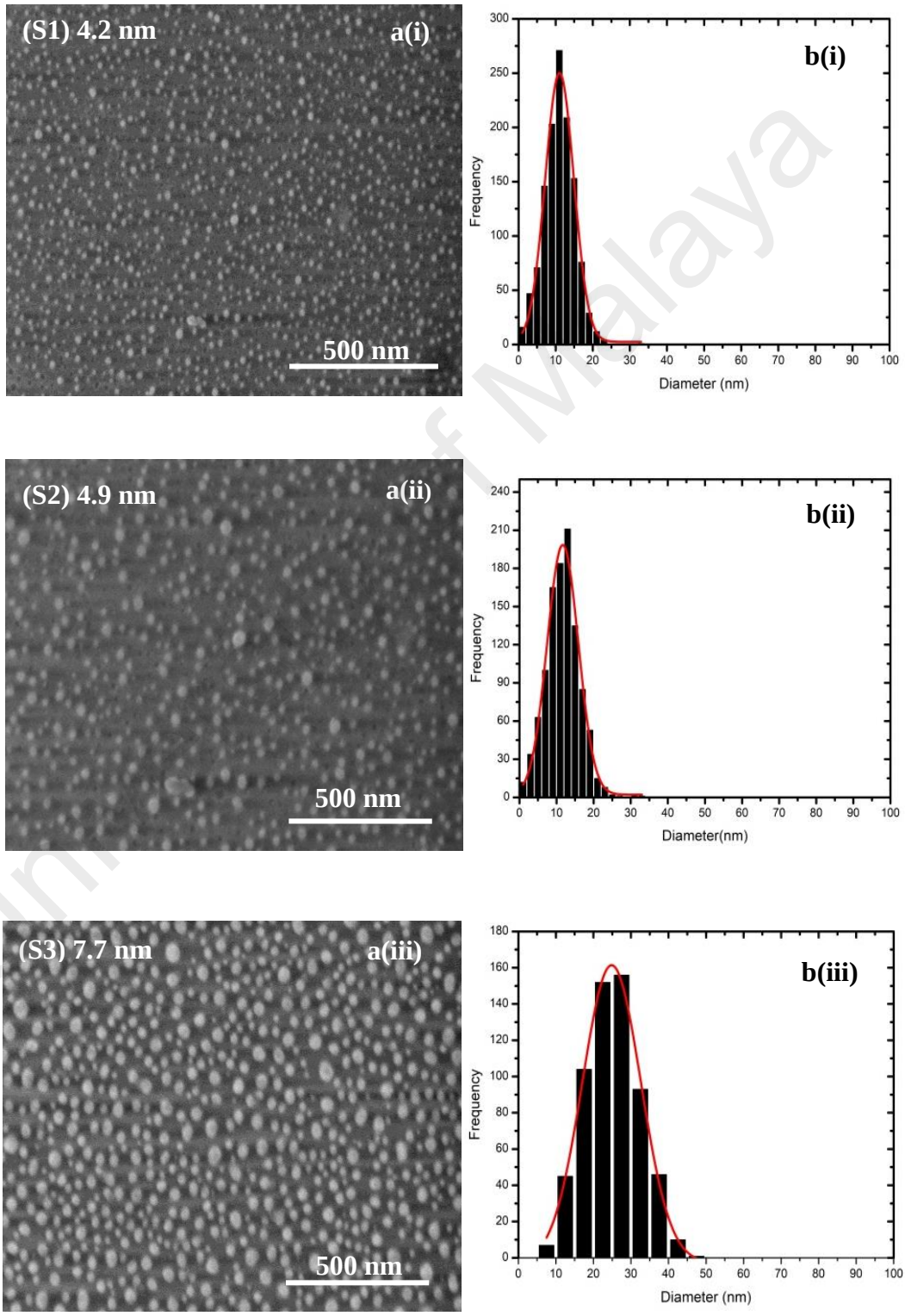

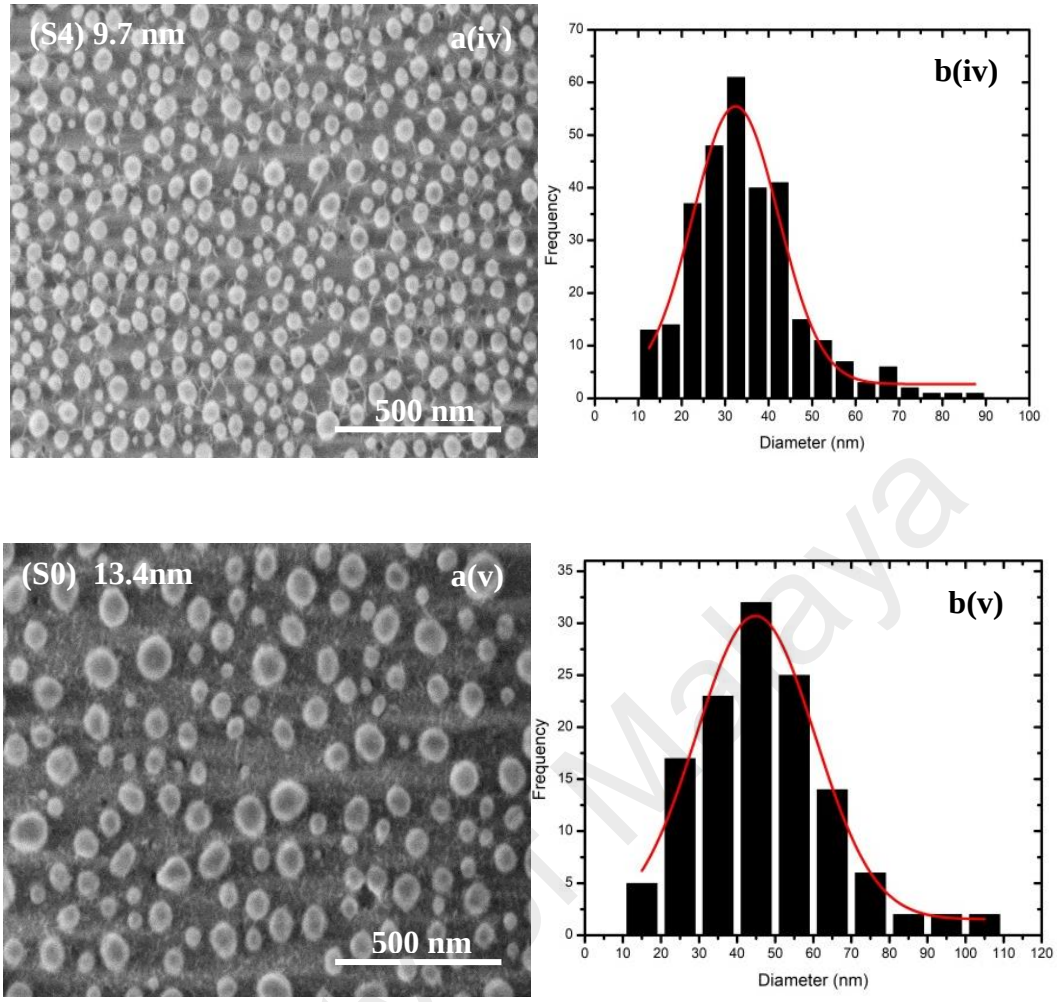

Figure 4.1: FESEM images of S1 to S5 (a (i) to a (v)) nanoparticles. Samples have the average of nanoparticles from 11 nm to 44 nm with scale bars are set at 500 nm. S1to S5 (b (i) to b (v)) are attributed to size distributions of metal nanoparticles at different thickness.

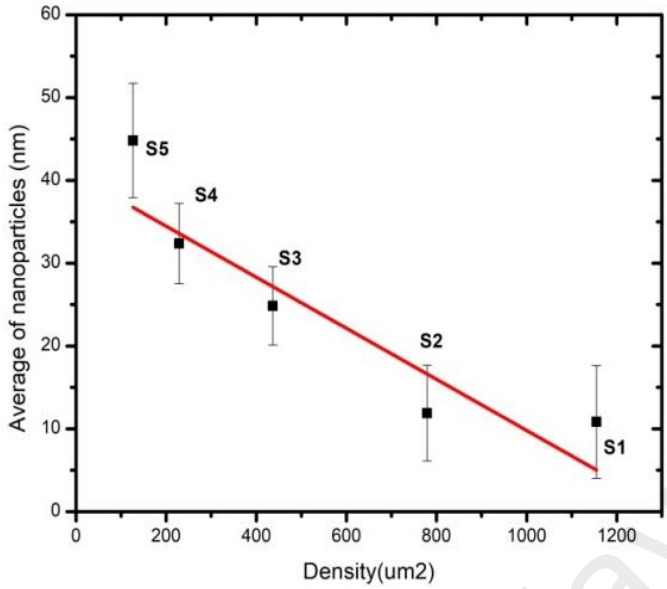

Figure 4.2: The relationships between density and average size of nanoparticle for S1 to S5.

FESEM image of Sample S6 is shown in Figure 4.3(a (i)) and its particle size distribution shown in Figure 4.3(b (i)). Sample S6 with average nanoparticle size is ~ 9 nm, while the particle density is 11.47 μm^2. Sample S9 is shown in Figure 4.3(a (iv)) and its particle size distribution shown in Figure 4.3(b (iv)). The average nanoparticle size is ~ 37 nm, while the particle density is 2.45 μm^2. It is found that the particle density decreases from 11.47 μm^2 to 2.45 μm^2 for Sample S6 and S9 respectively, Therefore, the thicknesses of this sample are proportional to nanoparticle size and inversely proportional to the particles density. The relationship of average particle size and their corresponding particle density is shown in Figure 4.4, which shows that as particle size increases, the particle density decreases linearly. From the results, we can conclude that silver nanoparticle layer can be formed when the initial thin film thickness is less than 30 nm which this agrees reported by Gaspar et al (Gaspar et al., 2013).

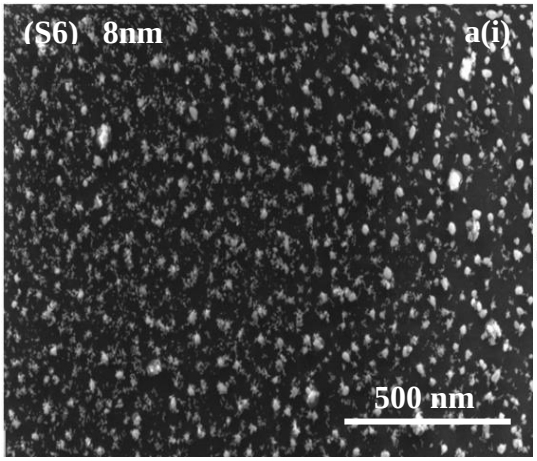

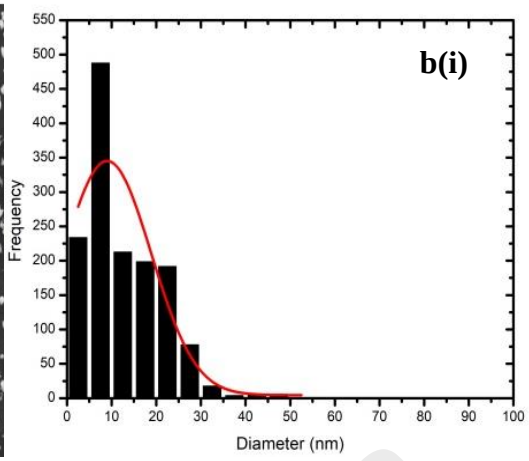

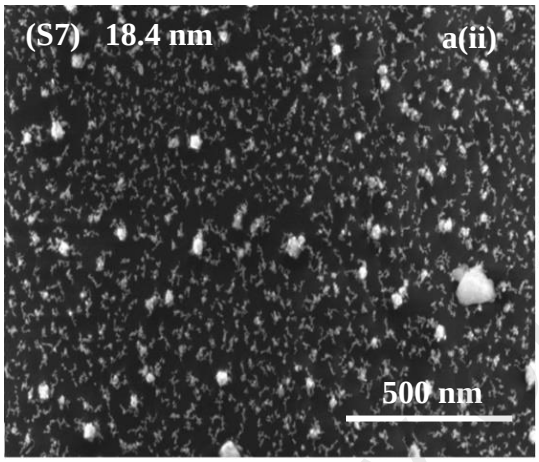

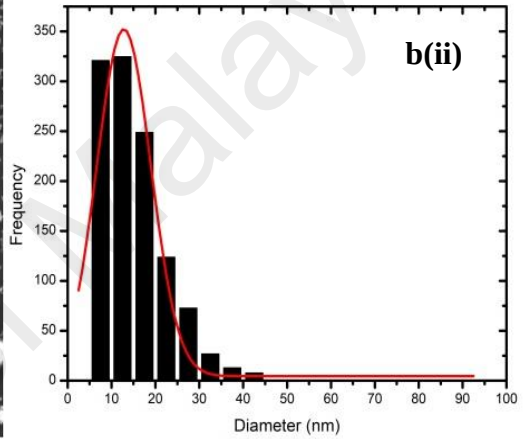

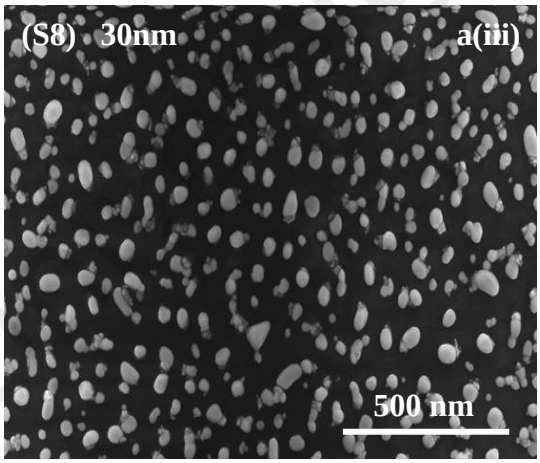

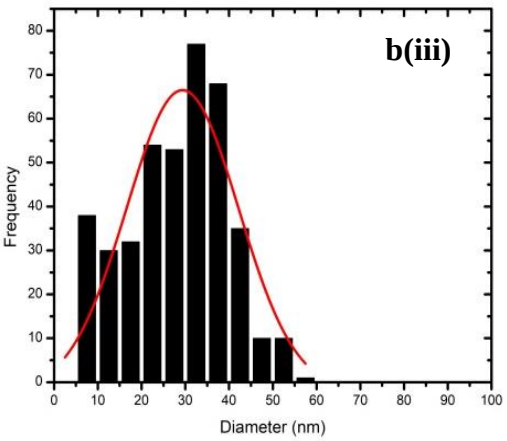

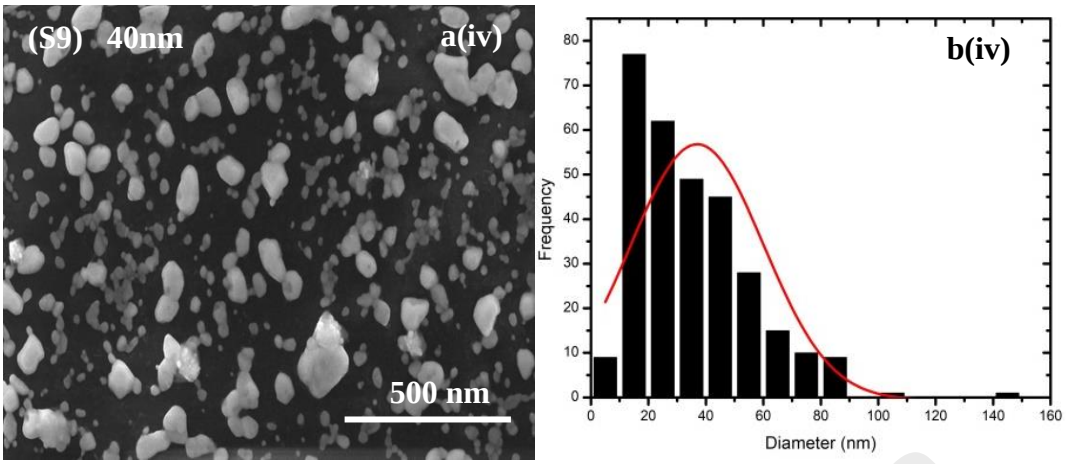

Figure 4.3: Images of S6 to S9 (a (i) to a (iv)) nanoparticles samples have the average of nanoparticles from 9 nm, to 37nm with scale bars are set at 5μm. S6 to S9 (b (i) to b(iv)) are attributed to size distributions of metal nanoparticles for different thicknesses.

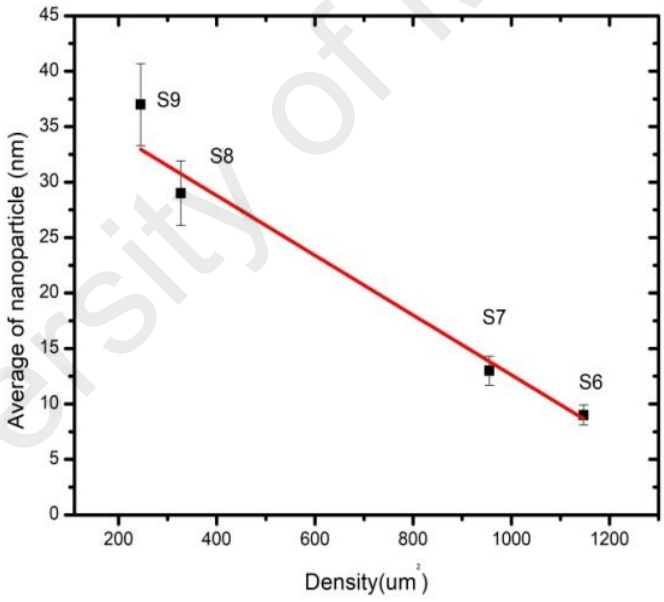

Figure 4.4: The relationships between average size of nanoparticle and density of S6 to S9.

FESEM image for Sample S10, which is the gold nanoparticle layer used for the preparation of hybrid gold/silver nanoparticle layer, is shown in Figure 4.5 (a (i)). The initial film thickness is ~11.8 nm. The particle size distribution is shown in Figure 4.5 (b(i)) and the average nanoparticle size is measured to be ~23 nm. The particle density

is measured to be ~384 μm^2. These values are similar to Sample S3 where the initial film thickness for Sample S3 and S10 are 7.7 nm and 11.8 nm, respectively. This observation indicates that the formation of nanoparticle layers characteristics can be controlled either by the film thickness or by the annealing duration. The limitation of each process parameters in control–eventual nanoparticle layer characteristics can be found in the works of (Agnihotri, Mukherji, & Mukherji, 2014; Hsu & Wu, 2010b; Islam & Mukherjee, 2011; Jiang, Chen, Chen, Xiong, & Yu, 2011; Lee et al., 2014; Piñero, Camero, & Blanco, 2017; Pris, 2014)

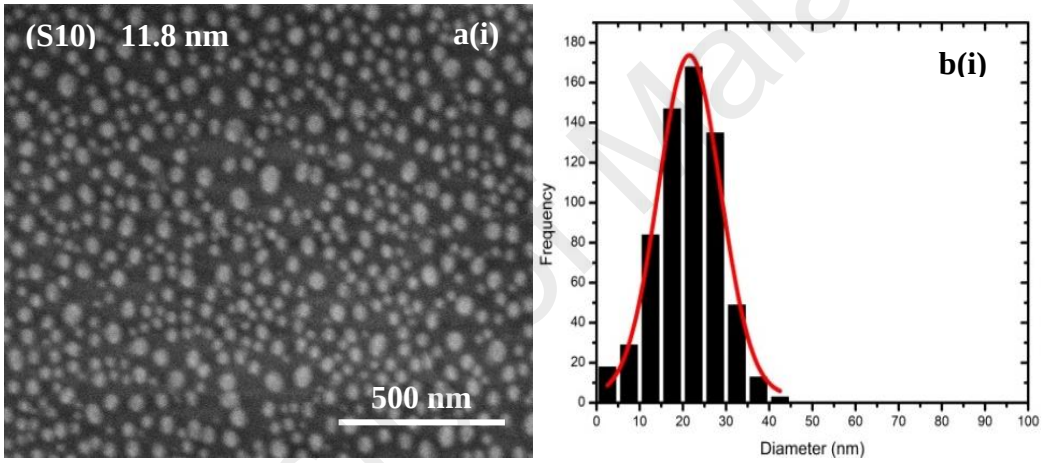

Figure 4.5: FESEM images of S10 a (i) nanoparticles. Samples have the average nanoparticles size of 23 nm.

For the hybrid gold/silver nanoparticles of Sample S11 to S15, the initial gold thin film thickness remains the same at ~11.8 nm, while the silver thin film thickness is varied from 8nm, 14.9 nm, 25.9 nm, 31.6 nm and 43.6 nm by controlling the silver deposition duration. The FESEM image of Sample S11 and its particle size distribution are shown in Figure 4.6 (a (i)) and Figure 4.6 (b (i)), respectively. The silver thin film thickness is ~8 nm. The resulting average nanoparticle size is ~ 26 nm while the particle density is 223 μm^2. The average gap between nanoparticles is around 100 nm, which is relatively large. The particle density is very low given the average size of the

nanoparticles. In addition, the nanoparticle shape is also not homogeneous when compared to other previous samples.

The FESEM image for Sample S12 is shown in Figure 4.6a (ii) and its particle size distribution shown in Figure 4.6 (b (ii)). The silver thin film thickness is ~15 nm. The average nanoparticle size is ~ 23 nm with increased particle density of 382 μm^2. For Samples S13 to S15; however, no distinct nanoparticle structures are observed, as shown in their FESEM images in Figure 4.6 (a (iii) - a (v)). The layers appeared to be granular structure with limited spacing between each other. There are two possibilities leading to this observation. The first one is because of the silver thin film are not having sufficient temperature-duration product to achieve significant thermal dewetting process. The second is being agglomeration of nanoparticles formed after thermal dewetting (Hsu & Wu, 2010a; Lee et al., 2014). Both phenomena originate from the relatively thick silver thin film. Note that the initial thickness of silver thin film for Sample S13 to S15 ranges from ~25.9 nm to ~43.6 nm. The latter being more than 5 times the thickness for Sample S11. As the annealing duration after silver thin film deposition is only 2 hours, it is believed that the first mechanism is responsible for the lack of formation of nanoparticle. The consequence of this result is that LSPR effect is expected to be very small in Sample S13 – S15. From the analysis of Sample S11 – S15, it can be concluded that hybrid gold/silver nanoparticle layer can be formed with silver thin film thickness of less than ~25 nm. The best surface morphology is obtained with ~15 nm silver thin film, where distinct nanoparticle structure is formed with high particle density. The FESEM analysis results are summarized in Table 4.2.

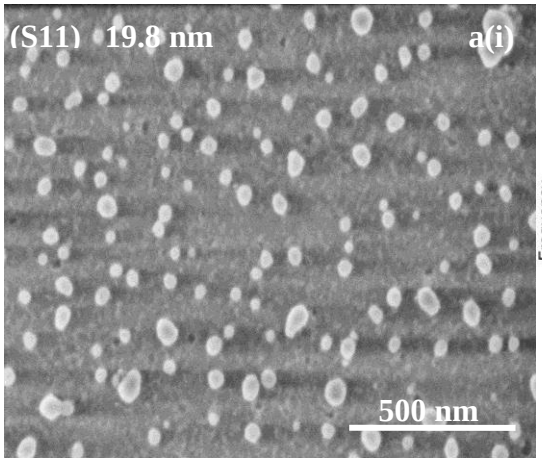

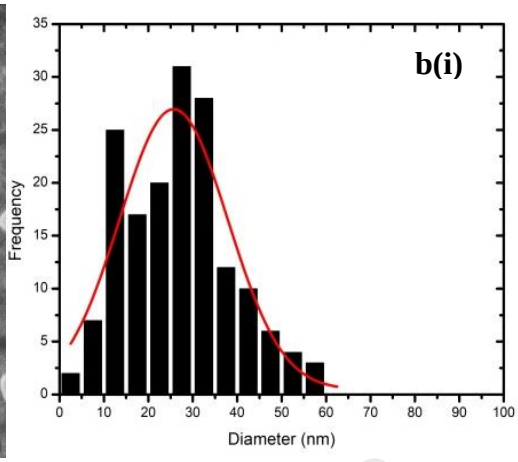

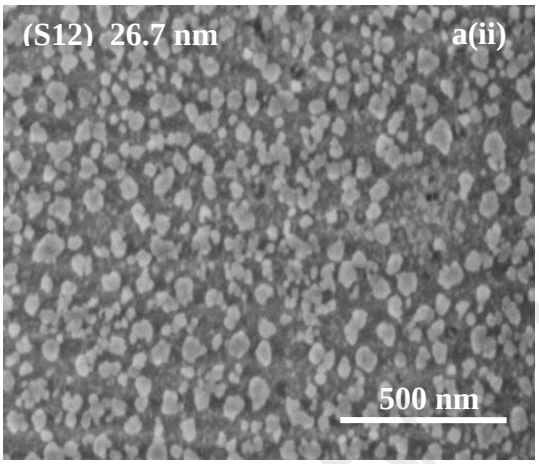

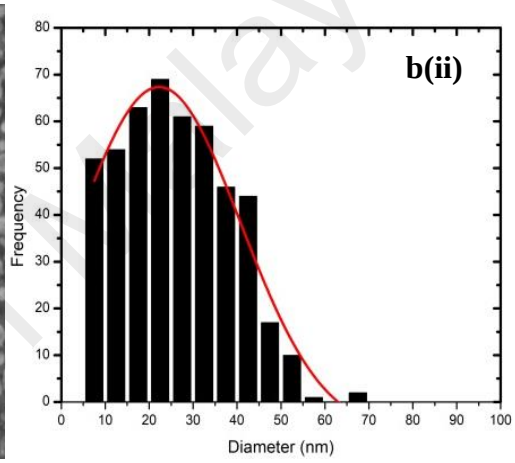

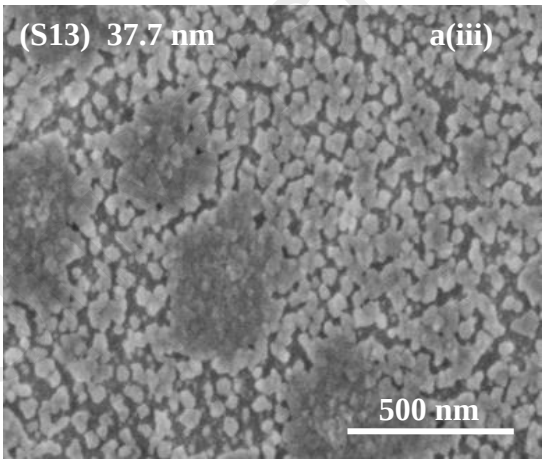

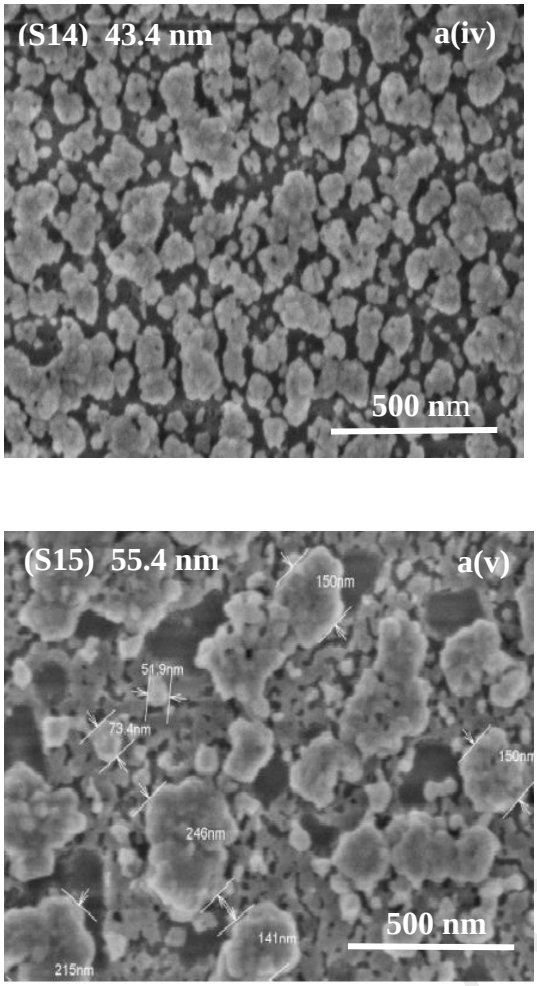

Figure 4.6: FESEM images of S11 a (i) to S15 a(v) two layers of nanoparticle with different thicknesses.

Table 4.2: Specifications of metal nanoparticles for Samples: S1 to S15 Samples have different material types with different layers of thicknesses

Material	Samples	Sample Thickness (nm)	Average Size of Particles (nm)	Average of nanoparticle distribution in (500 x 500) nm^2	Density (μm^2) = average of nanoparticle per area (500 x 500) nm^2
Gold nanoparticles annealing at temperature of 600^oC for 4 hours					
Gold (Au)	S1	4.2	11	289	1155 ± 17
Gold (Au)	S2	4.9	12	195	779 ± 6
Gold (Au)	S3	7.7	25	109	437 ± 12
Gold (Au)	S4	9.7	33	57	229 ± 4
Gold (Au)	S5	13.4	45	31	127 ± 4
Silver nanoparticles annealing at temperature of 270 ^oC (2 hours for Ag)					
Silver (Ag)	S6	8	9	287	1147 ± 14
Silver (Ag)	S7	18.4	13	239	955 ± 15
Silver (Ag)	S8	30	29	82	327 ± 12
Silver (Ag)	S9	40	37	62	245 ± 16
Gold/silver nanoparticles annealing at temperature of 600^oC(2 hours for Au) and 270 ^oC (2 hours for Ag) with variation of silver thickness					
Gold (Au)	S10	11.8	23	96	384 ± 5
Gold and Silver (Au & Ag)	S11	11.8 and 8	26	56	223 ± 9
Gold and Silver (Au & Ag)	S12	11.8 and 14.9	23	96	382 ± 11
Gold and Silver (Au & Ag)	S13	11.8 and 25.9	NA	NA	NA
Gold and Silver (Au & Ag)	S14	11.8 and 31.6	NA	NA	NA
Gold and Silver (Au & Ag)	S15	11.8 and 4 3.6	NA	NA	NA

4.2 Energy Dispersive X-Ray (EDX) analysis

Energy dispersive X-ray (EDX) analysis was carried out to verify the elementary composition of selected metal nanoparticle of samples S7, S10 and S11. For each sample, single point EDX analysis is carried out on a number of nanoparticles within the layer. The respective EDX spectrums are shown in Figure 4.7 to 4.10. For comparison, the EDX spectrum of microscope glass substrate is also observed and is shown in Figure 4.7. The EDX spectrum of the glass slide consists of peaks corresponding to elements of calcium, oxygen, sodium, magnesium, aluminum and silicon, which are the characteristic elements of soda lime glass (Adekoya et al., 2012;

Colak & Aral, 2005). The EDX spectrum of Sample S7 (Ag-NPs), as shown in Figure 4.8, show Ag-peaks at 2.98 keV, with no characteristic peak for gold. EDX spectrum for samples S10 (Au-Nps) is shown in Figure 4.9. The spectrum shows the existence of Au-peaks at 2.12 keV with no characteristic peak for silver. On the other hand, Figure 4.10 shows EDX spectrum of both Au-peak at 2.12 keV and Ag-peak 2.98 keV, which confirms the existence of both gold and silver elements in the hybrid gold/silver nanoparticles.

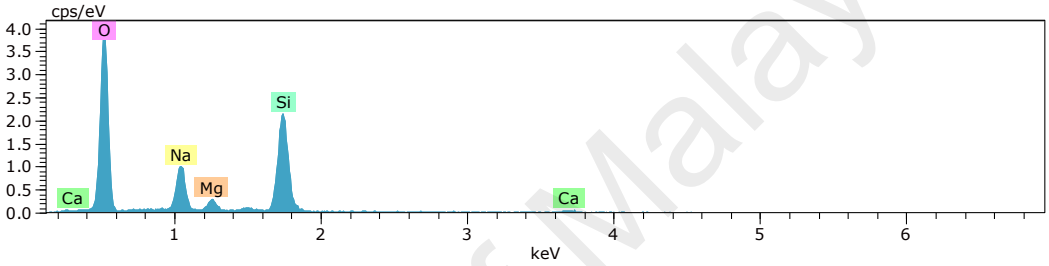

Figure 4.7: EDX spectrum analysis of microscope glass.

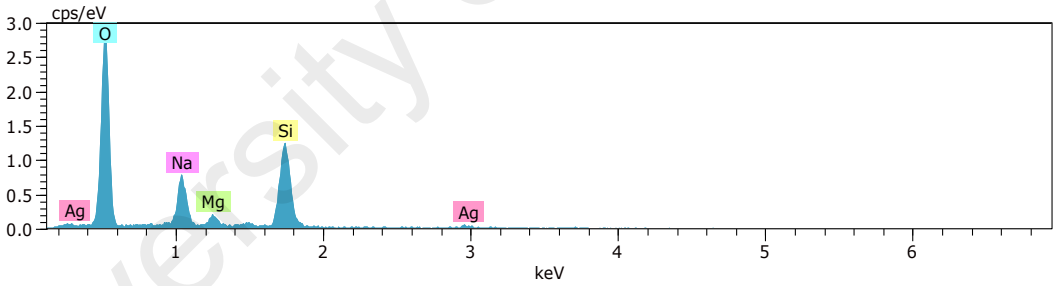

Figure 4.8: EDX spectrum analysis of S7 (Ag-NPs).

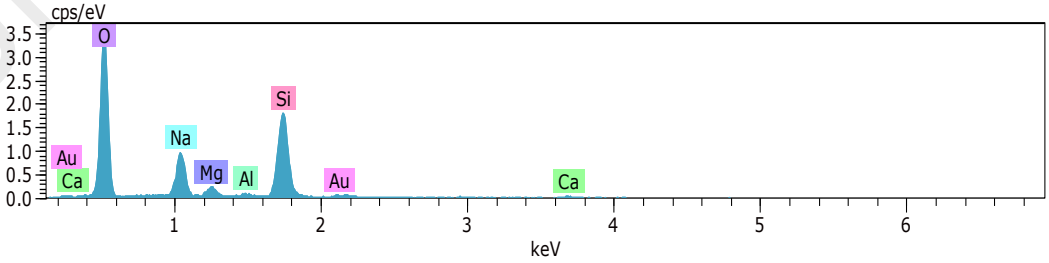

Figure 4.9: EDX spectrum analysis of S10 (Au-NPs).

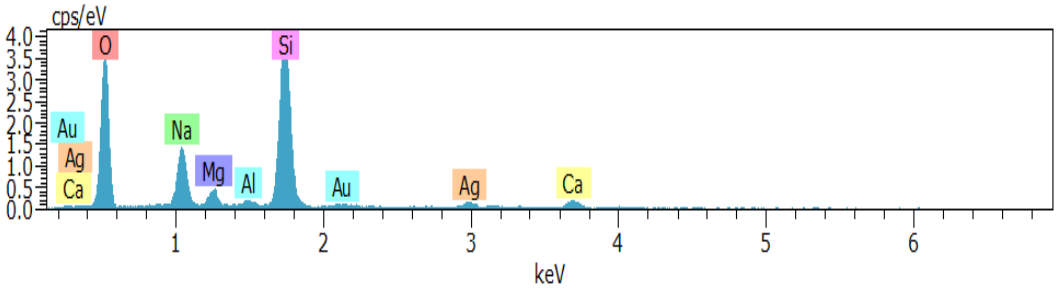

Figure 4.10: EDX spectrum analysis of S11 (Au-NPs and Ag-NPs) .

4.3 UV-VIS-NIR spectroscopy of nanoparticle layers

The UV-Vis-NIR absorption spectra of metal nanoparticles layers are recorded using Lambda 750 Perkin Elmer spectrometer. The absorption spectra for gold nanoparticle samples (S1-S5) are shown in Figure 4.11. The samples show resonance wavelength increasing gradually from 540 nm to 545 nm, 550 nm, 560 nm and 600 nm for sample S1, S2, S3, S4 and S5, respectively.

The increase in resonance wavelength corresponds to the increase in the average size of nanoparticle of 11 nm, 12 nm, 25 nm, 33 nm and 45 nm, respectively. The relationship between LSPR resonance wavelength and gold nanoparticle size is shown in Figure 4.12 and appears to be linear. A better linear fit is seen when the nanoparticle size is compared to the corresponding LSPR absorption width.

The increase in resonance wavelength lead to the increase in the Full Width at Half Maximum (FWHM) shown increases of 85 nm, 105 nm, 121 nm, 140 nm and 277 nm for sample S1, S2, S3, S4 and S5, respectively. The relationship between LSPR resonance wavelength and FWHM shown in Figure 4.13 and appears to be linear.

The FWHM was shown to increase of the 85 nm 105 nm, 121 nm, 140 nm and 277 nm corresponding to the increase size in the average nanoparticle of 11 nm, 12 nm, 25 nm, 33 nm and 45 nm for the samples of S1, S2, S3, S4 and S5, respectively. The

relationship between FWHM and average nanoparticle shown in Figure 4.14 and appears to be linear.

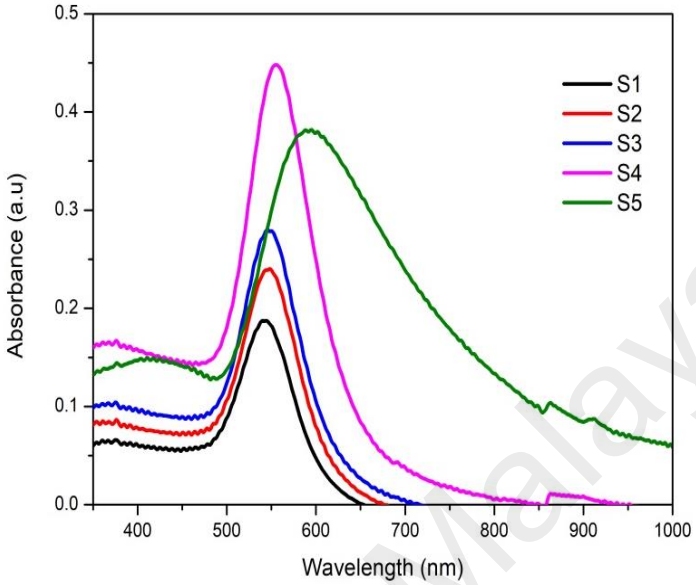

Figure 4.11: Spectrum of SPR for layers of S1 to S5 (4.2 nm, 4.9 nm, 7.7 nm, 9.7 nm and 13.4 nm) metallic nanoparticles.

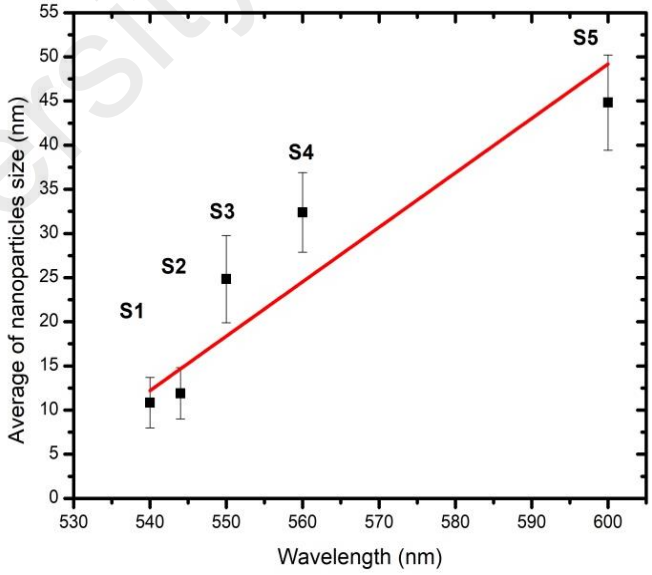

Figure 4.12: Graph of the relationships between wavelength and average size of nanoparticle of S1 to S5.

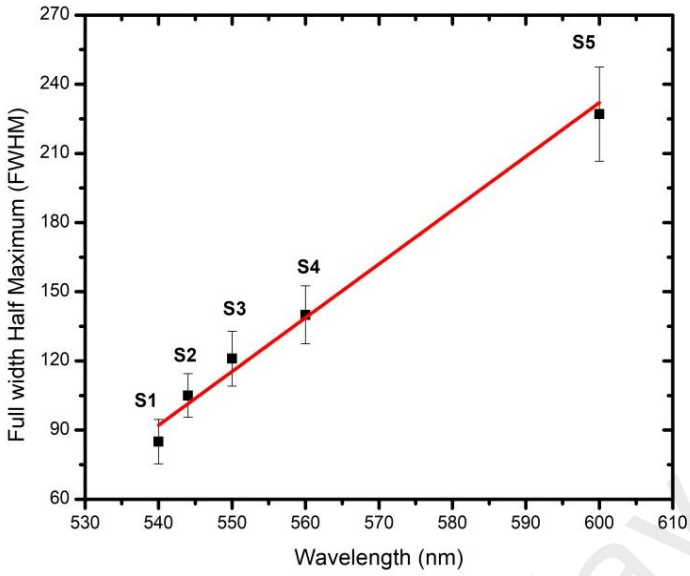

Figure 4.13: Graph of the relationship between wavelength and FWHM of S1 to S5.

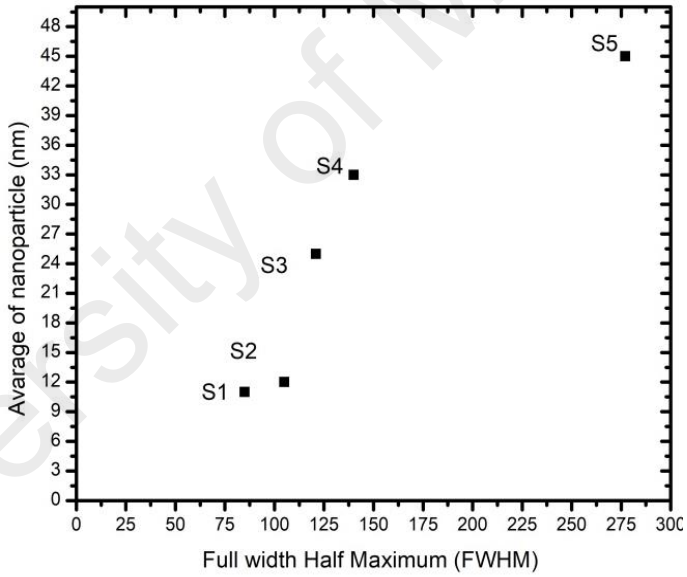

Figure 4.14: Graph of the relationships between FWHM and average size of nanoparticle of S1 to S5.

The absorption spectra for silver nanoparticle samples (S6-S9) are shown in Figure 4.15. The S6 shows peak absorption at 415 nm, S7 show peak absorption at 430 nm, S8 show peak absorption at 440 nm and S9 show peak absorption at 425 nm. The clearly plasmonics effect appears on the thickness between 5nm to 25 nm as shown in Figure

4.15. The samples S6, S7 and S8 shows the red shift while S9 (40 nm) not showing any plasmonics behaviors. It can also be seen that the absorption wavelength increasing corresponding to the increment in silver nanoparticle sizes of 9 nm, 13 nm, 30 nm and 37 nm for Samples S6, S7, S8 and S9 respectively. The relationship between LSPR resonance wavelength and silver nanoparticle sizes is shown in Figure 4.16. The value of wavelength based on FWHM shown the increment of 235 nm, 250 nm, 290 nm and 445 nm as depicts in Figure 4.17. Figure 4.18 shows the average of nanoparticles sizes for Sample S6 to Sample S9 for silver nanoparticles against FWHM. It can be concluded that the increment of silver nanoparticles will affects the FWHM of the LSPR spectrum.

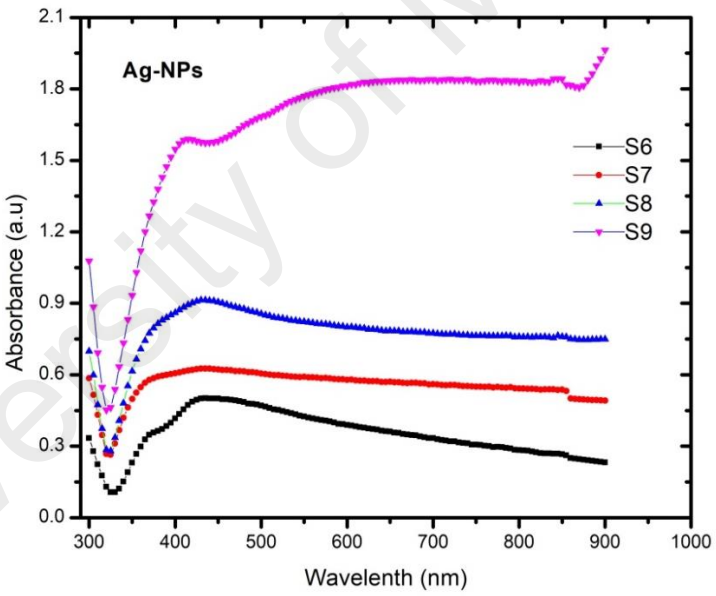

Figure 4.15: Spectrum of SPR of S6 (8 nm), S7 (18.9 nm), S8 (30 nm) and S9 (40 nm) layers.

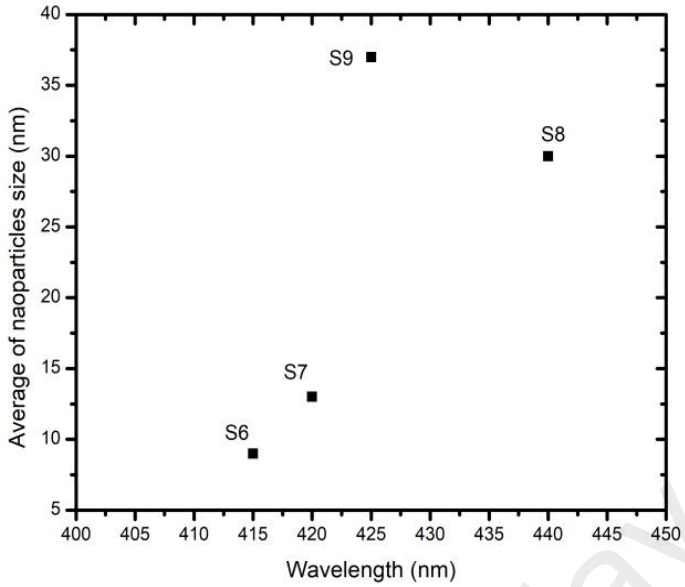

Figure 4.16: Graph shows the relationships between wavelength and average size of silver nanoparticle of S6 to S9.

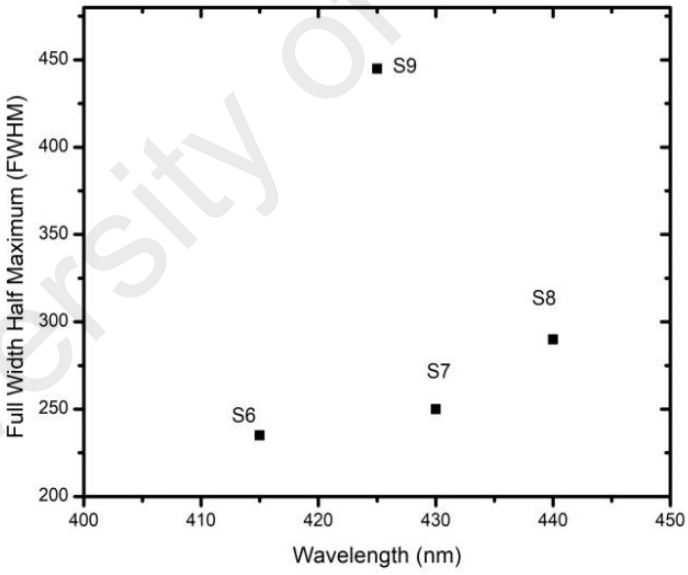

Figure 4.17: Graph shows the relationships between FWHM and wavelength and for S6 to S9.

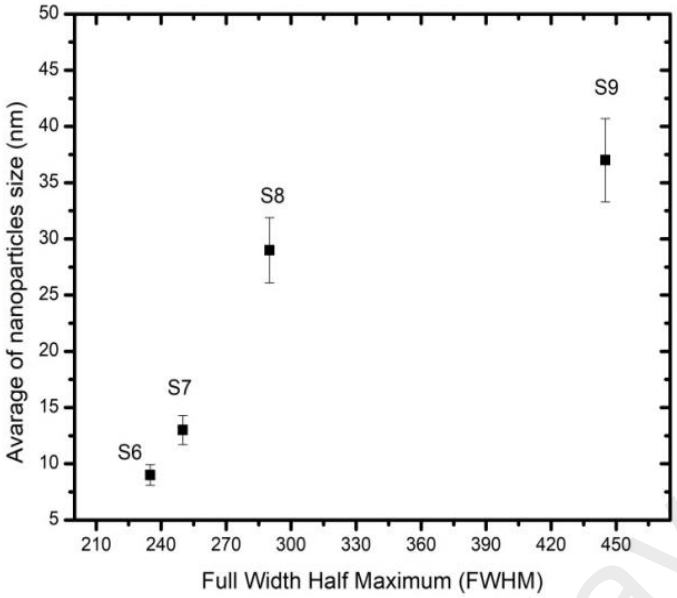

Figure 4.18: Graph shows the relationships between FWHM and average size of nanoparticle for samples S6 to S9.

Figure 4.19 shows the characteristic of the NPs of Sample S10where their absorption in the UV–Vis-NIR region due to LSPR. The UV–Vis-NIR spectra of nanoparticles layers for S10 occur at ~ 540 nm and the FWHM for S10 is ~ 200 nm.

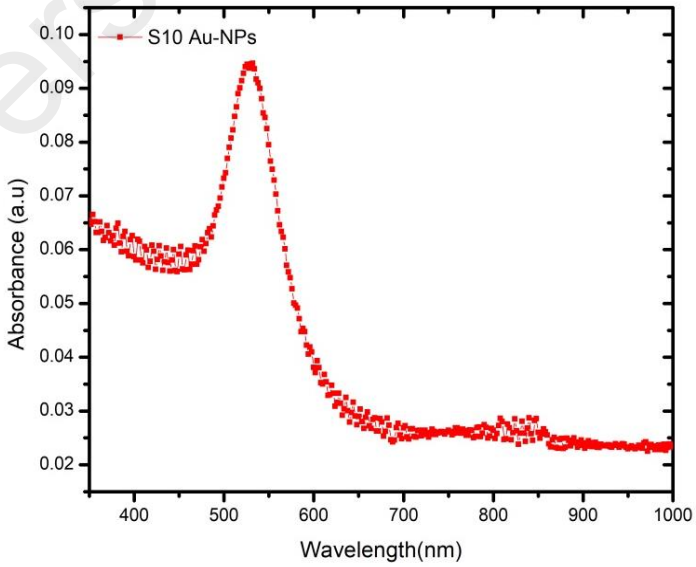

Figure 4.19: Spectrum of LSPR for layers of NPs of sample S10.

The hybrid nanoparticles represent (S11 to S15) and single layer of gold and silver nanoparticle represent (S7 and S10). The UV–VIs-NIR spectra of nanoparticles layers layers show in Figure 4.20 where: S11 occur at ~ 440 nm and S12 occur at ~ 520 nm. The FWHM of S11 shows at ~ 125 nm and S12 shows at ~ 140 nm. S12 shows significant increment in for FWHM. The S12 produces a stronger plasmon resonance compare to S11 due to the SPR occurs at energies that are distinct from any bulk inter-band transitions. The plasmon resonance of S11 and S12 appears between S10 (gold) absorption and S7 (silver) absorption and show enhancement in absorption peak due to manipulating the nanoparticles sizes (Mezher, Chong, & Zakaria, 2016b). It is commonly known that the plasmonics band of metal nanoparticles is due to the oscillations of free electrons which occupy energy states near the Fermi level in the conduction band. The experimental result agrees with the Mie theory discussed in Chapter 2. This theory states that red-shifting and broadening of the resonance peak are associated with the increase in the size of the nanoparticle (Singh & Aghamkar, 2014).

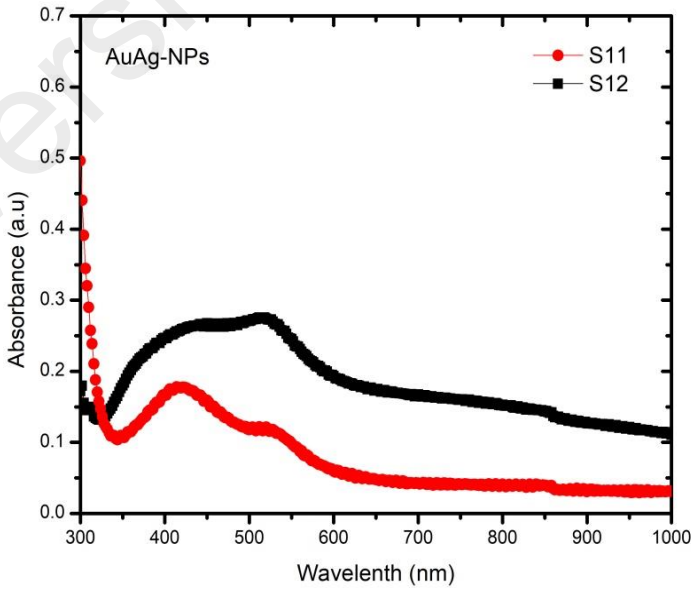

Figure 4.20: Spectrum of LSPR for layers of NPs of S11 to S12. The different absorption peaks, related to the samples with different thicknesses.

4.4 Nonlinear absorption and nonlinear refraction of metal nanoparticle layers

Before nonlinear absorption (NLA) and nonlinear refraction (NLR) can be measured, the linear absorption of the sample needs to be determined first. The linear absorption measurement setup is shown in Figure 4.21. The setup is the same as open-aperture Z-scan setup. However, the sample is fixed at a position in the laser beam path away from the focal point (low intensity) to avoid excitation of NLA and NLR effects.

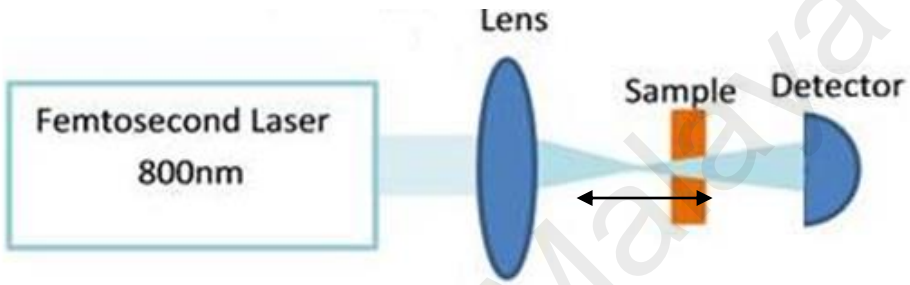

Figure 4.21: Schematic diagram of open aperture Z-Scan technique.

The Equation for linear absorption, α, is shown in Equation (4.1)

$$\alpha = \frac{-1}{L}\, ln(\frac{p}{p0}) \qquad (4.1)$$

where p is the power transmitted through a sample containing nanoparticle layer, and p_0 is the power transmitted through the substrate material without the nanoparticle layer. The sample thickness, L is determined by measuring the nanoparticle height using a surface profiler (DEKTAK D150). The linear absorption for the different metal nanoparticles samples are tabulated in Table 4.3.

Another important parameter in the calculation of NLA and NLR coefficient is the effective thickness of the sample, L_{eff}. L_{eff} can be calculated from the linear absorption coefficient as shown in Equation (4.2). (Ara, Dehghani, & Iranizad, 2008):

$$l_{eff} = \frac{1-e^{-\propto L}}{\propto} \quad (4.2)$$

For measurement of nonlinear optical interaction, the sample is translated along the laser beam propagation direction (z-axis) where the laser focal point is set as z = 0. In the open-aperture Z-scan setup in Figure 4.21, the measured transmittance of the nanoparticle samples will be reduced as the sample is translated through the laser focal point due to NLA by the sample. The transmittance profiles of gold nanoparticle layers (sample S3, S4 and S5) are shown in Figure 4.23(a). It can be seen that the open aperture transmittance is symmetric in relation to the focal point $Z = 0$. The NLA coefficient (β) can then be determined by measuring the peak-valley value, $\Delta T_{(z)}$ of the transmittance profile.

The NLA coefficient (β) is calculated using Equation (4.3):

$$\beta = \frac{2\sqrt{2}}{I_O L_{eff}} \Delta T_{(z)} \quad (4.3)$$

The close-aperture Z-scan is shown in Figure (4.22). An aperture is inserted near the detector to cut out a portion of transmitted light incident upon the detector. For close-aperture Z-scan setup, both NLA and NLR effects will be measured. The close-aperture Z-scan transmittance profile is then analyzed together with open-aperture Z-scan transmittance profile to determine the NLR coefficient.

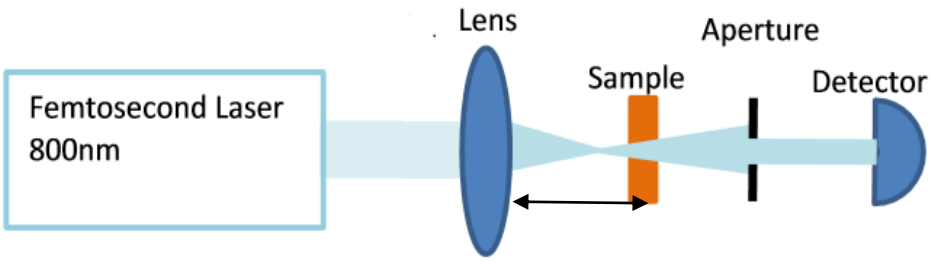

Figure 4.22: Schematic diagram of close aperture Z-Scan technique.

In this case a second parameter in introduced which is the ***S*** parameter. It is the normalized transmittance parameter and is represented by Equation 4.4:

$$S = 1 - exp\left(\frac{-2r_a^2}{w_a^2}\right) \tag{4.4}$$

where r_a is the radius of the aperture and w_a is the beam radius at the aperture**.**

For open aperture Z-scan measurement, ***S*** is equal to unity *(S=1)* since all transmitted light is measured by the detector. Whereas for close-aperture Z-scan measurement, S parameter varies from 0.25 – 0.45 due to the requirement for ***S*** value to be between $0 \leq S \leq 0.5$.

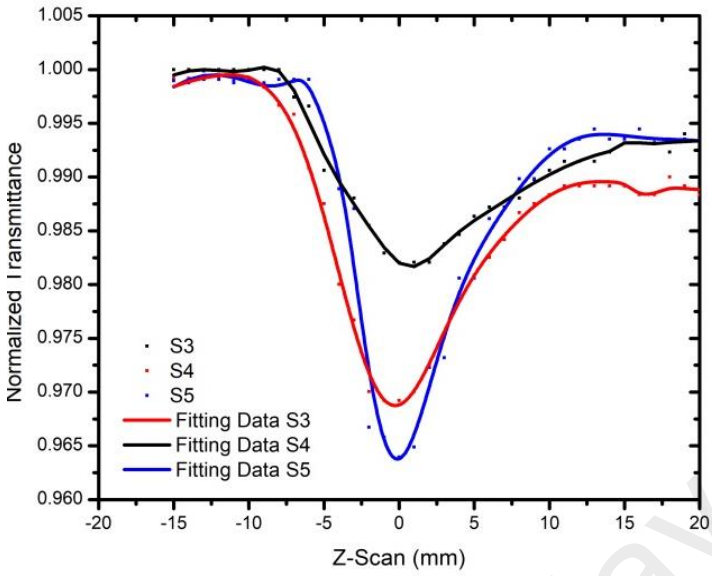

(a)

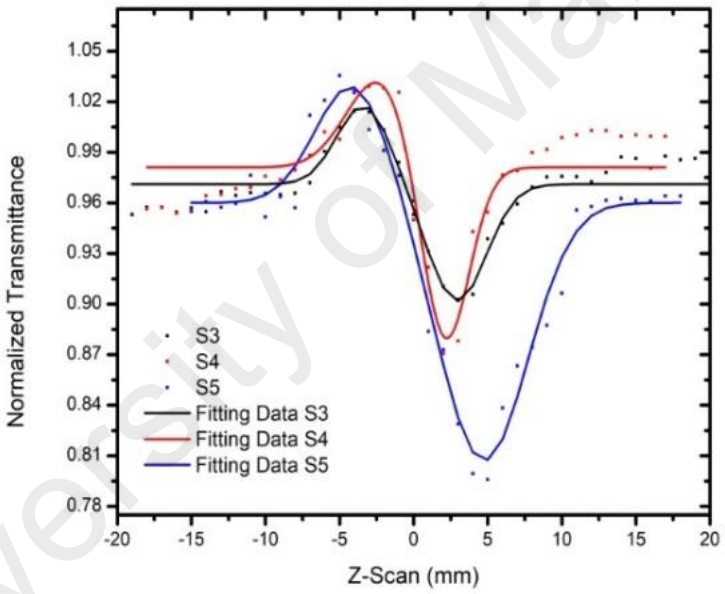

(b)

Figure 4.23: Open- aperture (a) and Closed-aperture (b) of Z-scan curve for samples S3, S4, and S5 with different exposure times.

The close-aperture Z-scan measurement profiles of gold nanoparticle layers after considering the NLA effect are shown in Figure 4.23(b). It can be seen that the transmittance first increases when it is close to the laser focal point before reducing to a level lower than the linear transmission. The transmittance then returns to the linear transmittance level as the sample is translated away from the laser focal point. As the

valley of the transmittance profile trails the peak, the sign of nonlinear refractive index change is negative and leads to self-defocusing of the laser beam. The sample acted as thin lens during scanning through the focal plane. In this case, the post focal peak and valley is a clear indication of negative lens (Mezher, Nady, Penny, Chong, & Zakaria, 2015). The different peak-valley values $\Delta T_{(p-v)}$ indicates different degree of NLR of the samples studied. The phase distortion $\Delta\Phi^o$ can be calculated from the differences between the normalized transmittance peak and valley, ΔT_{p-v} as shown in Equation (4.5):

$$\Delta T_{(p-v)} = 0.406(1-s)^{0.27}\,\Delta\phi° \qquad for\ \Delta\phi° < \pi\ (2) \tag{4.5}$$

The nonlinear refractive index, n_2, can then be obtained from Equations (4.6) (Hamanaka, Hayashi, Nakamura, & Omi, 2000) :

$$\Delta\phi^o = \frac{2\pi L_{eff} n_2 I_0}{\lambda} \tag{4.6}$$

Table 4.3 show values of β and n_2 of gold nanoparticle layers. S3 show a lower β of 2.26 x 10^{-4} cm W^{-1} while S4 and S5 show increasing value of β of 2.58 x 10^{-4} cm W^{-1} and 2.62 x 10^{-4} cmW^{-1} respectively. S3 has a nonlinear refractive index of n_2 of -1.77 x 10^{-8} cm^2W^{-1} and n_2 increases to -1.82 x 10^{-8} cm^2W^{-1} and 2.16 x$10^{-8}cm^2W^{-1}$: for samples S4 and S5 respectively. The relationship between (NLA and NLR) with gold nanoparticles density shown in Figure 4.24, the increase in NLA corresponds to the decrease in the density of nanoparticle of 437 μm^2, 229 μm^2 and 127 μm^2 respectively shown in Figure 4.24 (a). The increment in NLA is due to increasing the thickness of metal and this relation was mention in Figure 4.16. The S5 with thickness of 13.4 nm shown higher absorption than S4 (9.7nm) and S3 (7.7nm). The decrease in NLR corresponds to the decrease in the density of nanoparticle of 437μm^2, 229μm^2 and 127μm^2 respectively. The decrease in NLR shown in Figure 4.24(b) due to decreasing

the average of nanoparticle, the S5 with thickness (13.4nm) shown higher absorption than S4 (9.7nm) and S3 (7.7nm).

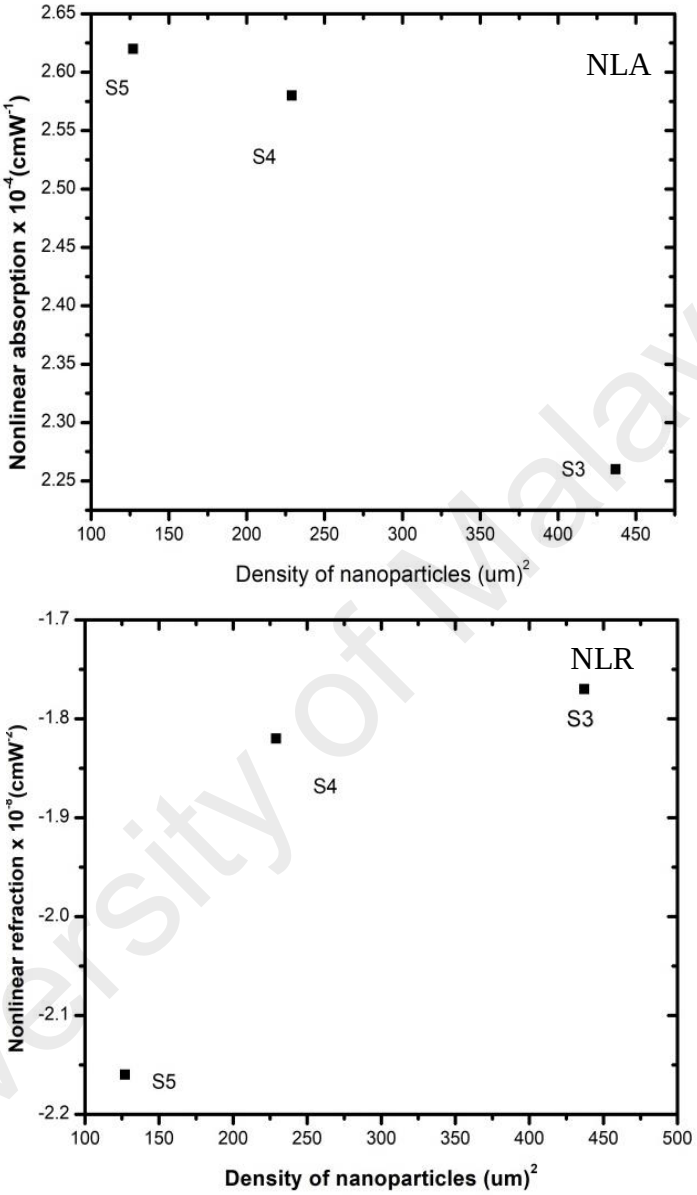

Figure 4.24: Graph shows the relationships between NLA and NLR for gold nanoparticles for samples S3 to S5.

The relationship between (NLA and NLR) with gold nanoparticles density is shown in Figure 4.25, where it is evident that the increase in NLA corresponds to the increase in the size from nanoparticle of 25 nm to 45 nm Figure 4.25(a). The increase in NLA due to increasing the thickness of metal and this relation was mention Figure 4.16.

Sample S5 with thickness of 13.4nm shows higher absorption than S4 (9.7 nm) and S3 (7.7 nm). The decrease in NLR corresponds to an increase in the size of nanoparticle as shown in Figure 4.25 (b) and due to decrease in the average size of nanoparticle.

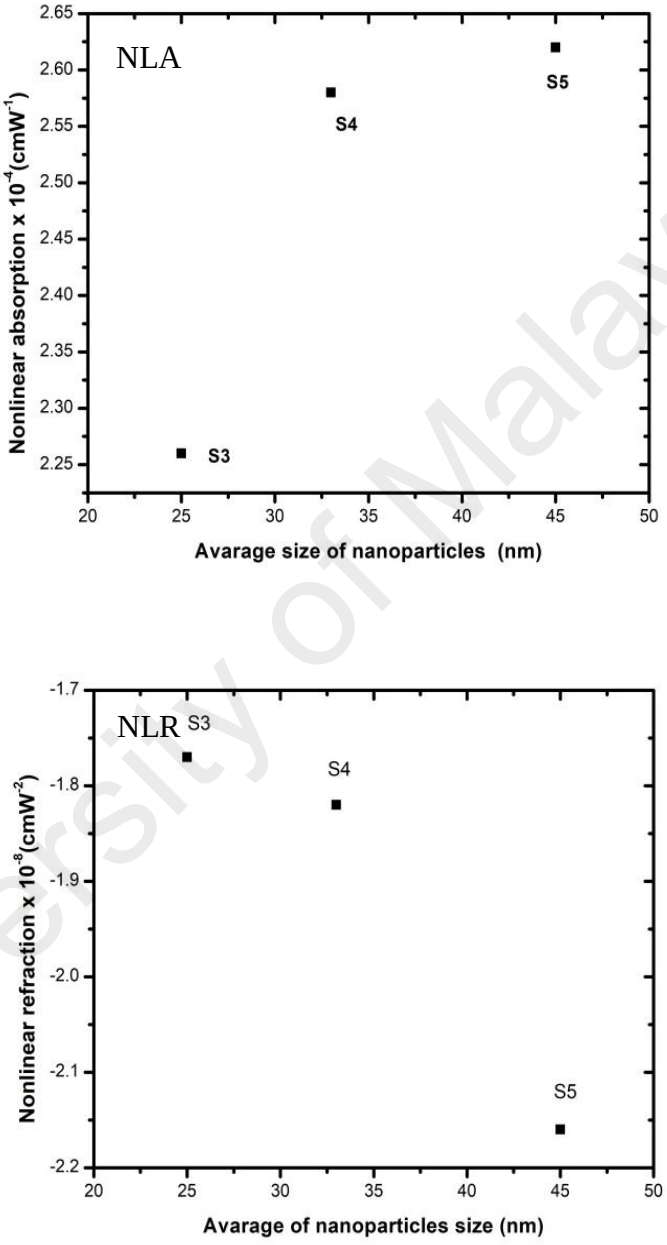

Figure 4.25: Graphs show relationship between NLA and NLR with average size of nanoparticle for S3 to S5.

Figure 4.26(a) illustrates the open-aperture Z-scan transmittance profile of sample S7, S10 and S11, which are layers of gold, silver and gold/silver, respectively. Linear

absorption level at the beginning and end is significantly different due to nanoparticle size and focal length of lens.

The nonlinear absorption coefficients of the different layers of NPs of S7, S10 and S11 are determined by the indicative shift of the deep $\Delta T_{(z)}$. Their respective nonlinear absorption coefficients show in Table 4.3 at the end of this section.

The S7 and S11 show a different trend compared to S10 that show lower absorption $1.74x10^{-4}$ cm W^{-1} while S7 show the absorption of 4.87 $x10^{-4}$ cm W^{-1} and the S11 of value 3.87 $x10^{-4}$ cmW^{-1} show the enhancement to absorption. The size of nanoparticles have significant effect on the $\Delta T_{(z)}$ due to absorption at the focal point.

For the evaluation of the refractive index (n_2) of samples S7, S10 and S11: NPs thin films are depends on the closed-aperture measurements are performed and normalized transmittances are performed, as shown in Figure 4.26 (b).

The close-aperture Z-scans shows transmission peaks followed by valleys near the focal point, which are asymmetric in trend. The samples S7, S10 and S11 of NPs films reveal post focal peak and valley, which is a clear indication of negative lens effect of n_2 (Henari, 2001; Mezher et al., 2016b; Mezher et al., 2015).

The S7 show lower refractive index of n_2 is $-3.21x10^{-9}$ cm^2W^{-1} due to the value of peak and valley transmittances (T_p-T_v). Sample S7 shows increasing value of refractive index n_2 as $-7.94x10^{-9}$ cm^2W^{-1} and sample S11 is also shows increasing value of n_2 as -5.84×10^{-9} cm^2W^{-1} due to the increasing size of nanoparticles. These different sizes of nanoparticles shows the nonlinear effect can be enhances due to increasing sizes of nanoparticles due to ($T_p - T_V$).

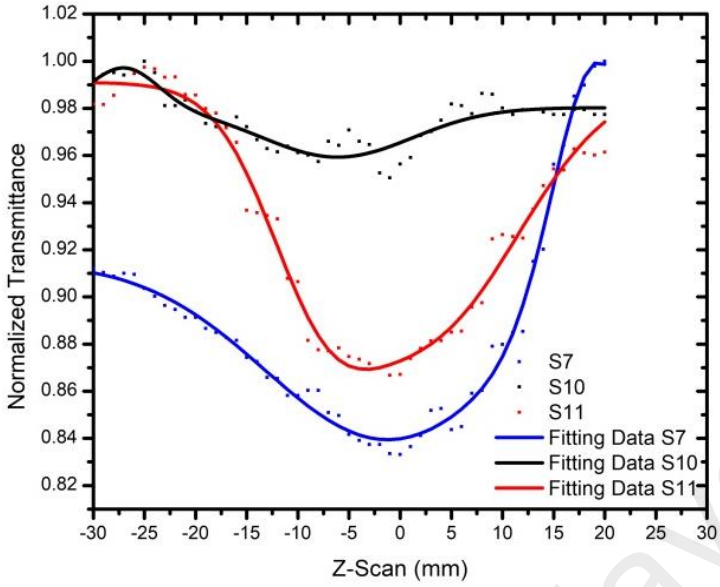

(a)

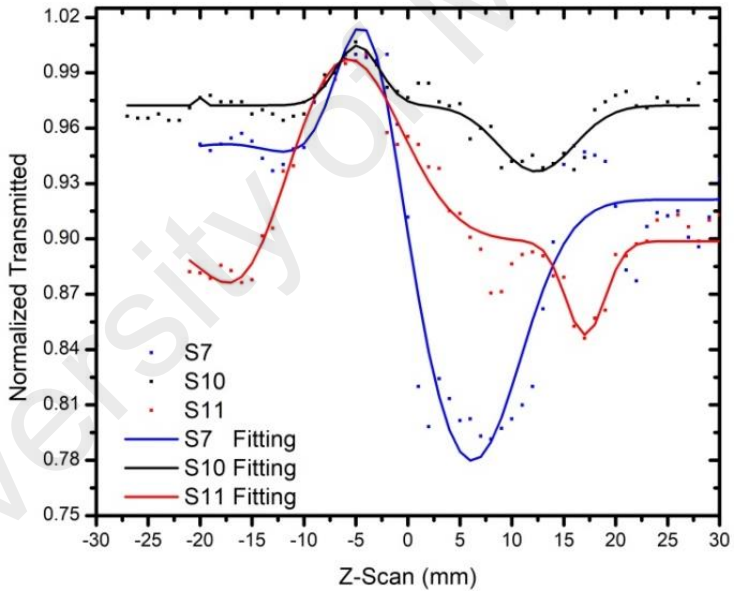

(b)

Figure 4.26: Open-aperture (a) and close-aperture (b) Z-scan curves for samples S7, S10 and S11 respectively.

Table 4.3: Nonlinear Refractive Index and Nonlinear Absorption Coefficient for sample S3 to S11 Sample.

Samples	PI(mW)	λ (nm)	w_o (μm)	I_0 ($MWcm^{-2}$)	α (cm^{-1})	$\Delta\Phi_0$	n_2 (cm^2W^{-1})	β (cmW^{-1})
S3	11	800	11.9	329.35	1.63×10^5	0.33	-1.77×10^{-8}	2.26×10^{-4}
S4	11	800	11.9	329.35	1.57×10^5	0.42	-1.82×10^{-8}	2.58×10^{-4}
S5	11	800	11.9	329.35	1.93×10^5	0.66	-2.16×10^{-8}	2.62×10^{-4}
S7	33	800	15.28	548.462	17.3×10^4	0.61	-7.94×10^{-9}	4.87×10^{-4}
S10	33	800	15.28	548.462	5.7×10^4	0.19	-3.21×10^{-9}	1.74×10^{-4}
S11	33	800	15.28	548.462	21.6×10^4	0.44	-5.84×10^{-9}	3.87×10^{-4}

CHAPTER 5: FABRICATION OF ARBITRARY PLASMONICS STRUCTURES AND THEIR NONLINEAR OPTICAL ANALYSIS

5.1 Introduction

In this section we present studies of using different shape of metallic structures to determine plasmonics behaviour from their shape. Different techniques and parameters have been applied to fabricate these arbitrarily shape of nanostructures (NSs). We will investigate effects of plasmonics structures using platinum and silver and other non plasmonics materials like nitrogen doped graphene and graphene oxides material. The obtained result will be observed into three categories, FESEM characterization of the samples, SPR characterization and nonlinear optics studies for these nano-structures. Four different groups of nanostructures layers have been prepared as listed below:

- Fabrication and characterization of platinum nanostructures (Pt- NSs).
- Fabrication and formation studies of Silver-Micro-Flower-Structure (Ag-MFS).
- Nitrogen doped graphene structures.
- Graphene Oxides.

The fabrication and formation of all of these structures will be describes experimentally and all these structures will also be used in the nonlinear optical measurement.

5.2 Fabrication and characterization of arbitrarily plasmonics structures

5.2.1 Platinum nanostructures (Pt-NSs)

Controllable fabrication of platinum nanostructures was experimentally demonstrated via electrodeposition in the liquid crystalline phase to form different structures. Electrodeposition process has taken place using a buffer solution of Pt $(NH_3)_2OH$ at pH 5.8. The electrochemical deposition of Pt-NSs was performed in a one-electrode electrochemical cell by chronoamperometry at -0.6 V, in connection with

Pt/PtCl reference electrodes. The ITO electrode was used as the working electrode and a platinum foil with an area of 2 cm^2 was used as the counter electrode. The solution containing 40 mM Pt $(NH_3)_2OH$ concentrations were prepared by adding ammonia (1 wt%) to a 50 mM platinum solution until the complete dissolution of the precipitates was achieved. Distilled water at a volume ratio of 1:12 (Pt $(NH_3)_2OH$: water) was subsequently added for the chronoamperometric deposition of the Pt-NSs on ITO electrode for 10 minutes. The final product (Pt-NSs) then washed using distilled water and dried at 50 ºC in a conventional oven.

JEOL JBM-7600F FESEM machine to analyze the morphology of the synthesis Pt-NSs as shown in Figure 5.1. A low-magnification image of electrodeposited synthesized Pt-NSs shown in Figure 5.1 shows randomly formed platinum structures Figure 5.1 (a) where it can be seen that structures consist of a single particle with 'dome' like as depicts in Figure 5.1 (b). It is believed that this structure formed due to the cooperative effect of the liquid crystalline phase soft template and self-assembly of Pt. Figure 5.1 (b) reveals that two platinum structures may are sit together, which is prominent disadvantage of applying chemical techniques to control spacing between structures. Therefore, based on these structures, we estimated the structures could be close to 30 nm.

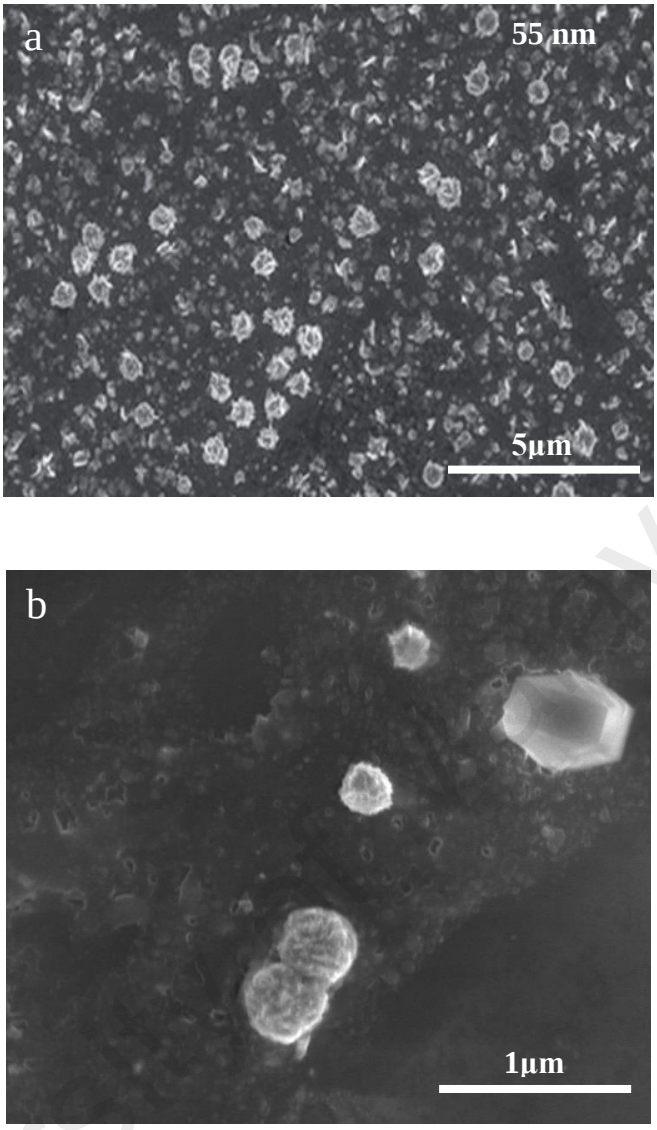

Figure 5.1: FESEM images of Pt-NSs, (a) show distribution structures on ITO (b) images of 'dome' like structure of platinum.

The UV-VIS absorption spectra of Pt-NSs films are shown in Figure 5.2, the peak absorption of Pt-NSs layer is dissimilar among the Samples, which can be attributed to the absorption of Pt-NSs thus further red-shifting the absorption peaks at 281 nm. The UV–VIS spectra initially confirm S1 present LSPR. The absorption spectrum of the Pt-NPs was synthesized at low concentration of Pt $(NH_3)_2OH$, with peak at 281 nm.

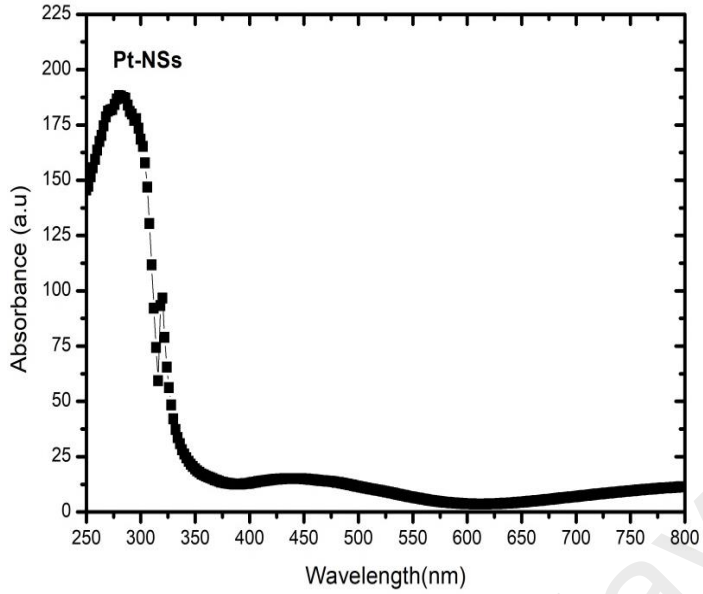

Figure 5.2: Spectrum of SPR for layers of Pt-NSs absorption peaks, related to the samples having resonance oscillation.

Energy Dispersive X-Ray (EDX) analysis was carried out to verify the elementary composition of selected materials Pt-NSs, determine the elemental compositions of the structures on the substrate. Platinum, sodium, magnesium, silicon, carbon and oxygen were the elements that could be detected. Silicon contributed to the spectrum owing to the composition of the substrate and the presence of sodium and magnesium was possibly due to the chemical process. The carbon and oxygen signals were most probably due to capping agents on the surfaces of nanostructures. Figure 5.3 shows EDX spectrum of Sample S1 at 2.1 keV, 8.3 keV, 9.5 keV, 10 keV, 11.2 keV and 13.1 keV which confirms the existence of platinum element.

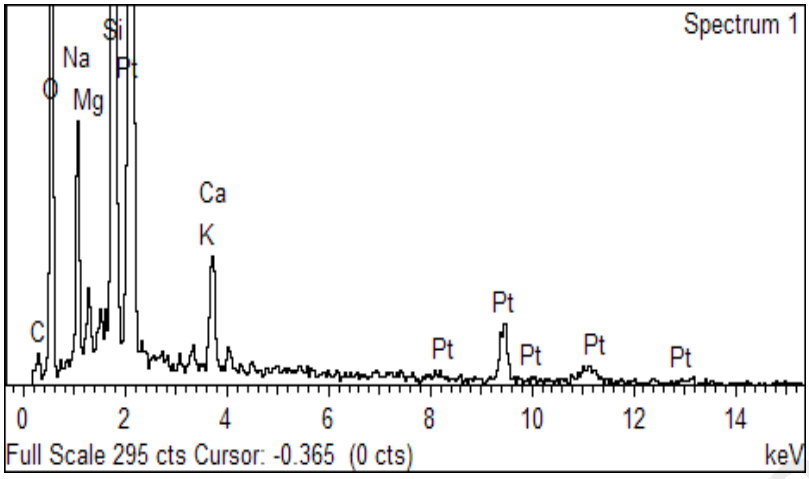

Figure 5.3: EDX analysis spectrum of platinum nanostructures (Pt-NSs).

5.2.2 Silver micro-flower structures (Ag-MFs)

Silver with flower-like structures at micro-scale size (Ag-MFS) has been fabricated using the electrochemical deposition technique. The electrochemical deposition of Ag-MFs has been performed in a three-electrode electrochemical cell by chronoamperometry at -0.6V with respect to Ag/AgCl as reference electrodes. The Indium Tin Oxide (ITO) electrode used as the working electrode and platinum foil of 2 cm^2, was used as counter electrode. A solution containing 40 mM Ag $(NH_3)_2OH$ was prepared by adding ammonia (1 wt. %) to a 50 mM silver nitrate solution. Distilled water was then added at a volume ratio of 1:12 (Ag $(NH_3)_2OH$: water) was subsequently added for chronoamperometric deposition of AgMF-modified electrode at (10, 15 and 45) min deposition times. The final products (Ag-MFS) residing on the ITO electrode was washed to eliminate any impurities and then dried at 50 ^0C in a conventional oven. The size and morphology of Ag-MFS structures are dependent primarily on the deposition time as shown in Figure 5.4. Figure 5.4 (a) presents the image of Ag structures after 10 minutes of deposition shows the size of one flower-like structure which is approximately 150 nm. Figure 5.4 (b) shows the flowers like structures after 15 minutes of deposition time show the size and the size increases approximately to 500

nm. Figure 5.4 (c) shows this structure after 45 minutes of deposition time with sizes recorded approximately to 1600 nm (Bond, 2002). During the electrodeposition process, Ag atoms were deposited randomly on the ITO substrate. When the deposition time was longer, more Ag cations were reduced to become Ag nanoparticles and deposition still going on randomly. In Figure 5.4, some parts of ITO substrate were covered with separate Ag islands due to the agglomeration of Ag nanoparticles on those particular areas. This formation increased the conductivity of their adjacent, resulting in the agglomeration of electrons in the peculiar areas. As the deposition process contained freely moving Ag cations then chose to move towards the rich electron areas. At this stage, they were no longer deposited randomly on the ITO substrate. When the amount of Ag nanoparticles deposited on the Ag islands were large enough, flower-like microstructures were finally formed.

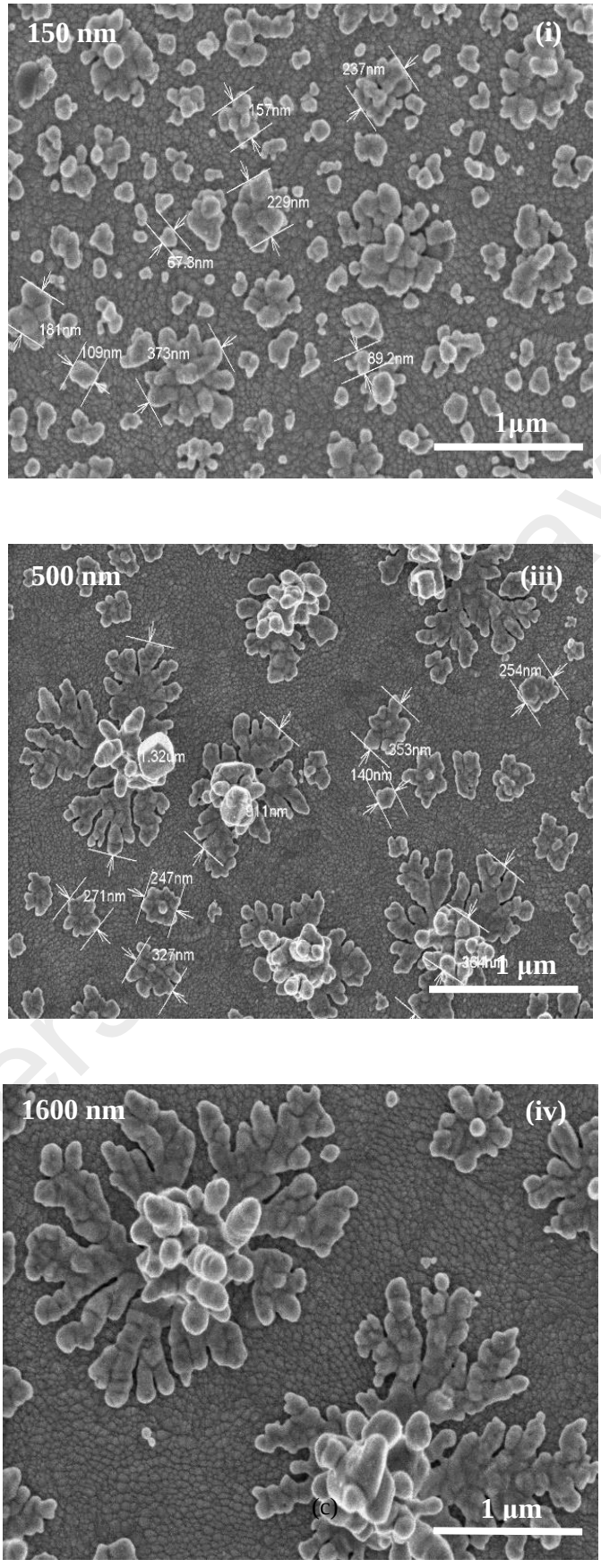

Figure 5.4: FESEM images of Ag-MFs at different time of deposition, which show as (a) has smallest cluster of ~150 nm for 10 minutes of deposition (b) with range of

~150–500 nm for 15 minutes of deposition and (c) structures with range of~300–1.3 nm for 45 minutes of deposition.

The UV–VIS spectra are shown in Figure 5.5 confirming Ag MFs LSPR films are present. The SPR peak absorption of Ag-MFs layer is dissimilar among the Samples, attributed to the absorption due to different flower size of the flowers. The absorption spectrum of the Ag MFs synthesized at 10 min is around 369 nm. When the increased the deposition time to 15 min and 45 min, the peak absorption is moved to red shift of the absorption plasmon band as stated as 372 nm and 375 nm respectively.

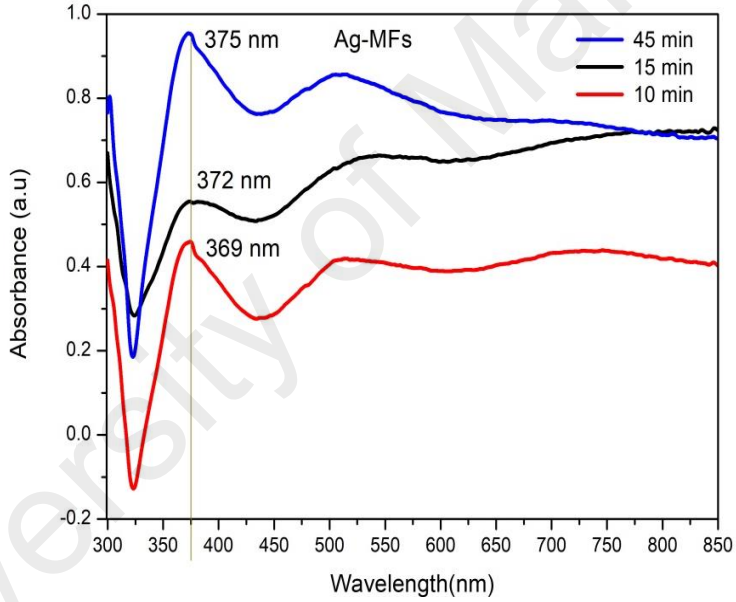

Figure 5.5: UV–VIS absorption spectra of Ag-MFs at different time of electrodeposition.

The EDX spectrum of Ag 10 minutes duration deposition show the peak at 0.7 keV and 2.98, also Ag at 15 minutes deposition duration showed the Ag peak at 0.7 keV and 2.98. The respective EDX spectrums are shown in Figure 5.6 and 5.7 respectively. Both EDX spectra showed a high peak of Ag detected from 10 minutes and 15 minute which have silver metal. The comparatively small existence of oxygen for both Samples

seen in the data may due to slight oxidation occurring on the surface of Ag Samples (Adekoya et al., 2012; Colak & Aral, 2005).

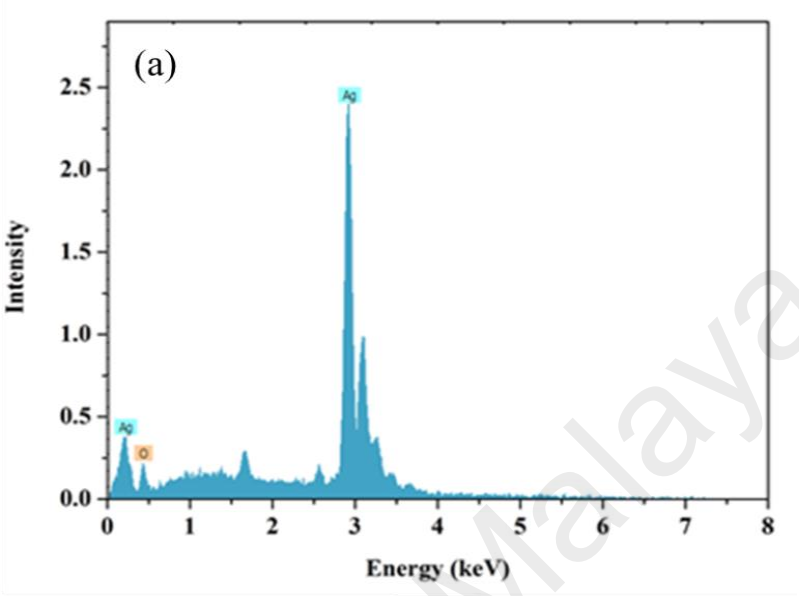

Figure 5.6: EDX spectrum analysis of Ag at 10 minutes.

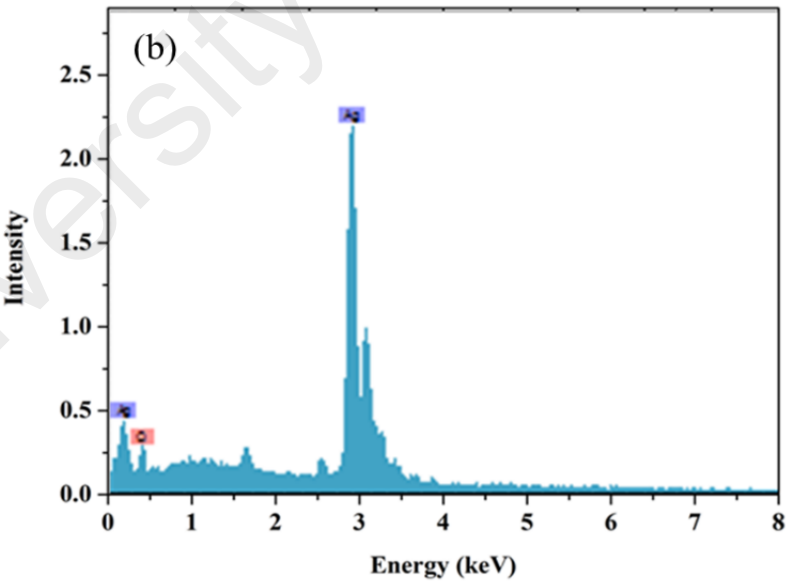

Figure 5.7: EDX spectrum analysis of Ag at 15 minutes.

5.2.3 Nitrogen doped graphene

Nitrogen doped graphene fabrication, according to the modified Hummers method, was employed with Graphite powder (1–2 mm, Aldrich) used as the precursor for the graphene oxide (GO) synthesis, 50 mL of a GO suspension in ethanol was (1 mg/mL) added with a 100 mg of urea. The dispersion was heated to 80 °C and stirred it until it dried. The powders was then placed in an Al_2O_3 crucible in a tube furnace and flushed with a 100 mg of Ar gas to remove the oxygen. Thereafter, the temperature was increased to 600 °C at 3 °C min^{-1} for an hour; for being increase again to 900 °C at 5 °C min^{-1} for 4 hours. Finally, it was cooled to room temperature to collect the as-synthesized N-graphene. The use of N-doped can increase attention which N-doped graphene which significantly enhance properties in physics materials sciences...etc. The FESEM show the morphology and structure of the as-synthesized pure N-graphene in Figure 5.8 indicate that the structure of composites image of N-graphene reveals crumpled sheet-like layer morphology with diameters of several micro-meters. The crumpling could be attributed to the defective structures formed by the exfoliation or the introduction of doped nitrogen atoms. Figure 5.9 shows the UV–visible spectra of Nitrogen doped graphene, where peak absorption was observed at 325 nm and 425 nm.

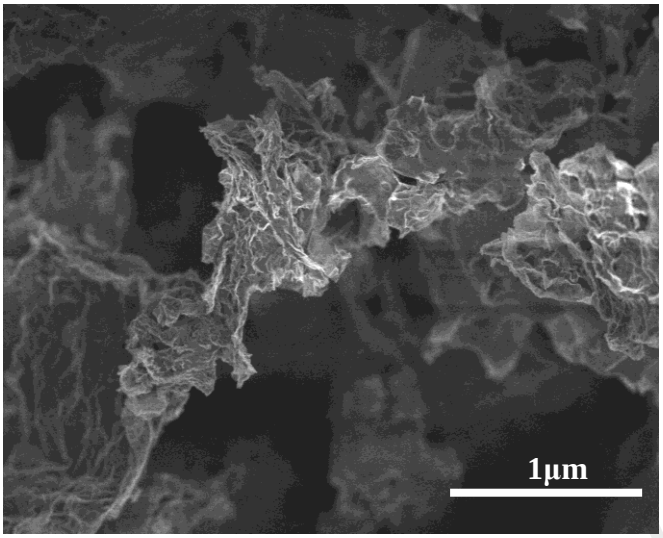

Figure 5.8: FESEM image of nitrogen doped graphene.

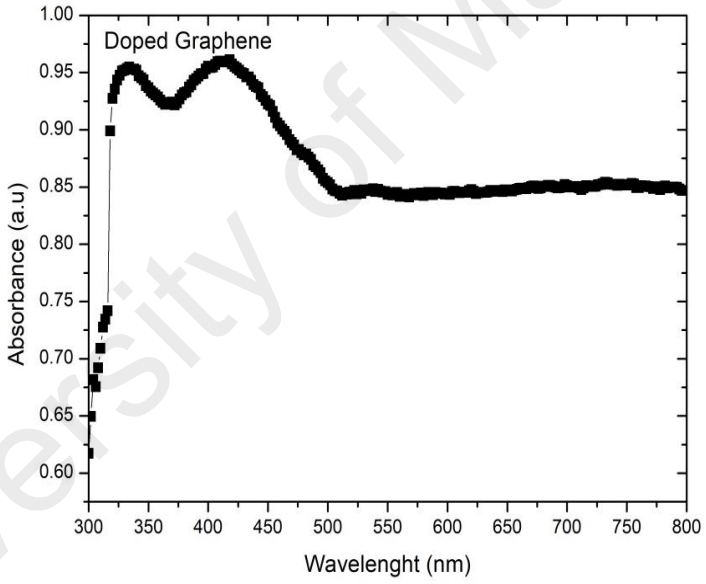

Figure 5.9: UV-Vis spectra of Nitrogen doped graphene.

5.2.4 Preparation of Graphene Oxide

There are a number of chemical oxidation methods to produce GO solution such as Hummers method (Ming, 2010) (Hummers Jr & Offeman, 1958), Staudeumaier's method (Staudenmaier, 1898), and Brodie's method (Brodie, 1859). GO solution used in this presented work was produced by the modified Hummer's method (Marcano et al., 2010). The synthesis process is explained as follows:

1. Graphite flake was first oxidized to a high degree of oxidation by mixing Potassium Permanganate ($KMnO_4$) and concentrated acid such as sulfuric acid with the flakes.
2. The mixture was constantly stirred under room temperature for 3 days. During this period, the color of the mixture changed from dark purplish green to dark brown.
3. To end the oxidation process, Hydrogen Peroxide (H_2O_2) solution was added, and the color of the mixture changed to bright yellow, indicating high oxidation level of graphite.
4. The graphite oxide was then washed several times with Hydrochloric Acid (HCl) and deionized (DI) water until a pH of 4-5 was achieved. The washing process was carried out using simple decantation of supernatant via a centrifugation technique with a centrifugation force of 10,000 g (G-force). During this process, the graphite oxide was exfoliated to formed GO gel. Finally, this gel was diluted using DI water into a suitable concentration for solution drop-casting.

5.2.5 Graphene Oxide coating

Two drops of 2.4 μL of GO solutions are applied directly onto the microscope glass via the drop-casting technique using a micropipette. The sample was then allowed to dry under ambient conditions with the drying process monitored using an optical microscope. To achieve thicker GO coating with the same coating area, multiple-drop-casting of small volume solution droplets onto the same area is applied.

The FESEM image in Figure 5.10 shows the morphology and structure of the synthesized Graphene oxide which reveals crumpled sheet-like layer morphology with diameters of several micro-meters.

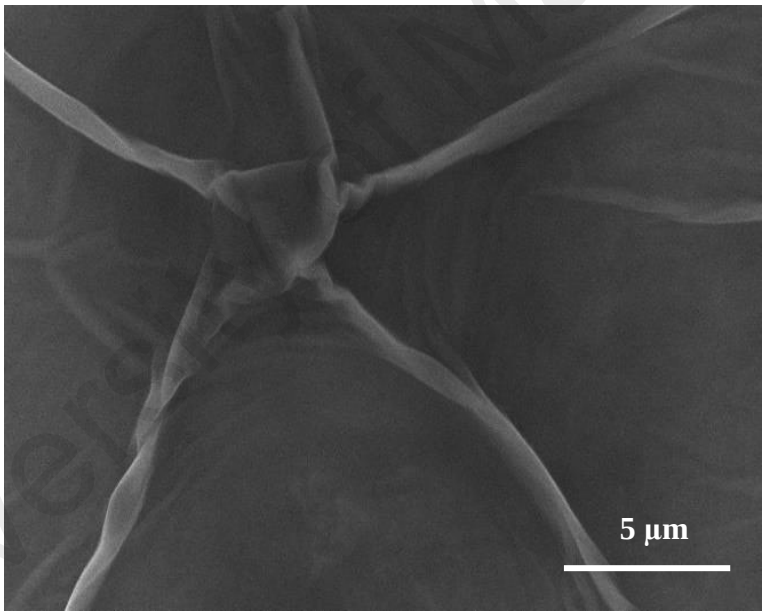

Figure 5.10: FESEM image of Graphene Oxide.

Figure 5.11 shows the UV–VIS spectra of the GO. The different absorption peaks appear due to different number of drop of GO; 2 drops (2.4μL) of GO occur at 293 nm while 3 drops (2.4μL) occur at 295 nm, respectively.

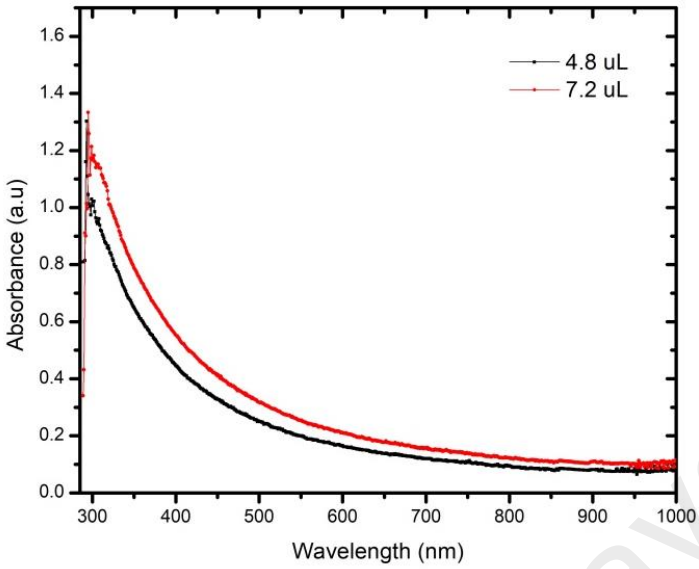

Figure 5.11: Absorption spectrum of graphene oxide.

Figure 5.12 shows the X-ray diffraction (XRD) of GO with sharp peak range around ~7- 12° and broad peak range around ~13- 25°. The data were collected using a PAN-analytical model EMPYREAN diffraction meter, equipped with a copper rotating anode (Cu Kα) radiation and a scintillation detector. All data were collected using reflection mode geometry.

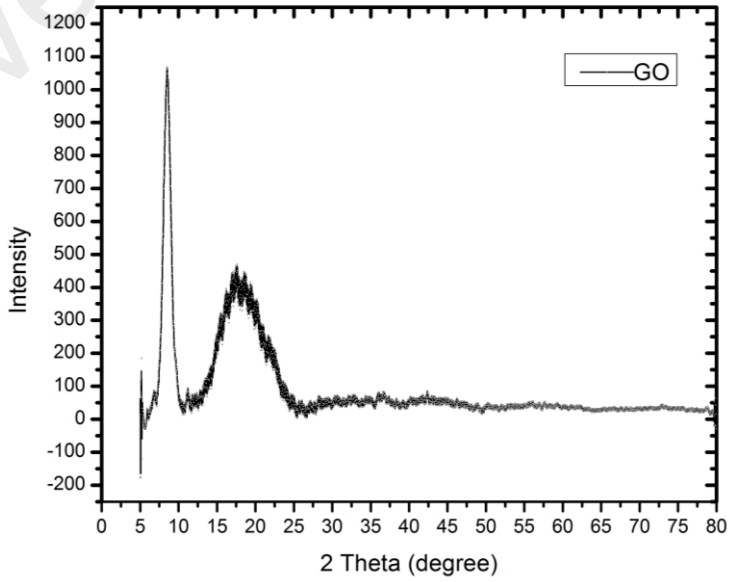

Figure 5.12: X-Ray-Diffraction of Graphene Oxide.

Table 5.1: Process parameters for plasmonics structures of materials.

Deposition material	Deposition method	Thin film thickness (nm)	Annealing temperature (^{o}C)	Annealing duration
Platinum	Electrophoretic Deposition Technique	55 nm	170	3 hours
Silver	Electrophoretic Deposition Technique	150	50	30 minutes
Silver	Electrophoretic Deposition Technique	500	50	30 minutes
Silver	Electrophoretic Deposition Technique	1600	50	30 minutes
N_2	Drop casting	375	40	10 minutes
GO (4.8 µL)	Drop casting	172	NA	NA
GO (7.2 µL)	Drop casting	194	NA	NA

5.3 Nonlinear absorption and nonlinear refraction

The nonlinear refraction and nonlinear absorption index shown in Figure 5.13 is dependent on the incident intensity of the laser. For the closed-aperture setup we used linear transmittance of S = 0.35 at the close aperture. The Z-scan measurement was also performed at different average powers Pt-NSs for 67 with decrease of the intensity shown to increase in the nonlinear absorption when the laser light increasing as shown in Figure 5.13(a).

In the open-aperture Z-scan setup in Figure 5.13 (a) the measured transmittance of the Pt-NPs will be reduced as the sample is translated through the laser focal point and can be seen that the open aperture transmittance is symmetric in relation to the focal point Z = 0. From the Equation 4.3 shows intensity (I_0) has the proportional relationship between β and $\Delta T(z)$.

The magnitude change in the nonlinear absorption coefficient $\Delta T(z)$ occurs varies only slightly differences in the incident laser intensity (Henari, 2001). Table 5.2 show

values of β and n_2 of Pt-NPs layers. 10 mW shows lower β of 2.74×10^{-3} cmW^{-1} while at 30 mW, 40 mW and 70 mW show decreasing value of β as 1.05×10^{-3} cmW^{-1}, 8.5×10^{-4} cmW^{-1} and 4.7×10^{-4} cmW^{-1}, respectively due to increasing the power.

The intensity decreases as the laser light increases as shown in Figure 5.13(b) due to nonlinear refection From the Equation (4.6) intensity (I_0) is proportional to n_2 and ΔT_{P-V}. The intensity of the light is obtained from the calculated peak power over the cross-sectional area of the laser beam. The NLA coefficient (β) can then be determined by measuring the peak-valley value, $\Delta T_{(z)}$ of the transmittance profile.

Increment laser power from 10 mW to 70 mW will decrease the nonlinear refraction (n_2) from -4.21×10^{-8} cm^2W^{-1} to -1.35×10^{-8} cm^2W^{-1}, due to the contribution of thermal nonlinear optical effect (Ara et al., 2012). Table 5.2 show the measurement conditions and associated results regarding values of (NLA and NLR) at five input power and the laser intensity at the focus beam.

The intensity depended of the absorption is measured as a change of transmittance through the sample for closed aperture Z-scan, even though can be determined more accurately via open aperture Z-scan. The values of β and n_2 is dependent on the light-matter interaction that occurs when a laser of sufficiently high intensity is incident through the sample. This study provides evidence of the β and n_2 values of nanomaterials and micro-materials (Ara et al., 2008; Mezher et al., 2016a; Mezher et al., 2015; G. Yang, Guan, Wang, Wu, & Chen, 2004).

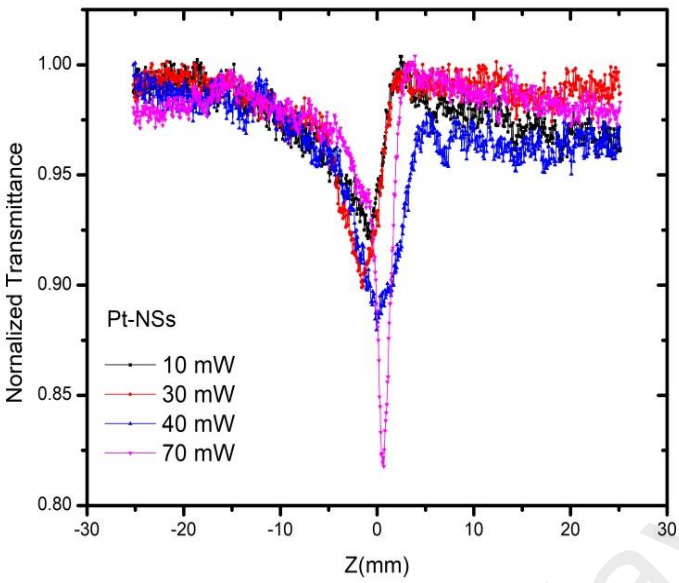

(a)

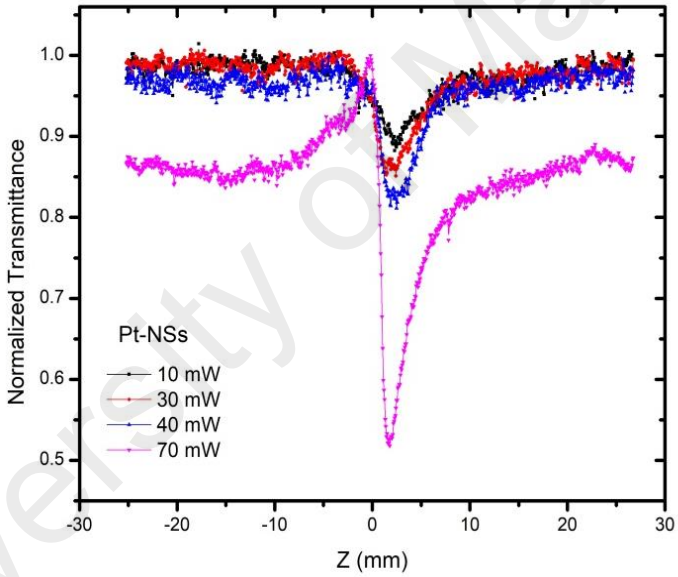

(b)

Figure 5.13: (a) Open aperture and (b) Close aperture Z-scan curve for samples platinum at different power.

Figure 5.14 (a) illustrates the open-aperture of Z-scan transmittance profile of samples of the Ag micro-flowers with thicknesses of 50 nm, 70 nm and 160 nm. The absorption level at the beginning and end of the Z-Scan is significantly different due to micro flower layers size. The nonlinear absorption coefficients of the different layers of MFs of 50 nm, 70 nm and 160 nm are determined by the indicative shift of the deep $\Delta T_{(z)}$. Their respective nonlinear absorption coefficient is shown in Table 5.2.Samples with thicknesses of 50 nm, 70 nm and 160 nm thicknesses show different trend of NLA. The NLA of thicknesses of 50 nm, 70 nm and 160 nm show of 2.28×10^{-4} cmW^{-1}, 2.30×10^{-4} cmW^{-1} and 2.33×10^{-4} cmW^{-1}, respectively.

The close-aperture Z-scans is show in Figure 5.14 (b) where transmission peaks followed by valleys near the focal point, which is unsymmetrical in trend. The 50 nm, 70 nm and 160 nm MFs films reveal post focal peak and valley, which is a clear indication of negative lens of n_2 (Mezher et al., 2016b; Mezher et al., 2015). The 50 nm shows lower refractive index of n_2 as -2.11 $x10^{-9}$ cm^2W^{-1} due to the value of peak and valley transmittances (T_p-T_v). A 70 nm thickness show increasing refractive index of n_2 as -2.22 $x10^{-9}cm^2W^{-1}$ and 160 nm thickness showing increasing value of n_2 as -3.71 $x10^{-9}cm^2W^{-1}$ due to the increasing in the micro-flower size of the thin film and formation of hot spots of these flowers. The different size of nanoparticles confirms nonlinear properties can be enhanced when increasing size of nanoparticles due to (T_p-T_v) (Henari, 2001; Singh & Aghamkar, 2014; Zakaria, Mezher, & Chong, 2016b).

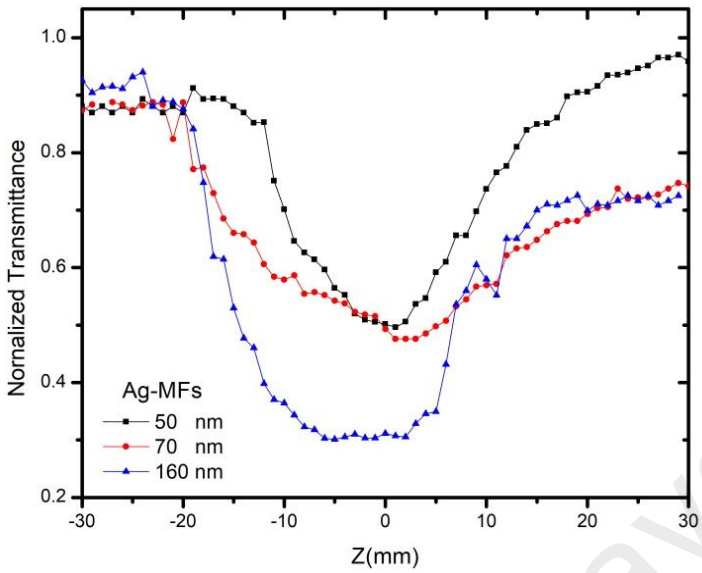

(a)

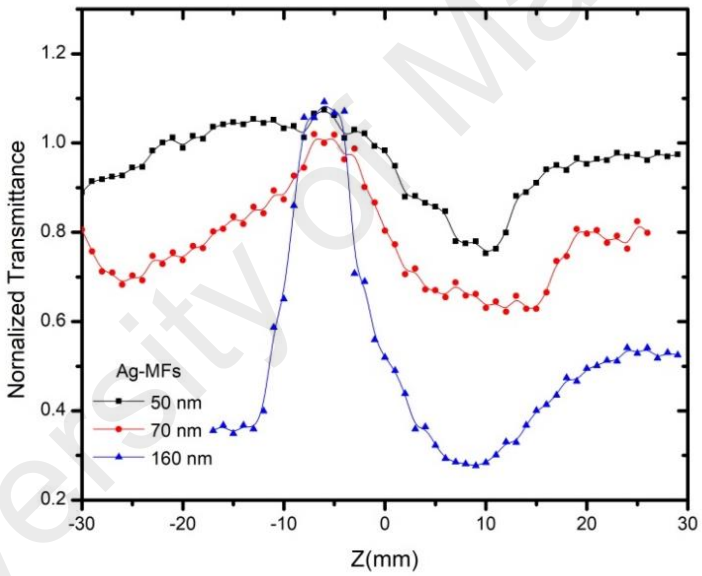

(b)

Figure 5.14: (a) Open aperture and (b) close aperture of 50 nm, 70 nm and 160 nm data points with fitting lines for samples with different times of exposure.

The open-aperture transmission of the nitrogen doped graphene is measured in the far-field to obtain the respective nonlinear absorption coefficients. Figure 5.15 (a) shows the transmission spectra of the sample at different incident laser power. The transmission increases with the increase in intensity towards the focal point, which is an indication of saturable absorption exhibited by the nitrogen doped graphene (F. Zhang et al., 2016). Near the focal point, the transmission shows a sharp decrease, indicating the occurrence of nonlinear absorption. All samples show transmission "valley" around the focal point which is asymmetrical. For 30 mW of laser incident power, the sample shows a NLA value of 3.11×10^{-4} cmW^{-1}. When the incident power is increased to 90 mW, the NLA value reduced to 2.17×10^{-4} cmW^{-1}.

The closed-aperture measurement was performed and normalized transmittance was recorded as shown in Figure 5.15 (b). The nitrogen doped graphene exhibited post focal peak and valley, directly indicating negative n_2 (negative lens). The Z-scan measurement was also performed close aperture at different power from 30 mW to 90 mW which indicates the different nonlinear refraction of nitrogen doped graphene. The 30mW sample shows NLR as -9.77×10^{-9} $cm^2\ W^{-1}$ and 90mW shows the NLR as -3.42×10^{-9} $cm^2\ W^{-1}$. The change in NLA and NLR with incident laser power is believed to be due to the contribution of thermal nonlinear optical effect.

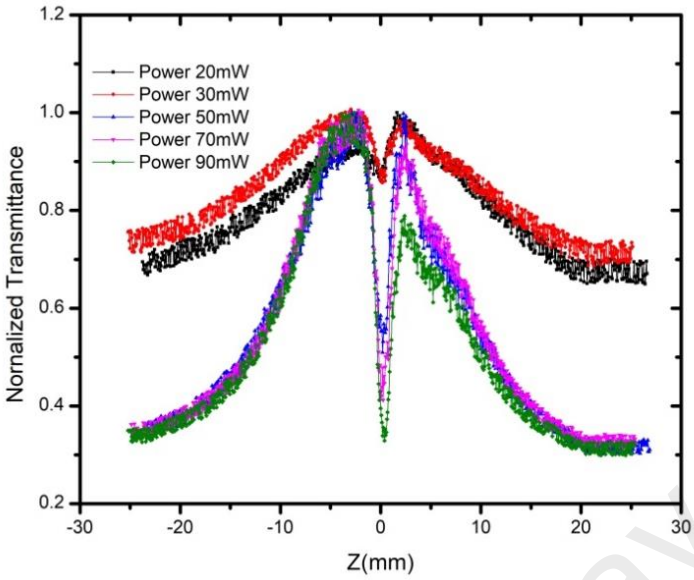

(a)

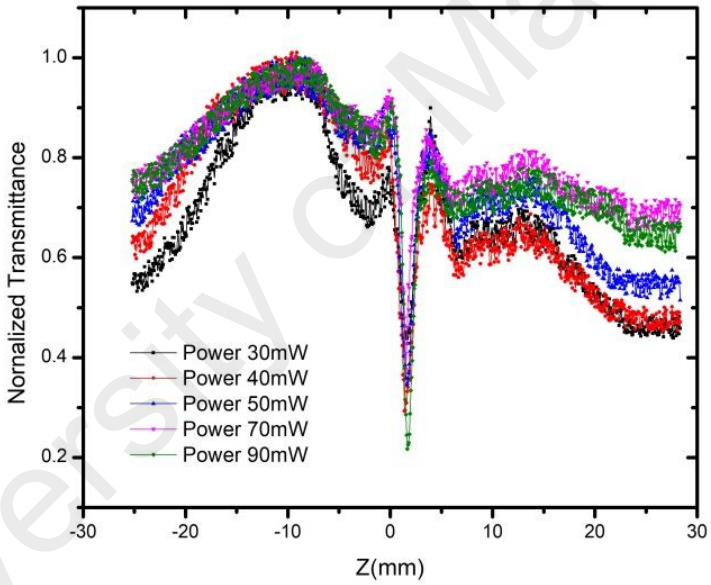

(b)

Figure 5.15: (a) Open aperture and (b) Close aperture Z-scan curve for nitrogen doped graphene.

The open-aperture transmission of the GO is shows in Figure 5.16 (a) where the measurement in the far-field is done to obtain the respective nonlinear absorption coefficients. The nonlinear absorption of GO films thickness as ~ 0.17 μm is 2.0×10^{-4} cmW^{-1} while GO with thickness of ~ 0.22 μm showing nonlinear absorption 2.2×10^{-4} cmW^{-1}.

To evaluate the refractive nonlinearity, the focus was on the magnitude of nonlinear refractive index, n_2. For this reason, the closed-aperture measurement was performed and normalized transmittance was recorded as shown in Figure 5.16 (b) of GO films exhibited post focal peak and valley, directly indicating negative n_2 (negative lens).

The Z-scan measurement was also performed at different thickness, GO films with thickness of ~ 0.17μm shows $n_2 = -2.69 \times 10^{-9}$ cm^2W^{-1} while GO with thickness ~ 0.22 μm show $n_2 = -3.26 \times 10^{-9}$ cm^2W^{-1}. Table 5.2 tabulates the measurement condition and associates the values of nonlinear absorption and nonlinear refraction,

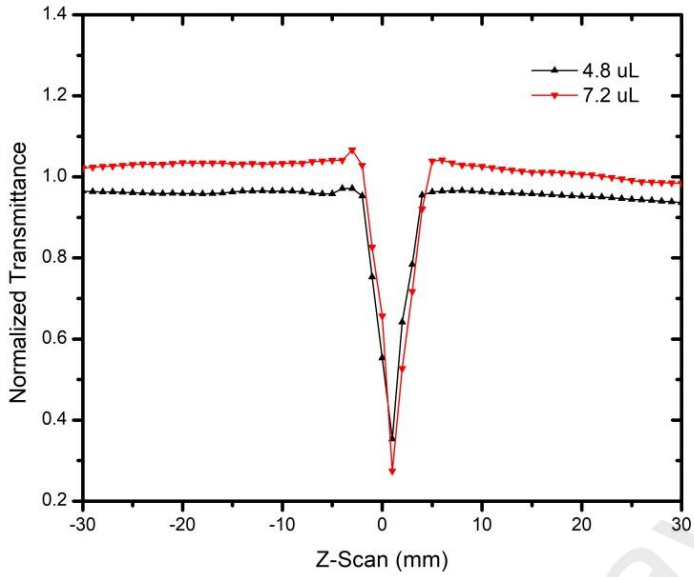

(a)

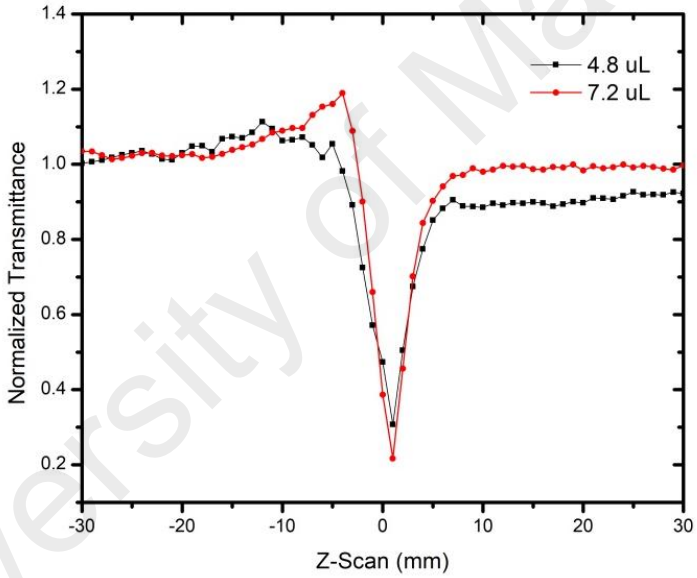

(b)

Figure 5.16: (a) Open aperture and (b) closed aperture from Z-scan curve for graphene oxides.

Table 5.2: Nonlinear Refractive Index and Nonlinear Absorption for different structures.

Sample	PI(mW)	λ(nm)	w_o(μm)	I_0(MWcm^{-2})	α (cm^{-1})	$\Delta\Phi_0$	n_2(cm^{2}W^{-1})	β(cmW^{-1})
PT	10	800	15.28	49.87	50 x10^4	0.30	-4.21x10^{-8}	2.74x10^{-3}
	30	800	15.28	149.35	49 x10^4	0.39	-1.77x10^{-8}	1.05x10^{-3}
	40	800	15.28	199.14	45 x10^4	0.47	-1.51x10^{-8}	8.5x10^{-4}
	70	800	15.28	348.50	21 x10^4	1.20	-1.35x10^{-8}	4.7x10^{-4}
Ag-MFs	33	800	11.9	110.12	4.34 x10^4	0.86	-2.11 x10^{-9}	2.28x10^{-4}
Ag-MFs	33	800	11.9	110.12	5.58 x10^4	1.16	-2.22 x10^{-9}	2.30x10^{-4}
Ag-MFs	33	800	11.9	110.12	9.87 x10^4	2.37	-3.71 x10^{-9}	2.33x10^{-4}
N_2	20	800	8.28	107.62	5.54 x10^4	1.12	-9.77x10^{-9}	3.11x10^{-4}
	30	800	8.28	175.60	5.04 x10^4	1.62	-6.26x10^{-9}	2.72x10^{-4}
	50	800	8.28	294.55	4.31 x10^4	1.81	-5.13x10^{-9}	2.39x10^{-4}
	70	800	8.28	464.49	4.28 x10^4	2.02	-3.59x10^{-9}	2.30x10^{-4}
	90	800	8.28	526.80	4.13 x10^4	2.20	-3.42x10^{-9}	2.17x10^{-4}
GO 4,2μL	30	750	4.2	650.82	1.8 x10^4	2.14	-2.696x10^{-9}	2.02x10^{-4}
GO 7.2μL	30	750	4.2	650.82	2.4 x10^4	2.67	-3.26x10^{-9}	2.29x10^{-4}

CHAPTER 6: APPLICATIONS IN OPTICAL SENSING

6.1 Optical waveguide sensors

Sensor devices have been used in many applications to monitor environmental factors such as temperature, stress, humidity, and the presence or concentration of a chemical or biological species (Barker et al., 1998; Chan et al., 1984; Dietrich et al., 1996; El-Sherif et al., 2007; Ferguson et al., 1996; Healey et al., 1997; Holst & Mizaikoff, 2001; Mizaikoff et al., 1995; Nguyen, 2012; Schweizer et al., 1997; Stewart et al., 1997; Wolfbeis, 2004).

Optical waveguide sensor is a device that detects environmental changes using light as the signal carrier. It utilises changes in light parameters such as intensity, phase, polarization and resonance wavelength due to changes in environmental factors as the general sensing principle. The change different parameters can cause by changes in the refractive index, absorption coefficient, fluorescence characteristics and Surface Plasmon Resonance of the optical material used.

The main advantages of optical waveguide sensors are immunity to electromagnetic noise, lightweight, relative robustness and durability, high sensitivity, low cost, ability for distributed sensing and the fact that they can be tailored in many ways to suit specific applications.

In this chapter, the use of metal nanoparticle layers and graphene oxide coating as sensing elements will be studied and discussed. Particularly, focus will be given on the sensing of water content in insulating oil in electric transformers.

6.2 Electric power transformer

An electric power transformer is a vital component in the network used to distribute electricity over long distances. Transformer have evolved over the past 20 years from a necessary item of expenditure to a strategic tool in the management of electrical

transmission and distribution networks. The electric power transformer consists of many part such as core, core windings, wings, primary coil, secondary coil, cellulose papers and insulation oil. To ensure efficient operation, the health of a transformer is always being monitored for oil leaks and hot spots. Another critical component of a transformer is the condition of the insulating oil. Pristine oil should contain no dissolved gas or water content. However, in many instances, water moisture and gas are introduced into the insulating oil after prolonged operation.

The water content in insulation oil is the focus of our sensing application. Insulation oil in an electrical power transformer is commonly known as transformer oil. This insulation oil normally obtained by fractional distillation and subsequent treatment of crude petroleum. That is why this oil is also known as mineral insulating oil.

Transformer oil mainly serves two purposes: (1) it acts as the liquid insulation in electrical power transformer and (2) it dissipates heat generated by the operation of the transformer. acts as coolant. In addition, transformer oil helps to preserve the core and winding as well as the cellulose paper inside the windings from oxidation as these parts are fully immersed inside the transformer oil.

However, the transformer oil itself is also prone to oxidation. Generally there are two types of transformer oil commonly used namely, paraffin-based transformer oil and Naphtha based transformer oil.

The main difference between the two oils is their oxidation rate and their chemical products. Naphtha oil is more easily oxidized than Paraffin oil. But oxidation products (sludge) of naphtha oil based are more soluble compared to the oxidation product of Paraffin oil. Thus sludge of naphtha based oil does not precipitate at the bottom of the transformer and does not obstruct the convection circulation of the oil, which is a

critical process of the transformer cooling system. In the case of Paraffin oil, although the oxidation rate is lower than that of Naphtha oil, the oxidation product (sludge) is insoluble and will precipitate at the bottom of the transformer, thus reducing the efficiency of the transformer cooling system. Another problem with paraffin based oil is its high pour point due to the higher wax content. This, however, does not affect its use in warm climate condition such as Malaysia and Iraq. Although Paraffin based oil has the above mentioned disadvantage, it is still generally used due to its cost and availability.

The properties of transformer oil should be routinely checked to determine the serviceability of the oil. The parameters of transformer oil can be categorized as follow,

1. Electrical parameters: Dielectric strength, specific resistance, dielectric dissipation factor.
2. Chemical parameter: Water content, acidity, sludge content.
3. Physical parameters: Inter facial tension, viscosity, flash point, pour point.

6.3 Water content in transformer oil

The operation condition of a transformer is very sensitive to the relative water content in the transformer oil. The solubility of water in transformer oil is dependent on temperature. When the temperature increases, the amount of water that can be dissolved in oil also increases. In potential manner the solubility of water in mineral oil, S_o with temperature is given by:

$$Log(S_o) = \frac{-1567}{k} + 7.0895 \quad (6.1)$$

where K is the temperature in Kelvin ($^oC + 273$)

The actual amount of water measured in the oil in relation to the solubility level at that temperature is termed Relative Saturation (R_S). *RS*, expressed in percentage, is the

concentration of water (W_c) in the oil relative to the solubility (S_o) of water the oil can hold at a specific temperature, as shown in Equation (6.2):

$$RS = W_c / S_o \ (100\%) \tag{6.2}$$

where W_c and S_o both have units in wt. ppm.

Depending on its content, water can appear in three different forms in oil (Lewand, 2002b):

(i) Dissolved water, where the water molecules are hydrogen bonded to the hydrocarbon molecules of the transformer oil.

(ii) Emulsion, which is a supersaturated solution of water and oil usually having a milky appearance.

(iii) Free water, which is also a type of supersaturated solution of water and oil, where the concentration of water is high enough to form water droplets separate from the oil.

There two sources of moisture contamination in transformer oil, namely bush leaks and water out-diffusion from cellulose paper. A bush leak occurs when the seals on the transformer degraded and allows the internal sections of the transformer to be exposed to external elements. Most transformers use cellulose-based paper as insulation in the windings. Water content is introduced into the transformer oil when it is subjected to overloading, which results in the increase of temperature of the transformer oil. The solubility of water in the oil increases with temperature, resulting in the cellulose paper releasing its water content into the transformer oil. As the transformer cools down, the water will stay in the transformer oil, taking on the forms discussed above.

One of the most important functions of transformer oil is to provide electrical insulation, a property which is dependent on the dielectric prop of the oil. Water content

in transformer oil is highly undesirable as it will adversely affect the dielectric properties of the oil. Any increase in water content can reduce the insulating properties of the oil, which may result in dielectric breakdown.

The water content in oil is measured as ppm (parts per million units). Transformers with different voltage rating (Type O, A, B and C), each have different tolerance to water content, ranging from 5 to 25 ppm by weight. Exceeding this limit may cause malfunction of the transformer, or in more severe cases, a burst and fire. Even though the risk of failure of a transformer is relatively small, its occurrence will inevitably lead to high repair costs, long downtime and possible safety hazards. Moreover, transformers are too expensive to replace regularly and must be properly maintained to maximize their life expectancy.

The current protocol for water content measurement in transformer oil involves shutting down the transformer and then taking oil samples out from the transformer and to for laboratory analysis using the Karl Fisher Titrator technique. The current technique involves shutting down and then powering up the transformer again for oil sample extraction. This practice may itself cause temperature fluctuation in the transformer and may in the process introduce additional water content into transformer oil. It is therefore desirable to be able to monitor the water content of an operating transformer without the need to interrupt its operation. One of the possible solutions is to use optical remote sensing, where the sensors probe can be placed in the transformer for continuous remote monitoring of the transformer oil condition. This is possible as optical sensing uses light as the signal carrier instead of electricity, which eliminates the possibility of oil ignition due to short circuit. There are a few more advantages for using optical sensing compared to electrical-based sensor, which will be discussed in the following sections. In addition,

the use of metal nanoparticle and graphene oxide coated optical waveguides as water content sensors in transformer oil are also discussed.

6.4 Karl fisher titration method

Before the sensing performance of the proposed sensors can be studied, it is essential to establish the accurate water content in the transformer oil samples to be used in the study. For this purpose, measurement of water content in transformer oil samples is first carried out using an established method. The water content in the transformer oil samples is measured by TOLS Oil Lab and Services Sdn Bhd using the Karl Fischer titration weight injection International Electrotechnical Commission 60814 (IEC 60814) method. An example of the test results is shown in Figure 6.1 below. 4 transformer oil samples with water content ranging from 15 ppm to 21 ppm are prepared.

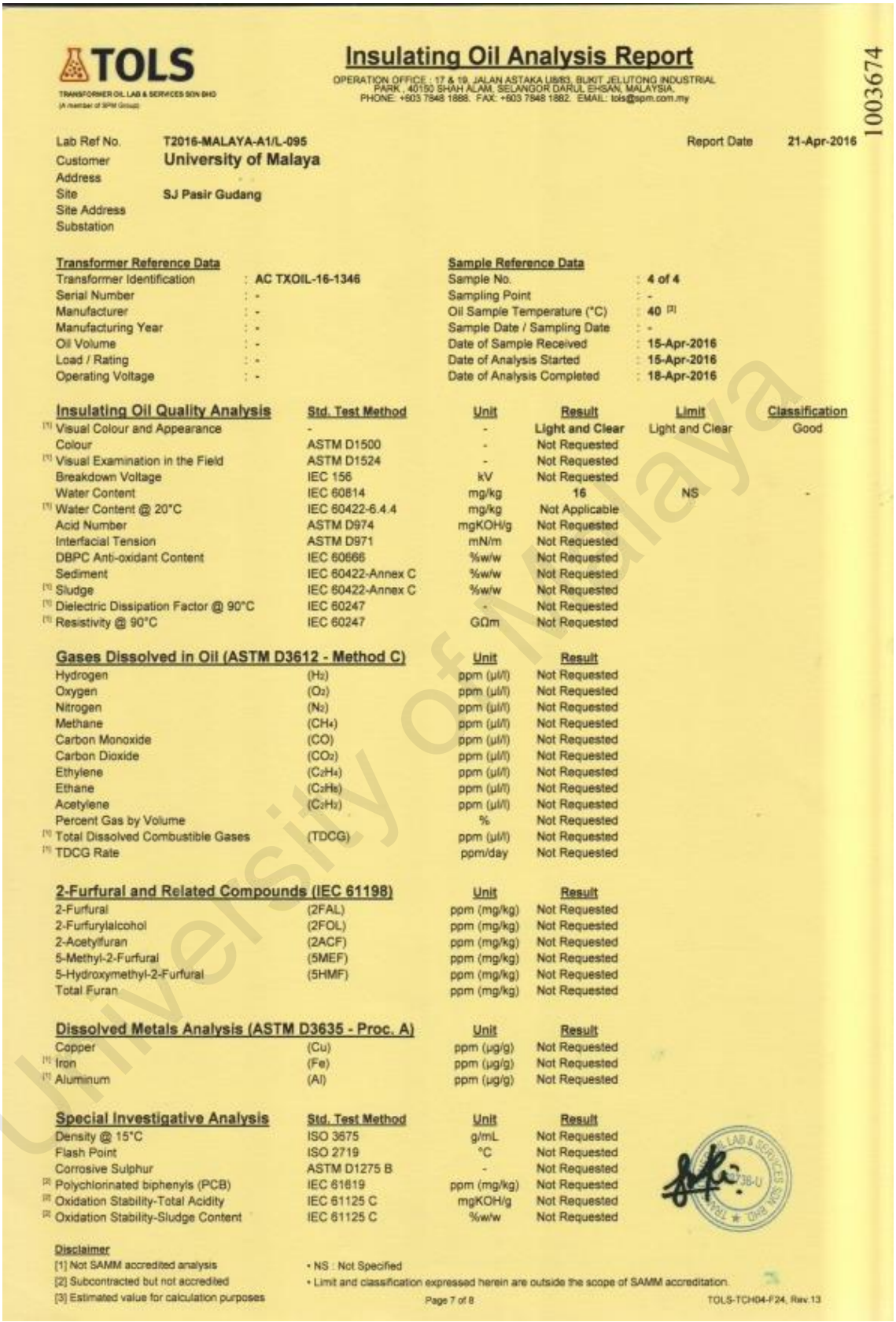

TOLS
TRANSFORMER OIL LAB & SERVICES SDN BHD
(A member of SPM Group)

Insulating Oil Analysis Report

OPERATION OFFICE : 17 & 19, JALAN ASTAKA U8/83, BUKIT JELUTONG INDUSTRIAL PARK, 40150 SHAH ALAM, SELANGOR DARUL EHSAN, MALAYSIA.
PHONE: +603 7848 1888. FAX: +603 7848 1882. EMAIL: tols@spm.com.my

1003674

Lab Ref No. T2016-MALAYA-A1/L-095
Customer University of Malaya
Address
Site SJ Pasir Gudang
Site Address
Substation

Report Date 21-Apr-2016

Transformer Reference Data

Transformer Identification	AC TXOIL-16-1346
Serial Number	-
Manufacturer	-
Manufacturing Year	-
Oil Volume	-
Load / Rating	-
Operating Voltage	-

Sample Reference Data

Sample No.	4 of 4
Sampling Point	-
Oil Sample Temperature (°C)	40 [3]
Sample Date / Sampling Date	-
Date of Sample Received	15-Apr-2016
Date of Analysis Started	15-Apr-2016
Date of Analysis Completed	18-Apr-2016

Insulating Oil Quality Analysis	Std. Test Method	Unit	Result	Limit	Classification
[1] Visual Colour and Appearance	-	-	Light and Clear	Light and Clear	Good
Colour	ASTM D1500	-	Not Requested		
[1] Visual Examination in the Field	ASTM D1524	-	Not Requested		
Breakdown Voltage	IEC 156	kV	Not Requested		
Water Content	IEC 60814	mg/kg	16	NS	-
[1] Water Content @ 20°C	IEC 60422-6.4.4	mg/kg	Not Applicable		
Acid Number	ASTM D974	mgKOH/g	Not Requested		
Interfacial Tension	ASTM D971	mN/m	Not Requested		
DBPC Anti-oxidant Content	IEC 60666	%w/w	Not Requested		
Sediment	IEC 60422-Annex C	%w/w	Not Requested		
[1] Sludge	IEC 60422-Annex C	%w/w	Not Requested		
[1] Dielectric Dissipation Factor @ 90°C	IEC 60247	-	Not Requested		
[1] Resistivity @ 90°C	IEC 60247	GΩm	Not Requested		

Gases Dissolved in Oil (ASTM D3612 - Method C)		Unit	Result
Hydrogen	(H_2)	ppm (µl/l)	Not Requested
Oxygen	(O_2)	ppm (µl/l)	Not Requested
Nitrogen	(N_2)	ppm (µl/l)	Not Requested
Methane	(CH_4)	ppm (µl/l)	Not Requested
Carbon Monoxide	(CO)	ppm (µl/l)	Not Requested
Carbon Dioxide	(CO_2)	ppm (µl/l)	Not Requested
Ethylene	(C_2H_4)	ppm (µl/l)	Not Requested
Ethane	(C_2H_6)	ppm (µl/l)	Not Requested
Acetylene	(C_2H_2)	ppm (µl/l)	Not Requested
Percent Gas by Volume		%	Not Requested
[1] Total Dissolved Combustible Gases	(TDCG)	ppm (µl/l)	Not Requested
[1] TDCG Rate		ppm/day	Not Requested

2-Furfural and Related Compounds (IEC 61198)		Unit	Result
2-Furfural	(2FAL)	ppm (mg/kg)	Not Requested
2-Furfurylalcohol	(2FOL)	ppm (mg/kg)	Not Requested
2-Acetylfuran	(2ACF)	ppm (mg/kg)	Not Requested
5-Methyl-2-Furfural	(5MEF)	ppm (mg/kg)	Not Requested
5-Hydroxymethyl-2-Furfural	(5HMF)	ppm (mg/kg)	Not Requested
Total Furan		ppm (mg/kg)	Not Requested

Dissolved Metals Analysis (ASTM D3635 - Proc. A)		Unit	Result
Copper	(Cu)	ppm (µg/g)	Not Requested
[1] Iron	(Fe)	ppm (µg/g)	Not Requested
[1] Aluminum	(Al)	ppm (µg/g)	Not Requested

Special Investigative Analysis	Std. Test Method	Unit	Result
Density @ 15°C	ISO 3675	g/mL	Not Requested
Flash Point	ISO 2719	°C	Not Requested
Corrosive Sulphur	ASTM D1275 B	-	Not Requested
[2] Polychlorinated biphenyls (PCB)	IEC 61619	ppm (mg/kg)	Not Requested
[2] Oxidation Stability-Total Acidity	IEC 61125 C	mgKOH/g	Not Requested
[2] Oxidation Stability-Sludge Content	IEC 61125 C	%w/w	Not Requested

Disclaimer
[1] Not SAMM accredited analysis
[2] Subcontracted but not accredited
[3] Estimated value for calculation purposes
• NS : Not Specified
• Limit and classification expressed herein are outside the scope of SAMM accreditation.

Page 7 of 8
TOLS-TCH04-F24, Rev.13

Figure 6.1 : Test results of water content in the transformer oil done by TOOLS Oil Lab and Services. Sdn. Bhd.

6.5 Water content and dielectric constant

Effects of Relative Saturation on Dielectric Strength

Water content can affect the dielectric strength of the transformer oil significantly. Dielectric strength can be sub-divided into the parameters below:

- *Breakdown Voltage*.
- *Dielectric Dissipation Factor*.
- *Relative Permittivity or Refractive Index*.
- *Resistivity*.
- *Viscosity*.
- *Color Scale*.

The parameters of interest for the current study are the breakdown voltage and relative permittivity.

6.5.1 Breakdown voltage of transformer oil

Breakdown voltages depend on the water content in the transformer oil. The breakdown voltages shown clearly in Figure 6.2 indicates that under dry condition (low than 20 wt. ppm) the breakdown voltage is as high as about 36 kV. When the water content increases to more than 50 wt. ppm, the break down voltage decreases to 13 kV (Suwarno). According to the International Electrotechnical Commission standard (IEC 60156) method for the determination of the electric strength of insulting oils, the minimum breakdown voltage of transformer oil for normal operation of transformer at room temperature must be more than 30 kV. This corresponds to a water content of less than 24 wt. ppm.

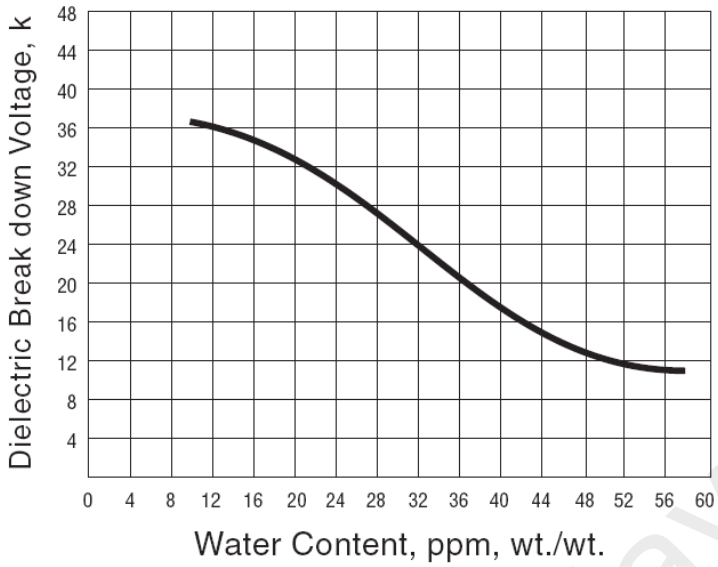

Figure 6.2: Relationship between dielectric break down voltage and water content (Suwarno).

6.5.2 Relative permittivity (refractive index) of transformer oil

Relative permittivity, also commonly known as dielectric constant, is often treated as a complex function:

$$\varepsilon_r = \varepsilon_r' - j\varepsilon_r'' \tag{6.3}$$

where ε_r' is the real part of the permittivity, which is related to the stored energy within the medium, while ε_r'' is the imaginary part of the permittivity, which is related to the dissipation (or loss) of energy within the medium (Cheng, 2011).

ε_r' of the transformer oil is influenced by its water content as reported by Constantine T. Dervos et al. (Dervos, Paraskevas, Skafidas, & Vassiliou, 2005). In their report, ε_r' of the mineral oil measured at 1 MHz changes from 2.16 to 2.21 when the water content in the mineral oil increases from 13 ppm to 17 ppm.

While the study of the effect of water content in transformer oil on its relative permittivity was undertaken at low frequency, it is believed that the optical properties of

transformer oil also changes with its water content as the refractive index of a medium, *n* is related to its relative permittivity, ε_r, and permeability, μ_r by the relation:

$$n = \sqrt{\varepsilon_r \mu_r} \tag{6.4}$$

At the optical frequency, μ_r is equal to 1, and therefore the refractive index of a medium is equal to the square root of its relative permittivity. Mahanta et al. demonstrated the detection of water content in transformer oil using a polymer optical fiber sensor. It was reported that when water content changes from 20 ppm to 65 ppm, the transmitted power of the fiber sensor, measured in voltage, decreases from 88 mV to 57 mV (Mahanta & Laskar, 2017). Further demonstrations of the measurement of water content in transformer oil using optical sensors are reported by Laskar et al. (Laskar & Bordoloi, 2013) and Banerjee et al. (Banerjee et al., 2007), where both reports the change in light propagation behavior due to the change in water content in the transformer oil under test. Though the exact value of change were not reported, it is believed that water content in transformer oil has a profound effect on the refractive index of the transformer oil, thus enabling response from the optical sensors used.

6.6 Optical waveguide sensor based on evanescent field sensing

The sensing mechanism of the proposed sensor is as follow; the propagation of electromagnetic field inside an optical waveguide is not completely confined with perfectly distinct boundary. A fraction of the field, called the evanescent field will extend from the waveguide core into the cladding. The guided field (inside the core) and the evanescent field are related by a condition of continuity of the electromagnetic field at the boundary between the core and the cladding. Thus, the guided field will be influenced by any variation in the evanescent field (Langhammer, Yuan, Zorić, & Kasemo, 2006; Mahanta & Laskar, 2016).

If a portion of the waveguide cladding can be removed, thus exposing the waveguide core, then the guided field can be influenced by variations in the surrounding environment. Furthermore, functionalization of the exposed section of the waveguide core with materials such as metal nanoparticle and graphene oxide coating can further enhanced the response of the guided field to environmental variations. Studying the performance of these waveguide structures, namely silver nanoparticle coated waveguides, platinum nanoparticle coated waveguides, graphene oxide coated waveguides are discussed below.

6.6.1 Planar waveguide coated with platinum nanoparticles

The waveguide structure used in study is shown in Figure 6.3. It is a SU-8 polymer waveguide fabricated on a silicon wafer substrate with a 5 μm of silica layer produced using thermal oxidation process. The waveguide width is 5 μm. The details of substrate cleaning, SU-8 spin coating and patterning using contact photolithography to produce SU-8 channel waveguide have been discussed in Chapter 3.

The platinum thin film is then coated onto the SU-8 waveguide using sputter coater LEICA EM SCD005. The waveguide channels are ensured to be facing up during the evaporation of the metal from the source to cover all of the channels waveguide. The thickness of the metal coating is controlled by in-situ digital thickness monitor. Finally, the thin film coated waveguide undergoes thermal treatment at 160 ^{o}C for 8 hours to form Pt-NPs. Figure 6.3 illustrates platinum nanostructures (Pt-NPs) coating on the planar waveguide with 55 nm.

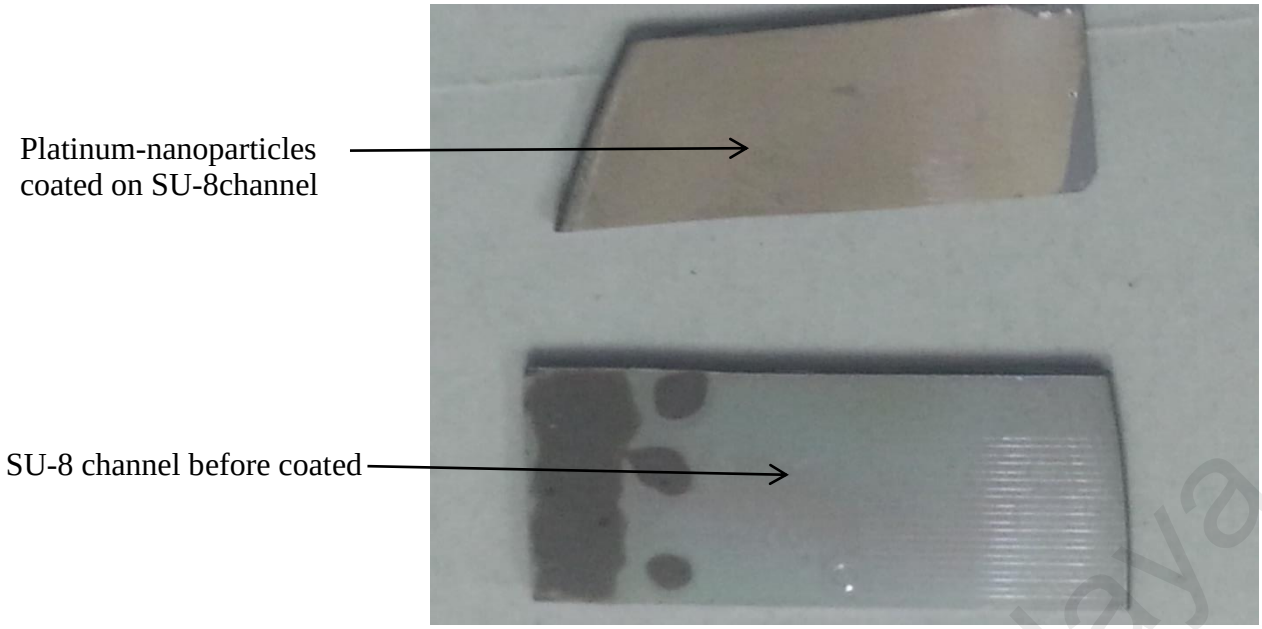

Figure 6.3: Planar waveguide coated by platinum nanoparticle.

Characterisation of the Pt-NPs coated waveguide is carried out using the setup as shown in Figure 6.4. The setup consists of two 5-axis fiber alignment stages (Newport 562 series) and a waveguide holder. The Pt-NPs coated waveguide is fixed onto the waveguide holder. The input fiber is aligned to overlap with the input end of the waveguide core. This is followed by the alignment of the output fiber to the output end of the waveguide core. A microscope equipped with CCD camera is placed on top of the alignment setup to monitor the alignments between the optical fiber and the planar waveguide. The input fiber is connected to a 1550 nm laser source and the output fiber is connected to an optical power meter. Both optical power meter and CCD camera are connected to a computer. A polarization Controller (PC) is inserted between the laser source and the input fiber to control the light polarization state in the fiber before it is coupled into the Pt-NPs waveguide. Fine alignment is made by aligning the input and output fibers to obtain maximum transmitted power across the waveguide.

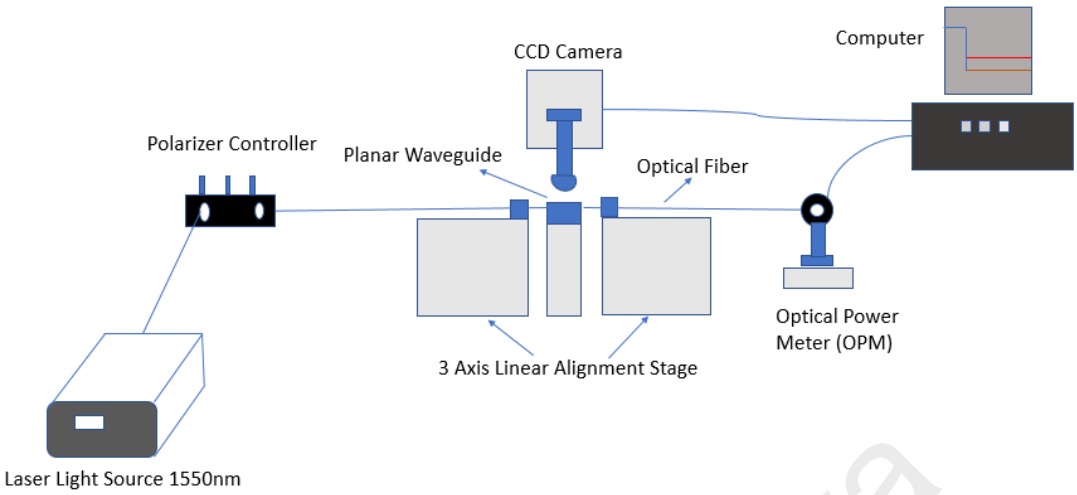

Figure 6.4: Planar waveguide experimental setup.

A total of 3 Pt-NPs coated waveguides were fabricated. The polarization extinction ratio (PER) of the planar waveguide with the Pt-NPs coating is first measured, the PER range from 2.5 dB to 5.5 dB. After Pt-NPs coating, the PER is increased to more than 11 dB. This indicates strong polarization dependent loss due to evanescent field interaction of light propagating in the waveguide with the Pt-NPs coating. The PER of the planar waveguide channels before and after Pt-NPs coating is summarized in Table 6.1.

Table 6.1: Shown the PER for planar waveguide (without coating and with coating) of Pt-NPs.

Waveguide channel	PER(dB) without Pt-NPs	PER(dB) with Pt-NPs
Channel-1	3.5 dB	14.7 dB
Channel-2	4.7 dB	16.1 dB
Channel-3	3.2 dB	13.8 dB

The electric field amplitude of the evanescent wave propagating parallel to the interface of the waveguide-Pt-NPs coating interface exponentially with distance normal to the interface, If the coating medium is non-absorbing, no energy loss will occur along the interface. However, if this medium has a large absorption coefficient, the intensity of the evanescent wave is attenuated and the transmitted power is reduced. The magnitude of this attenuation is affected by both the refractive index and absorption coefficient of the coating medium. The increase in PER indicates that the Pt-NPs coated waveguide exhibits a relatively large difference in refractive index for different light polarization states. For sensing application, the PC is adjusted to allow minimum power to be transmitted through the Pt-NPs coated waveguide, which corresponds to maximum evanescent field interaction with the Pt-NPs coating. Then, 0.5 μL of transformer oil is dropped onto the sensing region using a micropipette. The transmitted power level was measured for duration of 50 seconds starting from the application of the oil drop. The transformer oil on the sensing region is then rinsed with acetone and then dried with compressed dry air before subsequent measurement of transformer oil with different water content. The Pt-NPs coating is ensured to be intact and free of oil residue by measuring the transmission characteristics of the Pt-NPs coated waveguide before the subsequent application of transformer oil and ensuring that the values are the same as before the previous transformer oil application. The transmitted power of the sensor over time is shown in Figure 6.5. All readings are normalized to the transmitted power of the Pt-NPs waveguide before the transformer oil is applied. First transformer oil taken fresh from its container is used as reference. Upon application of the “fresh” transformer oil on the sensor, the transmitted power dropped by 2.0 dB. The transmitted power further decreases by 3.5 dB, 4.0 dB, 5.5 dB and 6.5 dB for transformer oil with 15 ppm, 16 ppm 18 ppm and 21 ppm of water content, respectively.

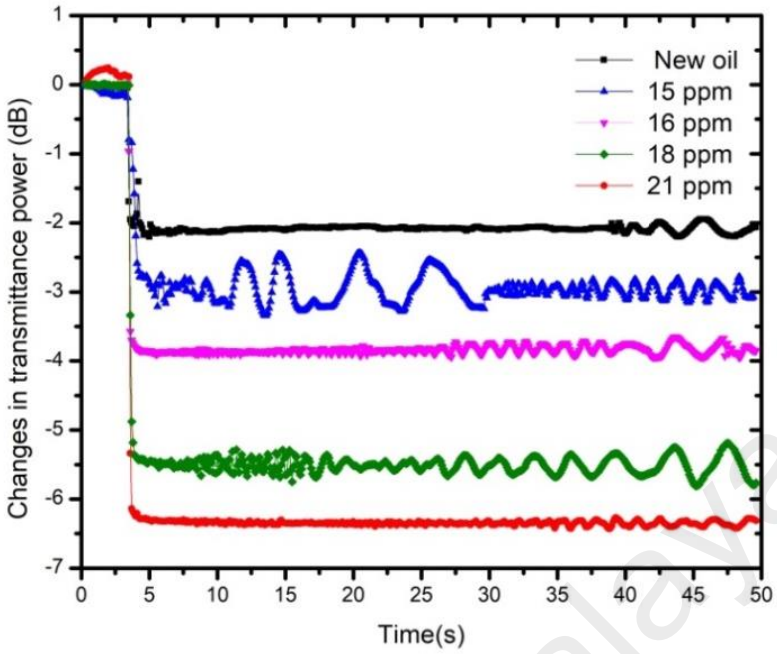

Figure 6.5: Power change for oils with the water content.

The increase in transmission loss is believed to be due to the increase in the Pt-NPs electrical conductance due to water adsorption. The increase in water content in transformer oil will increase water adsorption to the Pt-NPs coating and thus increasing the transmission loss of the Pt-NPs coated waveguides.

Change in the transmission loss of the Pt-NPs coated waveguide with water content in transformer oil is shown in Figure 6.6. It shows a good linear fitting, with the sensitivity of the sensor to water content in transformer oil calculated to be -0.561 dB/ppm, water content ranges from 15 ppm to 21 ppm. The experiment was repeated several times to determine the accuracy of the measurement and reproducibility of the system and displays a consistent result (Köllensperger, Karl, Ahmad, Pike, & Green, 2012; Liu, Tian, & Jiang, 2006; Mezher et al., 2016a).

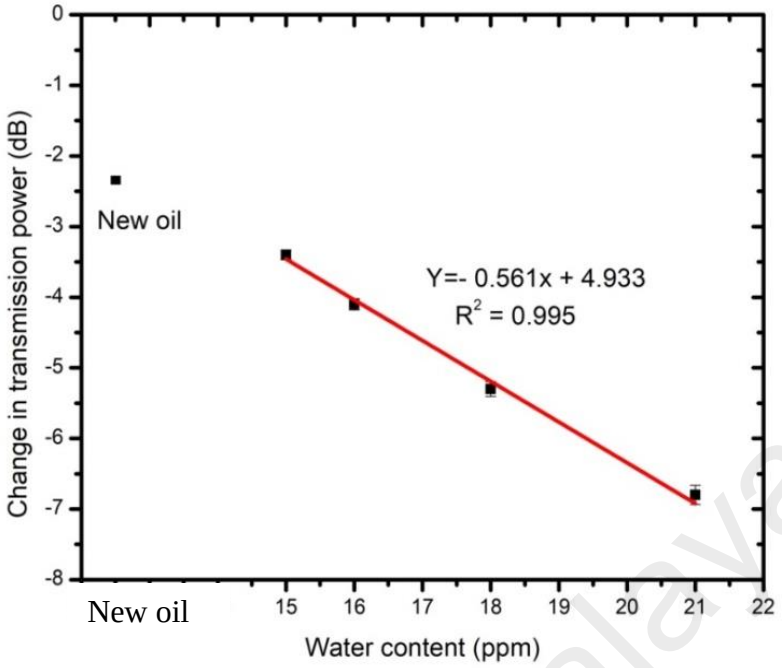

Figure 6.6: Shows the transmittance power change related to the water content.

6.6.2 Planar waveguide coating with Graphene Oxide

The GO sensor has been created by drop casting of GO solution on the waveguide channel. 2 drops of GO solution with single droplet volume of 2.4 μL are applied onto the waveguide channels. The coating is then allowed to dry for 20 to 25 minutes. Optical micrographs of the applied GO solution at different drying stages are shown in Figure 6.7. It can be seen that the size of the coating region remained the same throughout the drying process. The resulting GO coating has a diameter of 1.5 mm and its average thickness was measured using a Dektak D150 surface profiler to be 0.17 μm.

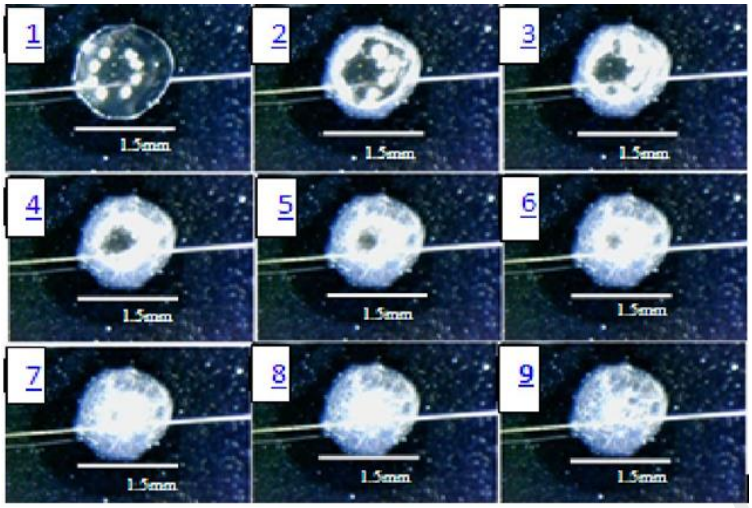

Figure 6.7: Graphene Oxide droplet applied on planar waveguide at different drying stages.

The PER of planar waveguide ranges from 2.5 dB to 5.5 dB and is increased to a range of between 10 dB to 15 dB after the GO coating. The polarization state of the input light is adjusted to allow minimum transmission through the GO-coated waveguide. Transformer oils with different water content are then applied on to the GO-coating region of the waveguide, and the change in transmission power measured.

Figure 6.8 shows the change in transmission power with the initial power (power level before application of transformer oil) referenced as 0 dB. Transmitted power level was measured for duration of 25 seconds from when the transformer oil is applied on to the GO-coated waveguide. For comparison, 0.5 μL of water is applied onto the GO-coated waveguide and the transmission power recorded. Transmission power increased instantaneously by about 15 dB because of water permeation into the GO coating (D. Zhang, Tong, & Xia, 2014). The response of the proposed sensor under ambient conditions when transformer oil droplet of 0.5 μL with different levels of water content was applied onto the sensing region was measured over time (Lewand, 2002a; Sparling & Aubin, 2007). It can be seen that the transmitted power increases almost immediately

after the oil sample is applied onto the sensing region (at the 1st second). For oil sample with higher water content, the transmitted power level increases further after the initial change and stabilized about 2 seconds after the oil sample is applied. Oil sample with 21 ppm of water content showed a largest increase in the transmitted power level of about 8 dB compared to oil sample with 16 ppm of water content, which is about 1 dB.

It was reported that GO film exhibits highly selective water molecules permeation with thickness up to 10 μm and these water molecules interact with the individual oxygen functional groups within the GO layers (Acik et al., 2010; Nair, Wu, Jayaram, Grigorieva, & Geim, 2012; Wei, Peng, & Xu, 2014). The interactions alter the GO dielectric properties by widening its bandgap, leading to a reduction in the conductivity and consequently decrease in the propagation loss in GO film and increasing the transmission of light (Jung et al., 2008; Lipatov et al., 2013; Yavari et al., 2010). Therefore, the propagation loss of the laser light in the GO film is reduced, resulting in the increase of the transmission of laser light. The result is the increase in transmitted power of the sensor with the increase water content indicates that water permeation into the GO film for dissolved is not significant. This phenomenon is consistent with water permeation rate through GO film increase of with increasing transmitted power (Geng et al., 2007; Nair et al., 2012). On the other hand, other solutions including transformer oil cannot permeate into the GO film, and therefore only interact with the GO-coated waveguide as a separate layer, resulting in very small changes to the transmission power characteristic. The higher water content in the transformer oil samples in turn results in the larger increase in transmission power.

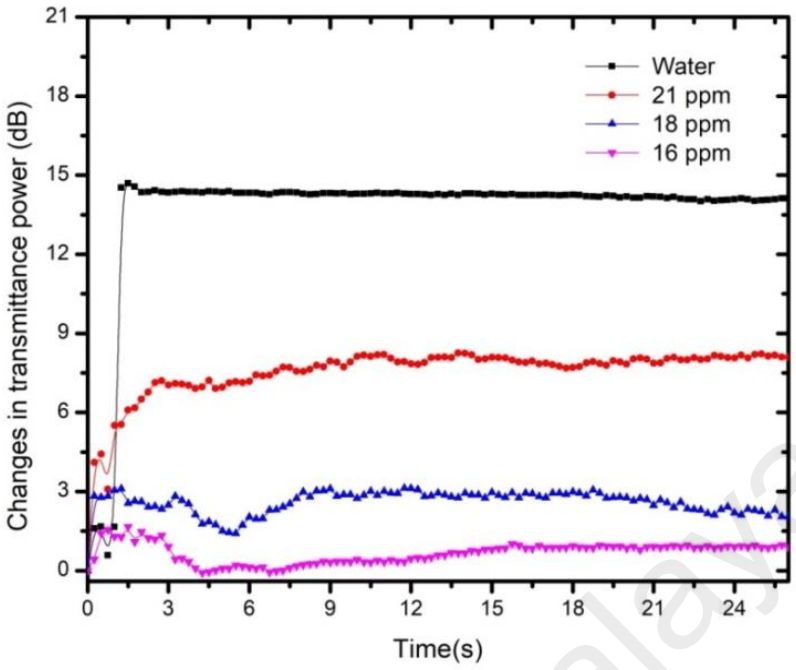

Figure 6.8: Temporal response of transmitted power level to transformer oil samples with different dissolved water and free water.

Figure 6.9 shows a linear relationship between the water content in the oil sample and the change in transmitted power within the range of 16 to 21 ppm. The sensitivity of the proposed sensor to water content is approximately 1.42 dB/ppm of water. The X-intercepts of the trendline cuts out at 15 ppm, which means that this sensor configuration has a lower water content detection limit of 16 ppm.

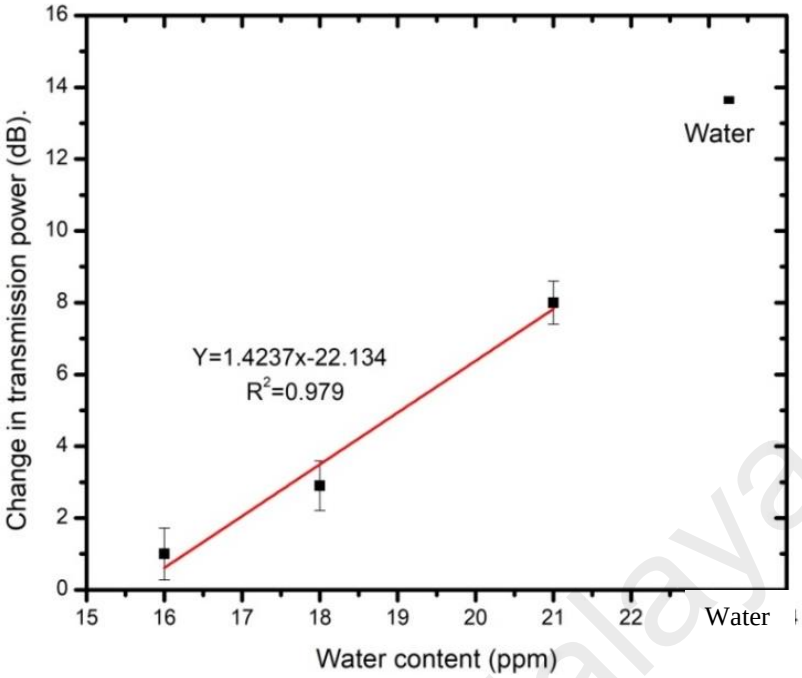

Figure 6.9: Shows power changes related to the water content.

6.6.3 D-Fiber Optics coating with Graphene Oxide

While GO-coated planar waveguide shows good response to water content in transformer oil, implementation of planar waveguide into harsh environment such as inside a high power transformer require packaging and mechanical bonding to optical fibers. The material used for the packaging may themselves contaminate the transformer oil as a result of material out-diffusion. Hence, efforts have been made to achieve optical sensing without the abovementioned issues.

The use of D-fiber as an alternative waveguide structure for GO-coated waveguide sensor is due to the following reasons:

1. It is easy to fabricate, as the entire structure is the optical fiber itself,
2. It does not require waveguide alignment and can be spliced directly to optical fiber connectors using established fusion splicing technology,
3. A better control of evanescent field can be achieved by controlling the polishing depth of the D-fiber,

4. By removing the polymer coating, an optical fiber can withstand high temperature processes such as thermal annealing up to 1000 ^{o}C.

These factors can be combined to develop a more sensitive and stable sensing device. In our experiment, the D-fiber has been fabricated using standard single mode fiber (SMF-28) to validate the principle of operation and feasibility. The fiber is first glued to a flat glass slide. The cladding and part of the core of the fiber are then removed using sandpaper abrasion to expose the evanescent field of light propagating in the fiber core to the surrounding medium. Hence the total power at the output is modulated by the optical properties of the surrounding medium. The D-fiber structural was performed using field emission scanning electron microscopy (FESEM, Hitachi model SU8000). Figure 6.10 (a) shows the FESEM image of the polished surface still glued on the glass slide. The polished fiber can be easily removed from the glass slide by heating the slide to 140^{o}C which soften the glue. Figure 6.10(b-e) shows the cross section of the removed D-fiber with magnification of 260x, 500x, 1000x and 2000x, respectively. Gradual tapering of the polished section of the fiber can be seen from Figure 6.10(b) and (c), and the surface of the polished fiber shows surface roughness comparable to the cleaved edge of the fiber.

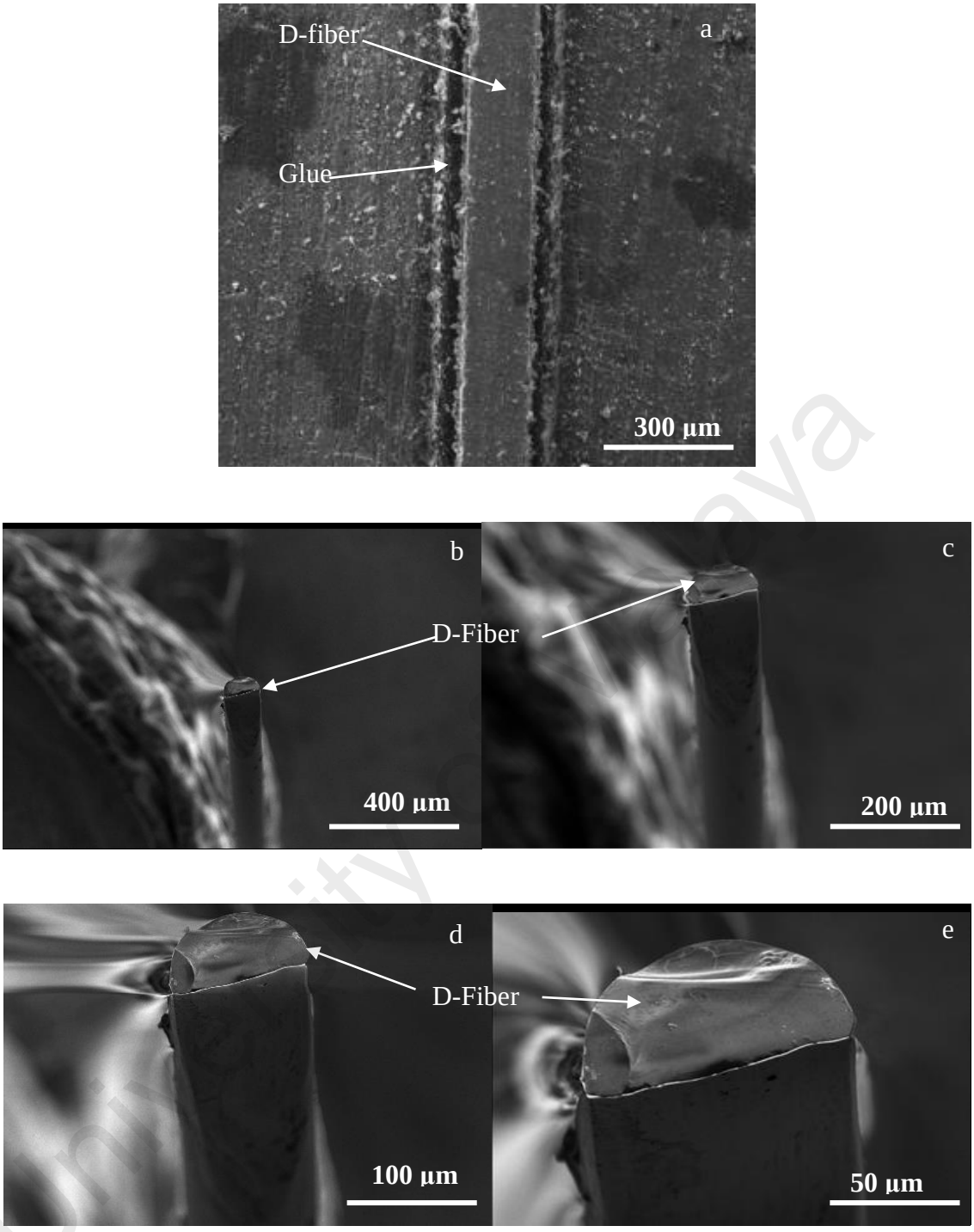

Figure 6.10: (a) FESEM images of the top view of side polished SMF and (b-e) side view of the polished SMF at different magnifications.

The response of the D-fiber without the GO-coating to transformer oil samples is first measured. The result is shown in the Figure 6.11, it can be seen that the transmitted power decreases almost immediately after transformer oil droplet is applied onto the sensing region (at the 6th second). In contrast, when water droplets are applied, the transmitted power increases by about 3 dB instead. This indicates that the refractive index of transformer oil is higher that the optical fiber core, thus causing light leakage into the transformer oil covering the D-fiber region(Acik et al.; Mathew, 2013). Also, transmitted power level of the D-fiber when transformer oil samples are applied shows large fluctuation over time, which is indicated by the vertical error bars in Figure 6.12. This makes transmitted power change between transformer oil with different water content in distinguishable.

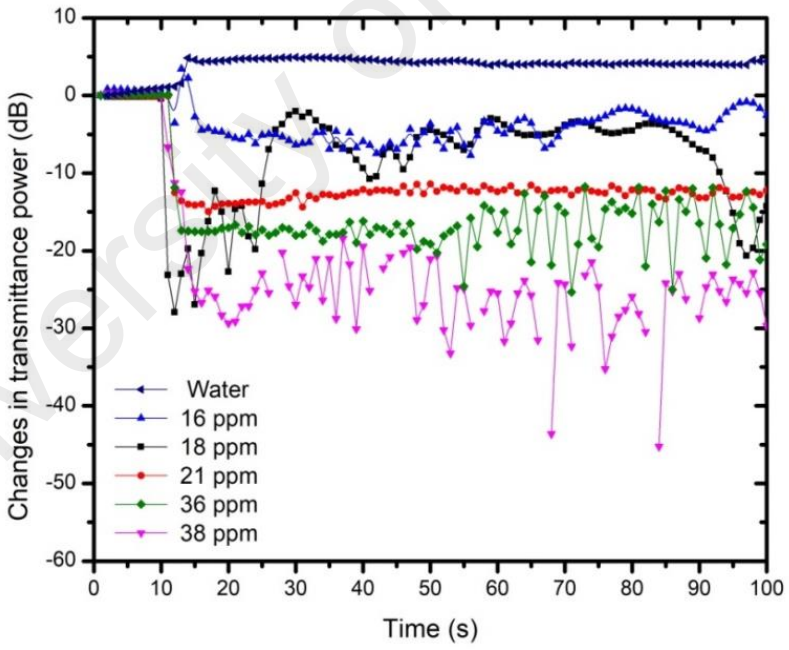

Figure 6.11: Temporal response of transmitted power level to transformer oil samples with different dissolved water using D-Fiber only.

Figure 6.12 shows the change in transmitted power for different water content in the oil sample. The fluctuation in power during 100 second may not give accurate reading, but we can take the average of the power. It shows a relationship between water content in oil and the change in transmitted power within the range of 16 to 38 ppm. The sensitivity of the proposed sensor to water content dissolved in transformer oil is calculated to be -0.60 dB/ppm of water.

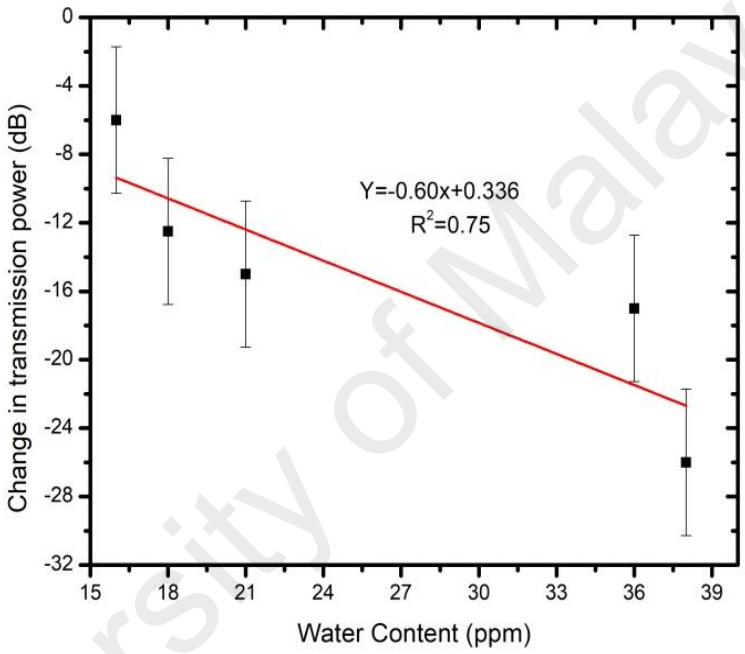

Figure 6.12: Response curve of transmitted power with different water content using D-fiber.

GO solution is then drop-casted onto the D-fiber to form GO-coated D-fiber. 1 drop of GO solution with droplet volume of 2.4 μL is applied onto the surface of D-fiber and spread along the polished length of the D-fiber. The coating is then allowed to dry for 15 minutes. The GO-coated D-fiber is shown in Figure 6.13. The GO-coating length is about 2 mm. The average thickness of GO-coating was measured using a Dektak D150 surface profiler to be 0.08~ μm.

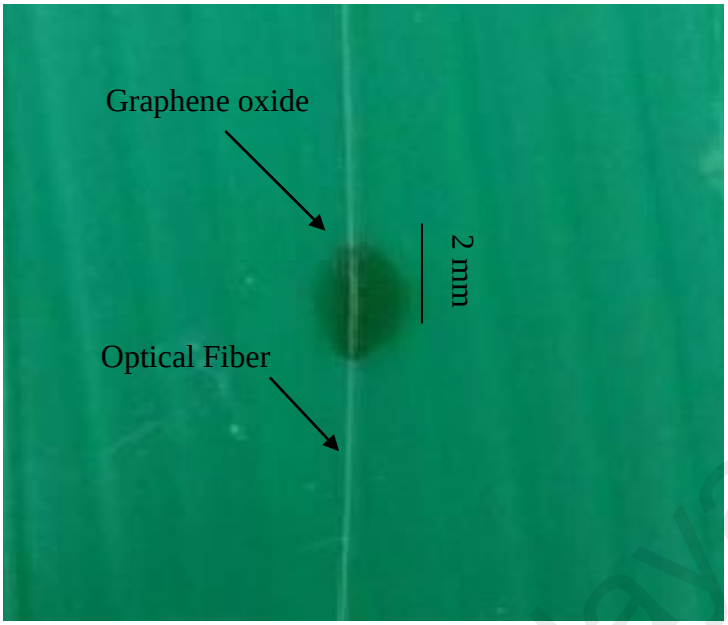

Figure 6.13: Stages of the drying of GO solution drop on the D-fiber.

The response of the GO-coated D-fiber to transformer oil with different levels of water content was measured. 0.5 μL of transformer oil is applied onto the sensing region. The transmission power measurement was carried out over a period of 40 seconds with 1 second intervals. Transformer oil is applied at about 4 seconds after power measurement starts. The results are shown in Figure 6.14. It can be seen that the transmitted power increases after the oil sample is applied onto the sensing region (at the 5^{th} second). Power fluctuations occur in the first 10 seconds after the oil sample is applied. For transformer oil with 15 ppm and 21 ppm of water content, transmission power increases to a maximum, before stabilizing at a lower power level. On the other hand, for transformer oil with 16 ppm and 18 ppm of water content, transmission power increases gradually and stabilizes after 3 and 10 seconds, respectively. The stabilized transmission power level increases with the amount of water content. The oil sample with 15 ppm of water content causes a transmission power increase of 5 dB, while oil sample with 21 ppm of water content showed the largest increase of 18 dB. As comparison, water is applied to the GO-coated D-shaped fiber and the transmission

power level increases by 23 dB immediately after the application of water drop with the minimum power fluctuation. The result indicates that water in the oil samples permeates into the GO coating, which results in a decreased transmission loss of the GO-coated D-shaped fiber (Nair et al., 2012).

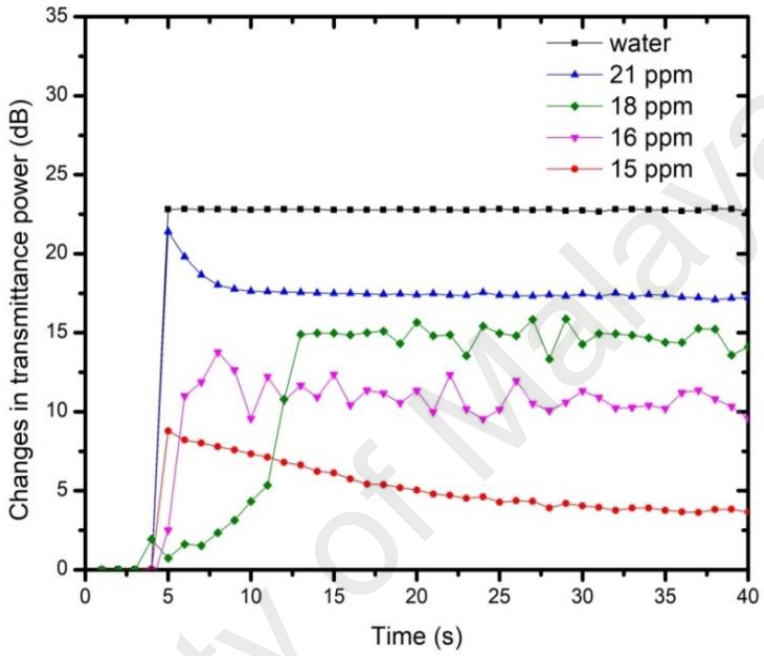

Figure 6.14: Temporal response of transmitted power level to transformer oil samples with different dissolved water and free water content.

Figure 6.15 shows the change in transmitted power for different water content in the oil sample within the range of 15 to 21 ppm. The sensitivity of the proposed sensor to water content dissolved in transformer oil is calculated to be 1.87 dB/ppm of water. The X-intercept is at about 15 ppm, which translate into a lower water content detection limit of >11 ppm.

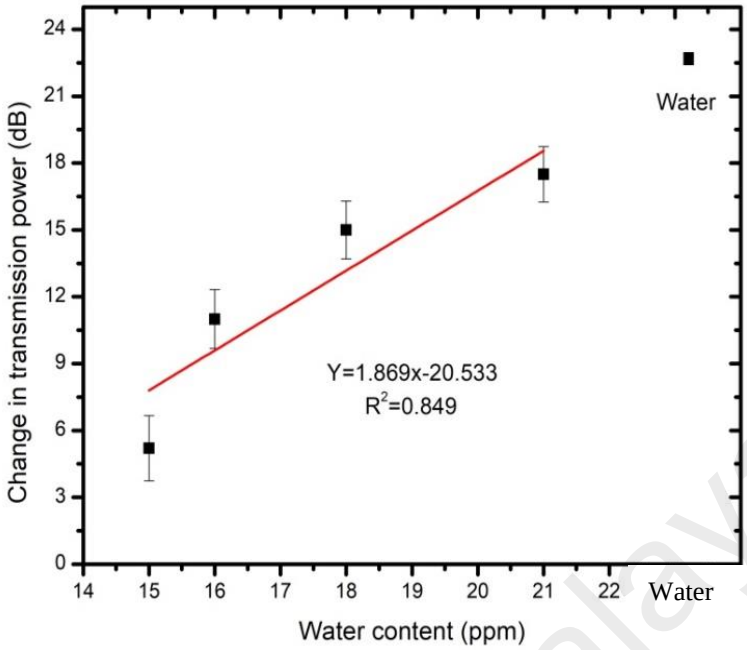

Figure 6.15: Shows the transmitted power with different water content.

The power fluctuation of the GO-coated D-fiber is believed to be due the thin GO-coating, which allows the evanescent field of the fiber core to interact with the transformer oil beyond the GO coating. Therefore, D-fiber with thicker GO-coating is prepared to study the effect of GO-coating thickness on the transmission power stability of the GO-coated D-fiber. The D-Fiber is coated with 3 drops of GO solution with volume 2.4 µl. The coating is then allowed to dry for 20-25 minutes. The GO-coating covers the entire polished length of the D-fiber and have a thickness of 0.22~ µm. The PER of the GO-coated D-fiber is measured to be 15 dB. The GO-coated D-fiber is then tested using different transformer oil samples. Water droplet is used as reference. Figure 6.16 shows the change in transmission power level of the GO-coated D-fiber when transformer oil droplets with different water content are applied onto the GO-coating. The application of water droplet results in the transmission power level increase of 13 dB, while transformer oil with 38 ppm of water content shows the largest increase in the transmitted power level among oil samples of about 9.7 dB. Transmitted power level

decreases for oil samples with lower water content and is lowest for oil sample with 16 ppm water content, which is about 2.3dB. This is a similar trend compared to the response of previously demonstrated GO-coated waveguide. What is different for the current GO-coated D-fiber is the relatively more stable power level measured over time after the oil sample droplet is applied, which is an improvement from the response of previous configurations of GO-coated waveguide. This will improve the measurement resolution of water content in transformer oil.

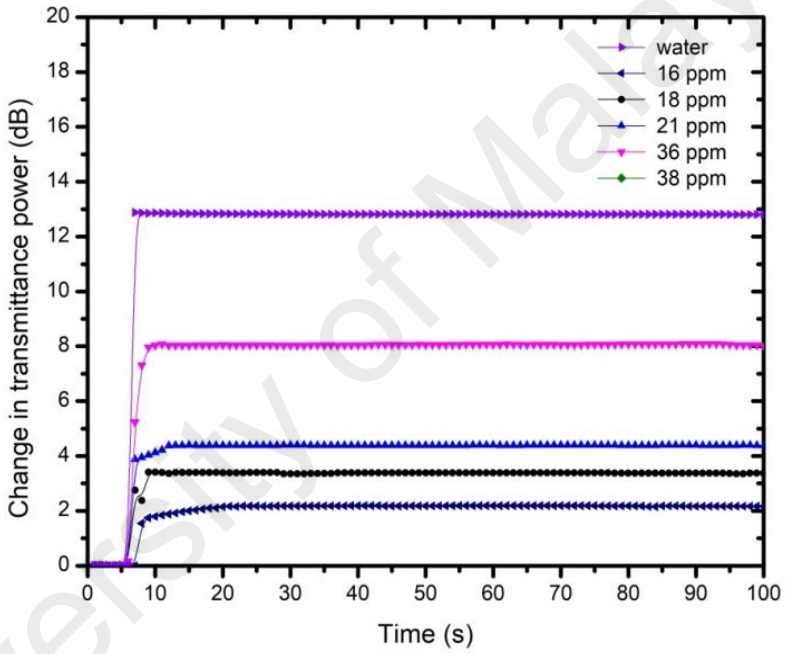

Figure 6.16: Temporal response of transmitted power level to transformer oil samples with different dissolved water using D-fiber coating by GO.

However, there is a trade-off for transmitted power level stability, which is the sensitivity. Figure 6.17 shows the change in transmitted power for different water content in the oil sample. It shows a linear relationship between water content in oil and the change in power transmittance within the range of 16 to 38 ppm. The sensitivity of the proposed sensor to water content dissolved in transformer oil is calculated to be 0.30 dB/ppm of water, which is about 6 times lower compared to D-fiber with thinner GO

coating. The lower detection limit is lower at >6 dB, possibly due to the higher resolution of the sensor as a result of improved transmission power level stability over time.

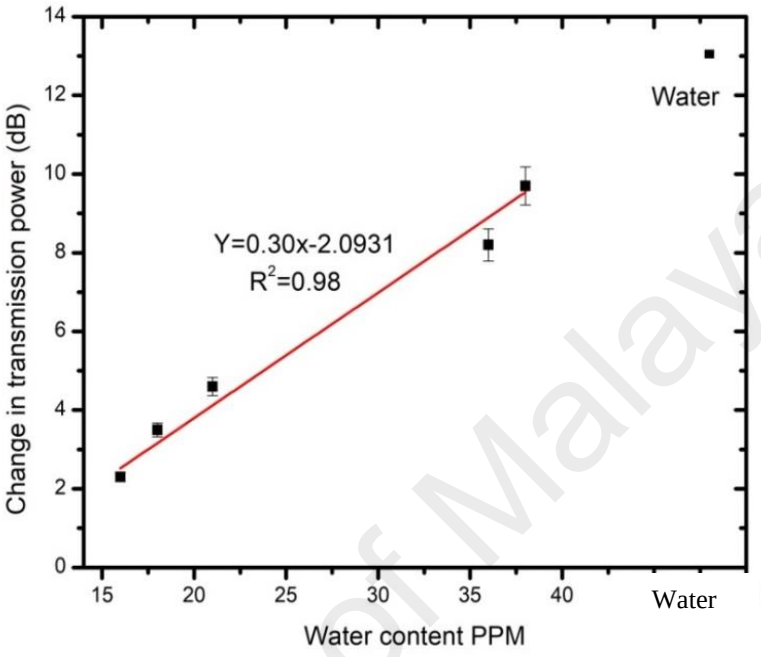

Figure 6.17: Response curve of transmitted power with different water content using GO coated on D-fiber.

To simulate the continuous change of water content in transformer oil, the GO-coated D-fiber is inserted into a fluidic channel made using PDMS. The fluidic channel is illustrated in Figure 6.18. It consists of a PDMS block with a through hole of 300 μm in diameter. Two additional holes are bored near both ends of the through hole for a distance until the through hole, forming a U-shaped fluidic channel. GO-coated D-fiberis then threaded through the through hole with the GO-coated region situated between the two vertical holes. Both ends of the through holes are then sealed using epoxy glue. The two vertical holes are connected with diameter of 2 mm. Transformer oil samples are then channel through the fluidic channel by injecting the oil into the medical tube using a syringe. The other end of the medical tube is connected to a

vacuum pump to assist fluid flow within the fluidic channel. Transmission power level of the GO-coated D-fiber is measured during with different oil samples channeling through the fluidic channel.

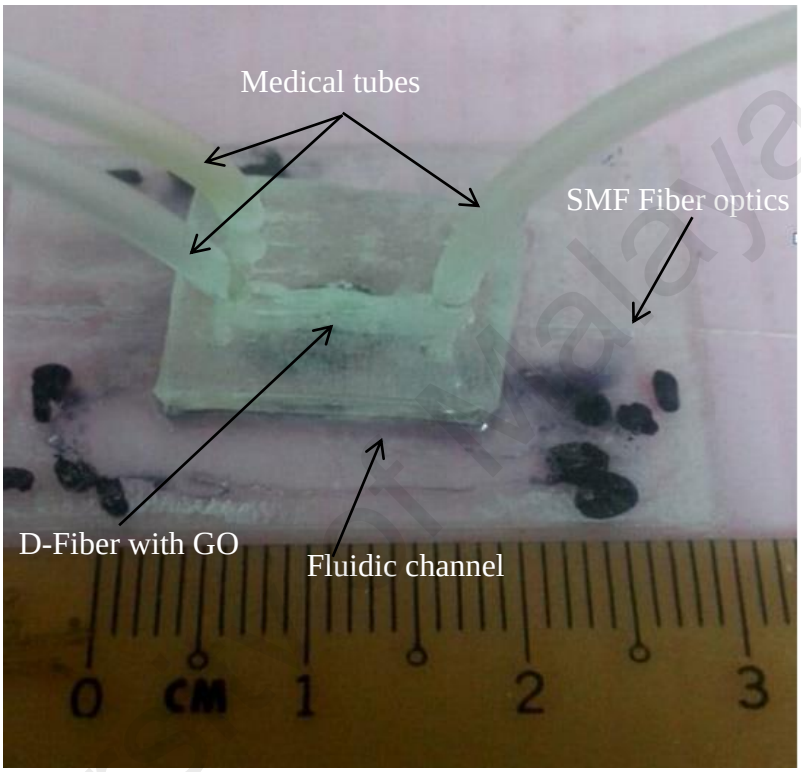

Figure 6.18: Physical view of D-Fiber coated by GO and cover PDMS.

The change in transmitted power over time is shown in Figure 6.19. Transmission power level changes by less than 1 dB after the first 1000 seconds with the vacuum pump switched on and ambient air flowing through the fluidic channel. When the transformer oil with 21 ppm of water content is introduced to the fluidic channel, the transmitted power level increases almost immediately by 24 dB before stabilizing at about 20 dB. When fresh transformer oil (new oil) is introduced to the fluidic channel, the transmitted power level dropped to about 18.3 dB. The transmitted power level increases to about 19.7 dB when transformer oil with 18 ppm of water content is

introduced before dropping back to 18.5 dB when fresh transformer oil is again introduced into the fluidic channel. Oil sample with 38 ppm of water content shows the largest increase in transmitted power level of about 24 dB, where oil sample with 36 ppm of water content shows increase in transmitted power level of about 23.7 dB while oil sample with 16 ppm water content shows smallest change in transmitted power level of 19.4 dB. Spikes in transmitted power level are measured when transformer oils with different water contents are flowed through the GO-coated D-fiber (for example, when transformer oil with 21 ppm of water content is initially flowed, and during the transition between transformer oil with 21 ppm of water content to new oil, and from new oil to transformer oil with 16 ppm of water content).

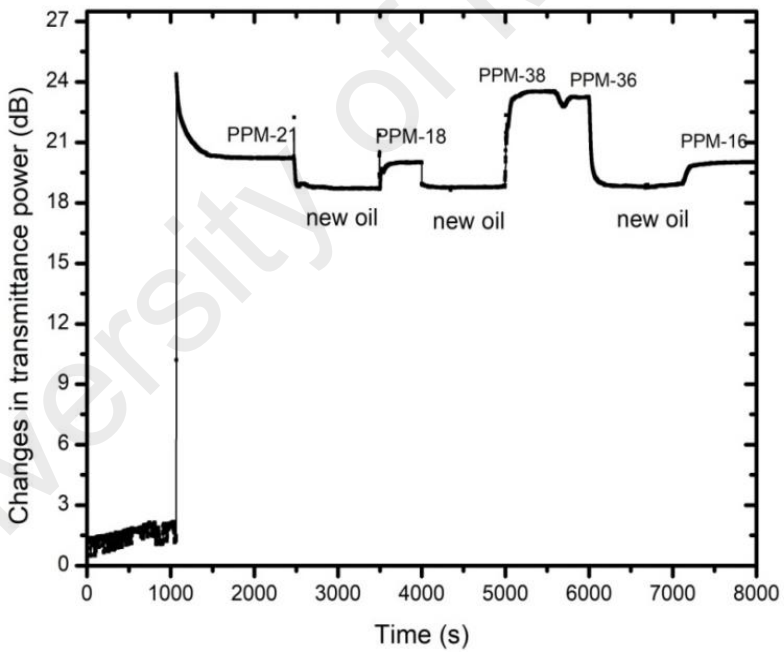

Figure 6.19: Temporal response of transmitted power level to transformer oil samples with different dissolved water using D-fiber coating by GO and cover by PDMS.

Figure 6.20 shows the change in transmitted power for transformer oil with different water content. It shows a linear relationship between for water content between 16 to 38 ppm. The sensitivity of the proposed sensor to water content dissolved in transformer oil is calculated to be 0.18 dB/ppm of water. It is less sensitive compared to GO-coated D-fiber before insertion in the fluidic channel. The performances of GO-coated D-fiber sensors are summarized in Table 6.2 below.

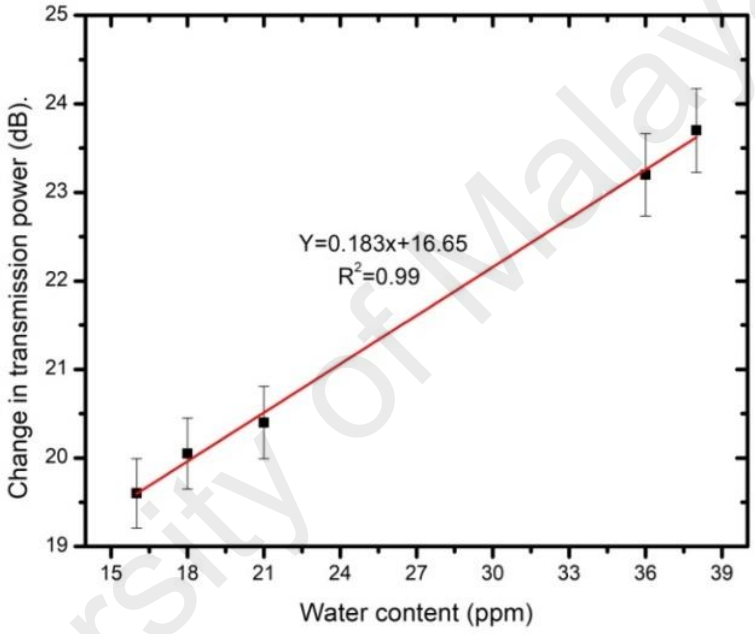

Figure 6.20: Response curve of transmitted power with different water content using PDMS.

Table 6.2: Show the parameter of the D-fiber and dissolved water.

Parameter		D-Fiber	1 drop of coating GO	3 drop of coating GO	3 drop of GO and PDMS
	15	NA	5.2 dB	NA	NA
Water content (ppm)	16	- 6 .1 dB	11.5 dB	2.3 dB	19.7 Db
	18	-12.5 dB	15 dB	3.5 dB	20.1 dB
	21	-15 .1dB	17.5 dB	4.6 dB	20.3 dB
	36	-17.2 dB	NA	8.9 dB	23.2 dB
	38	-26 dB	NA	9.7 dB	20.7 dB
R^2		0.75	0.849	0.980	0.998
Sensitivity (dB/ppm)		-0.6	1.869	0.30	0.183
Error		0.33	-20.53	-2.09	16.65

6.6.4 D-Fiber Optics coating with Platinum nanoparticles

In addition to GO-coated D-fiber, the transmission power characteristics of D-fiber coated with platinum nanoparticle (Pt-NP) layer is also studied. The thin film coated D-fiber with thickness of 55 nm using sputter coater and coated D-fiber undergoes thermal treatment at 360 ^{o}C for 4 hours to form Pt-NPs.

Figure 6.21 shows the change in transmitted power when oil sample was drop on the sensing region of the fiber. From the plots, the response time for transmitted power changed to lower values shows that the sensor is having a fast response and high sensitivity. This observation could be due to the rapid adsorption rate of the sensor as the water molecules from the transformer oil react with the platinum surface in an

equilibrium environment. It is clearly seen that for oil sample with water content range from 15 ppm to 21 ppm, transmitted power level changes from 1.8 dB to 7.0 dB.

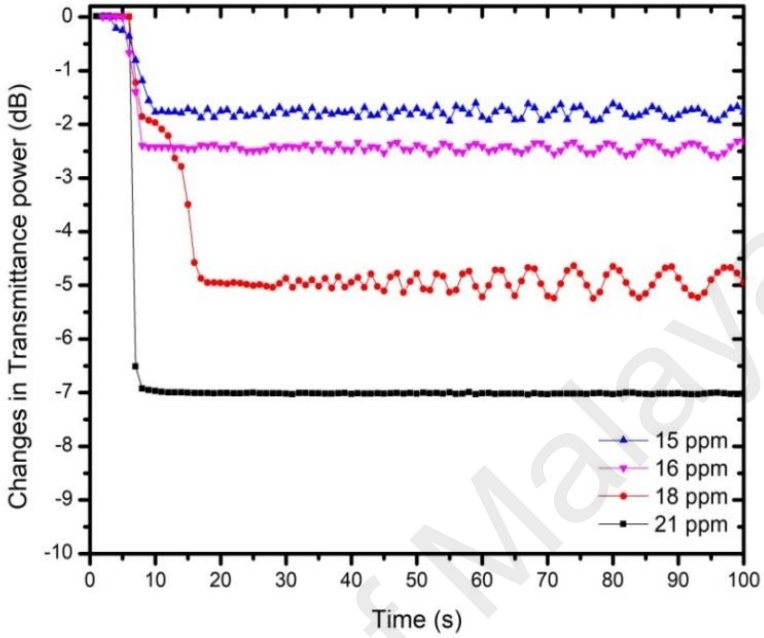

Figure 6.21: Temporal response of transmitted power level to transformer oil samples with different dissolved water using D-fiber coating by platinum nanoparticles.

Figure 6.22 shows the change in transmitted power for transformer oil with different water content. It shows a linear relationship between for water content between 16 to 21 ppm. The sensitivity of the proposed sensor to water content dissolved in transformer oil is calculated to be -0.88 dB/ppm of water.

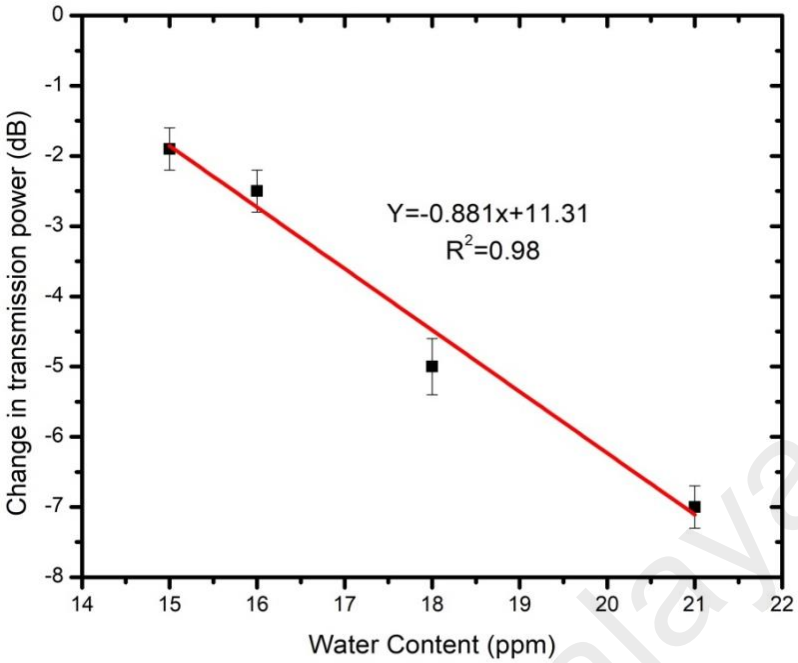

Figure 6.22: Graph of average of Transmitted power drop for four samples of aged oil with different water content.

CHAPTER 7: CONCLUSIONS

7.1 Summary

We present a study of the optical characteristics of metal and graphene oxide nanolayers and their application in optical sensing. The nanolayers are coated using different approaches such as electron beam evaporation, electrochemical deposition and drop casting technique. Gold and silver nanoparticle layers were fabricated using electron beam evaporation followed by subsequent thermal annealing at different temperature and duration to achieve de-wetting of the metal thin film. Morphological analysis was carried out to study the shape and size of the produced nanoparticles. The gold and silver nanoparticles have sizes ranging from 11 nm to 45 nm and 15 nm to 54 nm, respectively. Meanwhile, bilayer Au/Ag-NPs have also been fabricated with particle size in the range between 23 and 26 nm. On the other hand, the effects of nanostructures were studied using silver micro-flowers (Ag-MFs) with sizes of ~150-500 nm and platinum 'dome-like' nanostructures (Pt-NSs). Absorption spectroscopy was carried out to study the Surface Plasmon Resonance (SPR) of the nanoparticle layers. The shape and size of the nanoparticles are observed to affect the shifting of SPR wavelengths.

Nonlinear optical properties were obtained for different structures of nanolayers using Z-scan technique. The nonlinear refractive index and nonlinear absorption coefficient of the nanolayers were determined. The size of Au-NPs contribute to increase the nonlinear optical properties such as the Au-NPs with 11 nm show lower magnitude of nonlinear optical properties shows NLA is 2.26×10^{-4} cmW^{-1} where NLR is - 1.77×10^{-8} cm^2 W^{-1} while the 25 nm show increase in magnitude of NLA is 2.62×10^{-4} cmW^{-1} where NLR is - 2.16×10^{-8} cm^2 W^{-1}.

Meanwhile, Hybrid Au/Ag-NPs showing nonlinear optical properties between Au-NPs and Ag-NPs. The magnitudes of nonlinear optical effects Au/Ag-NPs where the values of NLA is $3.87x10^{-4}$ cmW^{-1} and NLR is -5.48×10^{-9} cm^2 W^{-1}, where Au-NPs value of NLA is $1.47x10^{-4}$ cmW^{-1} and NLR is -3.21×10^{-9} cm^2 W^{-1} and Ag-NPs shows NLA of 4.8710^{-4} cmW^{-1} and -7.94×10^{-9} cm^2 W^{-1}, respectively.

Ag-MFs are another structure has been study with increasing deposition time will cause increasing in the shape and sizes of micro flower and resulting increase nonlinear optical properties. The nonlinear optical properties of Ag-MFs with different thickness, Ag-MFs with 50nm show NLA of $2.28x10^{-4}$ cmW^{-1} where NLR is -2.11 $x10^{-9}$ cm^2 w^{-1}, 70 nm shows NLA of $2.30x10^{-4}$ cmW^{-1} where NLR is -2.22 $x10^{-9}$ cm^2 w^{-1} and 160nm shows NLA as $2.33x10^{-4}$ cmW^{-1} where NLR is -3.71 $x10^{-9}$ cm^2 w^{-1}, respectively.

Due to thermal effect, nonlinear absorption and nonlinear refraction index are not constant values and dependent on the incident intensity. Increasing the applied intensity on Pt-NSs show reduce NLA and NLR values and also for nitrogen doped graphene show reduce in NLA and NLR when increase the incident intensity. The different intensity apply on Pt-NSs from 49.87 to 348.50 I_0 $MWcm^{-2}$ which NLA value reduce from 27.4 $x10^{-4}$ to 4.7 $x10^{-4}$ cmw^{-1} and NLR value reduce from -4.21 x 10^{-8} to -1.35x 10^{-8} cm^2w^{-1}. The different incident intensity apply nitrogen doped graphene from 107.62 to 526.80 $MWcm^{-2}$ show reduce in NLA and NLR. Where NLA value reduce from 3.11 $x10^{-4}$ to 2.17 $x10^{-4}$ cm $w^{-1}$and NLR value reduce from $-9.77x10^{-9}$ to $-3.42x10^{-9}$ cm^2w^{-1}. Nonlinear optical properties of GO have been done for two thickness 0.17μm and 0.22 μm. The nonlinear optical properties increasing when the thickness increase, GO with thickness from 0.17 μm to 0.22 μm, show increase in the magnitude of NLA ($2.0x10^{-4}$ to 2.2 $x10^{-4}$) cmW^{-1} and NLR magnitude increase from ($-2.696x10^{-9}$ to $-3.21x10^{-9}$)

$cm^2\ W^{-1}$, respectively. We further investigate the ability of selected nanolayers for the detection of water content in transformer oil.

Selected nanolayers (Platinum and Graphene oxide) are applied on optical waveguides for detection the water content in transformer oil.

Pt-NPs have been coated on planar waveguide and D-Fiber, to test for water content in transformer oil. Four samples of oil were picked from the actual transformer with different values of water contents (15 ppm, 16 ppm, 18 ppm, and 21 ppm). The oil samples were drop on the sensing region of the sensor and resulting to the drop of transmission power from the initial value. The transmitted power level reduces when the water content increases due to increase water adsorption to the Pt-NPs. The Pt-NPs coated planar waveguide sensor shows the sensitivity to dissolved water in transformer oil of -0.561 dB/ppm while Pt-NPs coated D-Fiber sensor shows a sensitivity of -0.88dB/ppm.

GO have been coated on planar waveguide and D-Fiber to exam the water content in transformer oil. The drop casting technique is a method used to coat GO solution on the SU-8 channel of wave guide sensor. The guide sensor coated with GO with 1550 nm wavelength registers increasing in the transmitted power. Increasing in the transmitted power is measured with increase the water content. They observed that water molecule can change optical transmission characteristics of the sensor by penetrate the water inside the GO resulting decreasing the conductivity by further widened the band gap. Meanwhile, power transmittance increases when the dissolved water is higher is attributed by reducing the conductivity of GO films. Experiments were carried out for free water and the dissolved water in the oil range from 16 ppm to 21 ppm. GO have been coated on planar waveguide and D-Fiber to measure the water content in transformer oil. Depending on the GO coating thickness, the sensitivity range from 0.3

dB/ppm of water content in transformer oil to 1.86 dB/ppm of water content in transformer oil. The stability of the sensor output is inversely proportionate to the sensitivity, meaning there is a compromise between the two parameters when considering devising optical sensors in this configuration. The GO-coated waveguide sensor is further tested with continuous varying water content in transformer oil using a fluidic channel structure, and the result shows that the sensor is able to discern changes in water content in transformer oil in simulated environment.

7.2 Future Work

For future work, the proposed sensor can be packaged and installed in an operating transformer to study its performance in real environment. The proposed remote optical monitoring configuration is shown in Figure 7.1. The oil circulates between the transformer and radiator due to thermo-syphon effect. In some transformer, the circulation is assisted by an oil pump. The insulation oil covered all the internal part in transformer. The proposed sensor probe will be inserted in the line between the transformer and the radiator as shown in Figure 7.1.

The sensor probe package will require input and output ports, for connection to the laser source with wavelength at 1550 nm and to an optical power meter for power measurement.

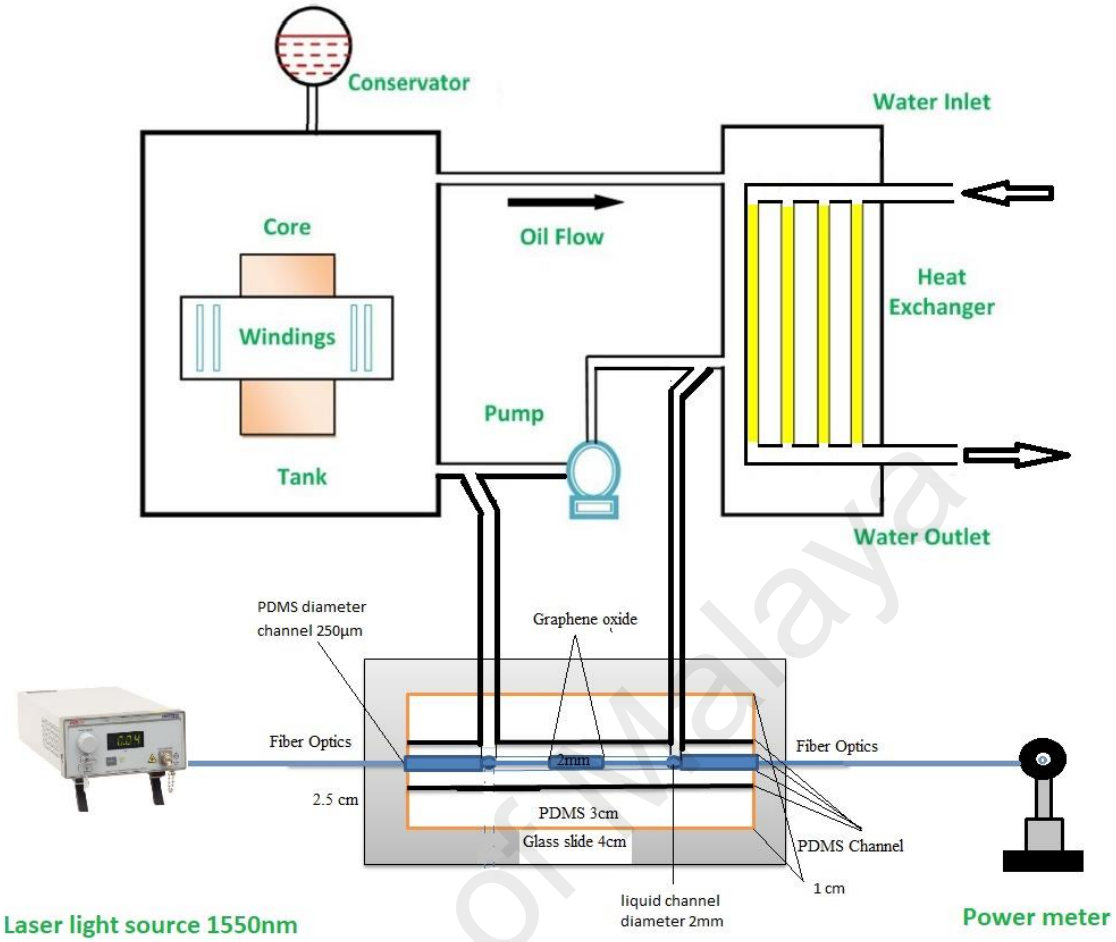

Figure 7.1: Figure shows the flow of the oil from the transformer to optical sensor.

REFERENCES

Acik, M., Mattevi, C., Gong, C., Lee, G., Cho, K., Chhowalla, M., & Chabal, Y. J. (2010). The role of intercalated water in multilayered graphene oxide. *Acs Nano*, 4(10), 5861-5868.

Adekoya, S. O., Eleruja, M. A., Olofinjana, B., Akinwunmi, O. O., Taleatu, B. A., & Ajayi, E. O. (2012). Enhanced Light Absorption in Textured Metal Organic Chemical Vapour Deposited (MOCVD) CdO Thin Films. *MRS Online Proceedings Library Archive*, 1432.

Adel, C.-e. B., Alexandre, R. B., Xavier, R. L., Jean-Jacques, E. G., & Olivier, E. G. L. (2003). Generation and amplification of surface plasmon polaritons at telecom wavelength with compact semiconductor-based devices .

Agnihotri, S., Mukherji, S., & Mukherji, S. (2014). Size-controlled silver nanoparticles synthesized over the range 5–100 nm using the same protocol and their antibacterial efficacy. *RSC Advances*, 4(8), 3974-3983.

Ara, M. M., Dehghani, Z., & Iranizad, S. S. (2008). Synthesis, characterization and single-beam Z-scan measurement of the third-order optical nonlinearities of ZnO nano-particles. *International Journal of Modern Physics B*, 22(18n19), 3165-3171.

Ara, M. M., Dehghani, Z., Sahraei, R., Daneshfar, A., Javadi, Z., & Divsar, F. (2012). Diffraction patterns and nonlinear optical properties of gold nanoparticles. *Journal of Quantitative Spectroscopy and Radiative Transfer*, 113(5), 366-372.

Atwater, H. A., & Polman, A. (2010). Plasmonics for improved photovoltaic devices. *Nat Mater*, 9(3), 205-213.

Bahadır, E. B., & Sezgintürk, M. K. (2015). Applications of commercial biosensors in clinical, food, environmental, and biothreat/biowarfare analyses. *Analytical Biochemistry*, 478, 107-120.

Bai, S., Li, Q., Zhang, H., Chen, X., Luo, S., Gong, H., Qiu, M. (2015). Large third-order nonlinear refractive index coefficient based on gold nanoparticle aggregate films. *Applied Physics Letters*, 107(14), 141111.

Banerjee, A., Mukherjee, S., Verma, R. K., Jana, B., Khan, T. K., Chakroborty, M., Singh, V. (2007). Fiber optic sensing of liquid refractive index. *Sensors and Actuators B: Chemical*, 123(1), 594-605.

Barker, S. L., Kopelman, R., Meyer, T. E., & Cusanovich, M. A. (1998). Fiber-optic nitric oxide-selective biosensors and nanosensors. *Analytical Chemistry*, 70(5), 971-976.

Bhushan, B. (2017). *Springer Handbook of Nanotechnology*: Springer.

Bischof, J., Scherer, D., Herminghaus, S., & Leiderer, P. (1996). Dewetting modes of thin metallic films: nucleation of holes and spinodal dewetting. *Physical Review Letters*, 77(8), 1536.

Boehm, H. P., & Scholz, W. (1965). Der „Verpuffungspunkt" des Graphitoxids. *Zeitschrift Für Anorganische and Allgemeine Chemie*, 335(1-2), 74-79.

Bohren, C., & Huffman, D. (1998). *Absorption and Scattering of Light by Small Particles:* Wiley-VCH.

Bond, A. M. (2002). Broadening Electrochemical Horizons: Principles and Illustration of Voltammetric and Related Techniques: Oxford University Press.

Brodie, B. C. (1859). On the atomic weight of graphite. *Philosophical Transactions of the Royal Society of London*, 149, 249-259.

Brownson, D. A., & Banks, C. E. (2014). *The Handbook of Graphene Electrochemistry:* Springer.

Cai, D., Lu, Y., Lin, K., Wang, P., & Ming, H. (2008). Improving the sensitivity of SPR sensors based on gratings by double-dips method (DDM). *Optics Express*, 16(19), 14597-14602.

Chan, K., Ito, H., & Inaba, H. (1984). An optical-fiber-based gas sensor for remote absorption measurement of low-level CH 4 gas in the near-infrared region. *Journal of Lightwave Technology*, 2(3), 234-237.

Chapple, P., Staromlynska, J., Hermann, J., Mckay, T., & McDuff, R. (1997). Single-beam Z-scan: measurement techniques and analysis. *Journal of Nonlinear Optical Physics & Materials*, 6(03), 251-293.

Cheng, J. (2011). Broadband Dieletric Properties of Impregnated Transformer Paper Insulation at Various Moisture Contents.

Colak, S., & Aral, E. (2005). SEM, EDX and UV spectrums of Fe_2O_3 doped soda-lime-silica glasses. *Romanian Journal of Physics*, 50(9/10), 1041.

Cole, J., Johnson, R., & Bhuta, P. (1977). Fiber-optic detection of sound. *The Journal of the Acoustical Society of America*, 62(5), 1136-1138.

Couture, M., Zhao, S. S., & Masson, J.-F. (2013). Modern surface plasmon resonance for bioanalytics and biophysics. *Physical Chemistry Chemical Physics*, 15(27), 11190-11216.

Cullen, D., Brown, R., & Lowe, C. (1987). Detection of immuno-complex formation via surface plasmon resonance on gold-coated diffraction gratings. *Biosensors*, 3(4), 211-225.

Cusano, A., Cutolo, A., & Giordano, M. (2008). Fiber Bragg gratings evanescent wave sensors: A view back and recent advancements. *Sensors*, 113-152.

Da Costa Silva, L. M., dos Santos, V. P. S., Salgado, A. M., & Pereira, K. S. (2013). Biosensors for contaminants monitoring in food and environment for human and

environmental health *State of the Art in Biosensors-Environmental and Medical Applications:* InTech.

Daghestani, H. N., & Day, B. W. (2010). Theory and applications of surface plasmon resonance, resonant mirror, resonant waveguide grating, and dual polarization interferometry biosensors. *Sensors*, 10(11), 9630-9646.

Dancus, I., Vlad, V., Petris, A., Gaponik, N., Lesnyak, V., & Eychmüller, A. (2010). Optical limiting and phase modulation in CdTe nanocrystal devices. *Journal of Optoelectronics and Advanced Materials*, 12(1), 119.

Dao, K. A., Nguyen, T. T., Nguyen, T. M. H., & Nguyen, D. T. (2015). Comparison of some morphological and absorption properties of the nanoparticles Au/TiO2 embedded films prepared by different technologies on the substrates for application in the plasmonic solar cell. *Advances in Natural Sciences: Nanoscience and Nanotechnology*, 6(1), 015018.

Das, A. K., & Raj, C. R. (2010). Facile growth of flower-like Au nanocrystals and electroanalysis of biomolecules. *Journal of Electroanalytical Chemistry*, 638(2), 189-194.

Dash, J. N., & Jha, R. (2016). Temperature insensitive PCF interferometer coated with graphene oxide tip sensor. *IEEE Photonics Technology Letters*, 28(9), 1006-1009.

Degiorgio, V., & Flytzanis, C. (1995). Nonlinear optical materials: *Principles and Applications* (Vol. 126): IOS Press.

Dervos, C. T., Paraskevas, C. D., Skafidas, P. D., & Vassiliou, P. (2005). A complex permittivity based sensor for the electrical characterization of high-voltage transformer oils. *Sensors*, 5(4), 302-316.

Diest, K., Liberman, V., Lennon, D. M., Welander, P. B., & Rothschild, M. (2013). Aluminum plasmonics: optimization of plasmonic properties using liquid-prism-coupled ellipsometry. *Optics Express*, 21(23), 28638-28650.

Dietrich, A. M., Jensen, J. N., & da Costa, W. F. (1996). Chemical species. *Water environment research,* 68(4), 391-406.

Djellali, N., Gozhyk, I., Owens, D., Lozenko, S., Lebental, M., Lautru, J., Zyss, J. (2009). Controlling the directional emission of holey organic microlasers. *Applied Physics Letters,* 95(10), 101108.

Drude, P. (1900a). Zur Elektronentheorie der Metalle. *Annalen der Physik,* 306(3), 566-613.

Drude, P. (1900b). Zur Elektronentheorie der Metalle; II. Teil. Galvanomagnetische und thermomagnetische Effecte. *Annalen der Physik,* 308(11), 369-402.

El-Sherif, M., Bansal, L., & Yuan, J. (2007). Fiber optic sensors for detection of toxic and biological threats. *Sensors,* 7(12), 3100-3118.

Fano, U. (1941). The theory of anomalous diffraction gratings and of quasi-stationary waves on metallic surfaces (Sommerfeld's waves). JOSA, 31(3), 213-222.

Ferguson, J. A., Boles, T. C., Adams, C. P., & Walt, D. R. (1996). A fiber-optic DNA biosensor microarray for the analysis of gene expression. *Nature Biotechnology,* 14(13), 1681-1684.

Freise, A. (2012). Optical Metamaterials: Fundamentals and Applications, by W. Cai and V. Shalaev. *Contemporary Physics,* 53(3), 278-279.

Gao, L., Zhu, T., Deng, M., Chiang, K. S., Sun, X., Dong, X., & Hou, Y. (2012). Long-period fiber grating within D-shaped fiber using magnetic fluid for magnetic-field detection. *IEEE Photonics Journal,* 4(6), 2095-2104.

Gaspar, D., Pimentel, A., Mateus, T., Leitao, J., Soares, J., Falcao, B., Aguas, H. (2013). Influence of the layer thickness in plasmonic gold nanoparticles produced by thermal evaporation. *Scientific Reports*, 3.

Geng, W., Li, N., Li, X., Wang, R., Tu, J., & Zhang, T. (2007). Effect of polymerization time on the humidity sensing properties of polypyrrole. *Sensors and Actuators B: Chemical*, 125(1), 114-119.

Ghoshal, S., Sahar, M., Rohani, M., & Sharma, S. (2011). *Nanophotonics for 21st century Optoelectronics-Devices and Applications:* InTech.

Gibney, E. (2015). 2D OR NOT 2D. *Nature*, 522(7556), 274.

Gramotnev, D. K., & Bozhevolnyi, S. I. (2010). *Plasmonics beyond the diffraction limit. Nature photonics*, 4(2), 83-91.

Gupta, B. D., Shrivastav, A. M., & Usha, S. P. (2016). Surface plasmon resonance-based fiber optic sensors utilizing molecular imprinting. *Sensors*, 16(9), 1381.

Gupta, B. D., & Verma, R. K. (2009). Surface plasmon resonance-based fiber optic sensors: principle, probe designs, and some applications. *Journal of Sensors*, 2009.

Hajakbari, F., & Ensandoust, M. (2016). Study of Thermal Annealing Effect on the Properties of Silver Thin Films Prepared by DC Magnetron Sputtering. *Acta Physica Polonica A*, 129(4), 680-682.

Hamanaka, Y., Hayashi, N., Nakamura, A., & Omi, S. (2000). Dispersion of third-order nonlinear optical susceptibility of silver nanocrystal-glass composites. *Journal of Luminescence*, 87, 859-861.

Han, Y., Ye, H., Wu, W., & Shi, G. (2008). Fabrication of Ag and Cu nanowires by a solid-state ionic method and investigation of their third-order nonlinear optical properties. *Materials Letters*, 62(17), 2806-2809.

Healey, B. G., Li, L., & Walt, D. R. (1997). Multianalyte biosensors on optical imaging bundles. *Biosensors and Bioelectronics*, 12(6), 521-529.

Henari, F. Z. (2001). Optical switching in organometallic phthalocyanine. Journal of Optics A: *Pure and Applied Optics*, 3(3), 188.

Herminghaus, S., Jacobs, K., Mecke, K., Bischof, J., Fery, A., Ibn-Elhaj, M., & Schlagowski, S. (1998). Spinodal dewetting in liquid crystal and liquid metal films. *Science*, 282(5390), 916-919.

Holst, G., & Mizaikoff, B. (2001). Fibre optic sensors for environmental applications'. *Handbook of Optical Fibre Sensing Technology, John Wiley & Sons*, 729-749.

Homola, J. (2003). Present and future of surface plasmon resonance biosensors. *Analytical and Bioanalytical Chemistry*, 377(3), 528-539.

Homola, J. (2006). Surface plasmon resonance based sensors. 2006 - *Springer*, 3-44.

Homola, J., Yee, S. S., & Gauglitz, G. (1999). Surface plasmon resonance sensors. *Sensors and Actuators B*: Chemical, 54(1), 3-15.

Horikoshi, S., & Serpone, N. (2013). Introduction to nanoparticles. Microwaves in Nanoparticle Synthesis: *Fundamentals and Applications*, 1-24.

Hsu, S. L.-C., & Wu, R.-T. (2010a). Preparation of silver nanoparticle with different particle sizes for low-temperature sintering. Int. Proc. Chem. Biol. *Environ. Eng*, 2, 55-58.

Hsu, S. L.-C., & Wu, R.-T. (2010b). Preparation of silver nanoparticle with different particle sizes for low-temperature sintering. *Paper Presented at the International Conference on Nanotechnology Biosensors*. IACSIT Press, Hong Kong.

Hu, E. L., Brongersma, M., & Baca, A. (2011). Applications: nanophotonics and plasmonics Nanotechnology Research Directions for Societal Needs in 2010 *Springer* (pp. 417-444):.

Hu, M., Chen, J., Li, Z.-Y., Au, L., Hartland, G. V., Li, X., Xia., Y. (2006). Gold nanostructures: engineering their plasmonic properties for biomedical applications. *Chemical Society Review*s, 35(11), 1084-1094.

Hulla, J., Sahu, S., & Hayes, A. (2015). Nanotechnology: History and future. *Human & Experimental Toxicology,* 34(12), 1318-1321.

Hummers Jr, W. S., & Offeman, R. E. (1958). Preparation of graphitic oxide. *Journal of the American Chemical Society,* 80(6), 1339-1339.

Huttunen, A., & Törmä, P. (2002). Band structures for nonlinear photonic crystals. *Journal of Applied Physics,* 91(7), 3988-3991.

Iijima, S. (1991). Helical microtubules of graphitic carbon. *Nature,* 354(6348), 56.

Islam, A. M., & Mukherjee, M. (2011). Effect of temperature in synthesis of silver nanoparticles in triblock copolymer micellar solution. *Journal of Experimental Nanoscience,* 6(6), 596-611.

Jiang, X., Chen, W., Chen, C., Xiong, S., & Yu, A. (2011). Role of temperature in the growth of silver nanoparticles through a synergetic reduction approach. *Nanoscale Res Lett,* 6(1), 32.

Jones, H. (1957). Introduction to Solid State Physics by C. Kittel. *Acta Crystallographica,* 10(5), 390.

Jung, I., Dikin, D., Park, S., Cai, W., Mielke, S. L., & Ruoff, R. S. (2008). Effect of water vapor on electrical properties of individual reduced graphene oxide sheets. *The Journal of Physical Chemistry C,* 112(51), 20264-20268.

Kinnan, M. K., & Chumanov, G. (2010). Plasmon Coupling in Two-Dimensional Arrays of Silver Nanoparticles: II. Effect of the Particle Size and Interparticle Distance. *The Journal of Physical Chemistry C,* 114(16), 7496-7501.

Köllensperger, P., Karl, W., Ahmad, M., Pike, W., & Green, M. (2012). Patterning of platinum (Pt) thin films by chemical wet etching in Aqua Regia. *Journal of Micromechanics and Microengineering*, 22(6), 067001.

Kosasih, A. N. (2012). Application of Graphene Oxide in Purple Membrane Chip Technology.

Kovtyukhova, N. I., Ollivier, P. J., Martin, B. R., Mallouk, T. E., Chizhik, S. A., Buzaneva, E. V., & Gorchinskiy, A. D. (1999). Layer-by-layer assembly of ultrathin composite films from micron-sized graphite oxide sheets and polycations. *Chemistry of Materials,* 11(3), 771-778.

Kreibig, U., & Genzel, L. (1985). Optical absorption of small metallic particles. *Surface Science,* 156, Part 2(0), 678-700.

Kreibig, U., & Volmer, M. (1995). Optical properties of metal clusters: *Springer*.

Kretschmann, E. (1971). Die bestimmung optischer konstanten von metallen durch anregung von oberflächenplasmaschwingungen. *Zeitschrift Für Physik*, 241(4), 313-324.

Kretschmann, E., & Raether, H. (1968). Radiative decay of non radiative surface plasmons excited by light. Zeitschrift für Naturforschung A, 23(12), 2135-2136.

Kretschmann, E., & Raether, H. (1968). Radiative decay of nonradiative surface plasmons excited by light. *Z. Naturforsch. A,* 23, 2135.

Krishna, H., Sachan, R., Strader, J., Favazza, C., Khenner, M., & Kalyanaraman, R. (2010). Thickness-dependent spontaneous dewetting morphology of ultrathin Ag films. *Nanotechnology,* 21(15), 155601.

Kumar, H. V., Woltornist, S. J., & Adamson, D. H. (2016). Fractionation and characterization of graphene oxide by oxidation extent through emulsion stabilization. *Carbon*, 98, 491-495.

Kumar, R. S. S., Rao, S. V., Giribabu, L., & Rao, D. N. (2008). Nonlinear optical properties of alkyl phthalocyanines in the femtosecond, nanosecond, and cw excitation regimes. *Paper presented at the Lasers and Applications in Science and Engineering.*

Lalanne, P., & Liu, H. (2013). Waves on subwalength metallic surfaces: a microscopic view point Plasmonics: *Theory and Applications* (pp. 379-399): *Springer*.

Langhammer, C., Yuan, Z., Zorić, I., & Kasemo, B. (2006). Plasmonic properties of supported Pt and Pd nanostructures. *Nano letters*, 6(4), 833-838.

Langmuir, I. (1928). Oscillations in Ionized Gases. *Proceedings of the National Academy of Sciences*, 14(8), 627-637.

Laskar, S., & Bordoloi, S. (2013). Monitoring of moisture in transformer oil using optical fiber as sensor. *Journal of Photonics*, 2013.

Lee, S.-W., Chang, S.-H., Lai, Y.-S., Lin, C.-C., Tsai, C.-M., Lee, Y.-C., Huang, C.-L. (2014). Effect of temperature on the growth of silver nanoparticles using plasmon-mediated method under the irradiation of green LEDs. *Materials*, 7(12), 7781-7798.

Lewand, L. (2002b). Understanding water in transformer systems. *InterNational Electrical Testing Association.*

Liedberg, B., Nylander, C., & Lundström, I. (1995). Biosensing with surface plasmon resonance—how it all started. *Biosensors and Bioelectronics*, 10(8), i-ix.

Liedberg, B., Nylander, C., & Lunström, I. (1983). Surface plasmon resonance for gas detection and biosensing. *Sensors and Actuators, 4, 299-304.*

Link, S., & El-Sayed, M. A. (1999). Spectral Properties and Relaxation Dynamics of Surface Plasmon Electronic Oscillations in Gold and Silver Nanodots and Nanorods. *The Journal of Physical Chemistry B, 103(40), 8410-8426.*

Lipatov, A., Varezhnikov, A., Wilson, P., Sysoev, V., Kolmakov, A., & Sinitskii, A. (2013). Highly selective gas sensor arrays based on thermally reduced graphene oxide. *Nanoscale, 5(12), 5426-5434.*

Liu, Z., Tian, Z. Q., & Jiang, S. P. (2006). Synthesis and characterization of Nafion-stabilized Pt nanoparticles for polymer electrolyte fuel cells. *Electrochimica Acta, 52(3), 1213-1220.*

Lundström, I. (2014). From a laboratory exercise for students to a pioneering biosensing technology. *Plasmonics, 9(4), 741-751.*

Luo, Y.-T., Wang, H.-B., Ma, G.-M., Song, H.-T., Li, C., & Jiang, J. (2016). Research on high sensitive D-shaped FBG hydrogen sensors in power transformer oil. *Sensors, 16(10), 1641.*

Luong, J. H., Male, K. B., & Glennon, J. D. (2008). Biosensor technology: technology push versus market pull. *Biotechnology Advances, 26(5), 492-500.*

Mahanta, D. K., & Laskar, S. (2016). Transformer Condition Monitoring using Fiber Optic Sensors: A Review. *ADBU Journal of Engineering Technology, 4.*

Mahanta, D. K., & Laskar, S. (2017). Water quantity based quality measurement of transformer oil using polymer optical fiber as sensor. *IEEE Sensors Journal.*

Maier, S. (2007). Plasmonics fundamentals and applications. Plasmonics: *Fundamentals and Applications.*

Maier, S. A. (2007). Excitation of Surface Plasmon Polaritons at Planar Interfaces. Plasmonics: *Fundamentals and Applications*, 39-52.

Maier, S. A. (2007). Plasmonics: *fundamentals and applications:* Springer Science & Business Media.

Majdabadi, A., Gaeeni, M. R., Ghamsari, M. S., & Majles-Ara, M. H. (2015). Investigation of stability and nonlinear optical properties CdSe colloidal nanocrystals. *Journal of Laser Applications*, 27(2), 022010.

Mak, K. F., Ju, L., Wang, F., & Heinz, T. F. (2012). Optical spectroscopy of graphene: from the far infrared to the ultraviolet. *Solid State Communications*, 152(15), 1341-1349.

Mandal, A., & Chaudhuri, P. (2013). Contribution of higher order plasmonic modes on optical absorption enhancement in amorphous silicon thin films. Optics Communications, 300, 77-84.

Mao, Y., Bao, Y., Wang, W., Li, Z., Li, F., & Niu, L. (2011). Development and Application of Time-Resolved Surface Plasmon Resonance Spectrometer. *American Journal of Analytical Chemistry*, 2(05), 589.

Marcano, D. C., Kosynkin, D. V., Berlin, J. M., Sinitskii, A., Sun, Z., Slesarev, A., . . . Tour, J. M. (2010). Improved synthesis of graphene oxide. *ACS Nano*, , 4 (8), pp 4806–4814

Mathew, J. (2013). Development of Novel Fiber Optic Humidity Sensors and Their Derived Applications. thesis submite Dublin Institute of Technology.

Mezher, M., Chong, W., & Zakaria, R. (2016a). Nonlinear optical response of platinum nanostructures and application for water detection in transformer oil. *RSC Advances*, 6(106), 104624-104631.

Mezher, M., Chong, W., & Zakaria, R. (2016b). Third-order optical nonlinearity studies of bilayer Au/Ag metallic films. *Laser Physics*, 26(5), 055401.

Mezher, M., Nady, A., Penny, R., Chong, W., & Zakaria, R. (2015). Z-scan studies of the nonlinear optical properties of gold nanoparticles prepared by electron beam deposition. *Applied Qptics*, 54(33), 9703-9708.

Michalak, W. D., Miller, J. B., Yolcu, C., & Gellman, A. J. (2012). Fabrication of metallic nanoparticles by spinodal dewetting of thin films: A high-throughput approach. *Thin Solid Films*, 522, 473-479.

Ming, H. N. (2010). Simple room-temperature preparation of high-yield large-area graphene oxide. *International Journal of Nanomedicine*, 6.

Mizaikoff, B., Taga, K., & Kellner, R. (1995). Infrared fiber optic gas sensor for chlorofluorohydrocarbons. *Vibrational Spectroscopy*, 8(2), 103-108.

Mubeen, S., Zhang, S., Kim, N., Lee, S., Krämer, S., Xu, H., & Moskovits, M. (2012). Plasmonic properties of gold nanoparticles separated from a gold mirror by an ultrathin oxide. *Nano Letters*, 12(4), 2088-2094.

Mulvaney, P. (1996). Surface Plasmon Spectroscopy of Nanosized Metal Particles. *Langmuir*, 12(3), 788-800.

Murray, W. A., & Barnes, W. L. (2007). Plasmonic Materials. *Advanced Materials*, 19(22), 3771-3782.

Nair, R., Wu, H., Jayaram, P., Grigorieva, I., & Geim, A. (2012). Unimpeded permeation of water through helium-leak–tight graphene-based membranes. *Science*, 335(6067), 442-444.

Neethling, P. (2005). *Determining non-linear OpticalPproperties using the Z-scan Technique. Stellenbosch:* University of Stellenbosch.

Nguyen, H. H. (2012). *Optical Fibre Surface Plasmon Resonance Sensors based on a Metallic Array of Sub-Wavelength apertures.* Victoria University.

Norazlina, H., & Kamal, Y. (2015). Graphene modifications in polylactic acid nanocomposites: a review. *Polymer Bulletin*, 72(4), 931-961.

Norton, K. (1937). The physical reality of space and surface waves in the radiation field of radio antennas. *Proceedings of the Institute of Radio Engineers*, 25(9), 1192-1202.

Novoselov, S. (2010). The Nobel Prize in Physics 2010 honours two scientists, who have made the decisive contributions to this development. They are Andre K. Geim and Konstantin S. Novoselov, both at the University of Manchester, UK. They have succeeded in producing, isolating, identifying and characterizing graphene.

Otto, A. (1968). Excitation of nonradiative surface plasma waves in silver by the method of frustrated total reflection. *Z. Physik*, 216, 398.

Otto, A. (1968). Excitation of nonradiative surface plasma waves in silver by the method of frustrated total reflection. *Zeitschrift Für Physik*, 216(4), 398-410.

Otto, A. (1968). A new method for exciting non-radioactive surface plasma oscillations. *phys. Stat.* sol, 26, K99-K101.

Owens, D. T., Fuentes-Hernandez, C., Hales, J. M., Perry, J. W., & Kippelen, B. (2010). A comprehensive analysis of the contributions to the nonlinear optical properties of thin Ag films. *Journal of Applied physics*, 107(12), 123114.

Ozbay, E. (2006). Plasmonics: Merging Photonics and Electronics at Nanoscale Dimensions. *Science*, 311(5758), 189-193.

Patnaik, A., Senthilnathan, K., & Jha, R. (2015). Graphene-based conducting metal oxide coated D-shaped optical fiber SPR sensor. *IEEE Photonics Technology Letters*, 27(23), 2437-2440.

Piñero, S., Camero, S., & Blanco, S. (2017). Silver nanoparticles: Influence of the temperature synthesis on the particles' morphology. Paper presented at the *Journal of Physics:* Conference Series.

Powell, C., & Swan, J. (1960). Effect of oxidation on the characteristic loss spectra of aluminum and magnesium. *Physical Review*, 118(3), 640.

Pris, M. (2014). *Influence of different parameters on wet synthesis of silver nanoparticles*. University of Twente.

Qadir, R. W., Ahmad, Z., & Sulaiman, K. (2014). Effect of the shapes of nanostructures on the light absorption in organic thin films. *Journal of Modern Optics*, 61(8), 636-640.

Qazi, H. H., Mohammad, A. B., Ahmad, H., & Zulkifli, M. Z. (2016). D-Shaped Polarization Maintaining Fiber Sensor for Strain and Temperature Monitoring. *Sensors*, 16(9), 1505.

Quidant, R., Zelenina, A. S., & Nieto-Vesperinas, M. (2007). Optical manipulation of plasmonic nanoparticles. *Applied Physics A*, 89(2), 233-239.

Rani, S., Kumar, M., Garg, R., Sharma, S., & Kumar, D. (2016). Amide Functionalized Graphene Oxide Thin Films for Hydrogen Sulfide Gas Sensing Applications. *IEEE Sens.* J, 16, 2929-2934.

Ritchie, R. H. (1957). Plasma Losses by Fast Electrons in Thin Films. *Physical Review*, 106(5), 874-881.

Romer, P. (1993). Idea gaps and object gaps in economic development. *Journal of Monetary Economics*, 32(3), 543-573.

Rukshan Fernando, F. S., and Priyalal Wijewarnasuriya. (2012). Altering Plasmonic Nanoparticle Size Through Thermal Annealing for Improved Photovoltaic Devices.

Sabuktagin, M. S., Hamdan, K. S., Sulaiman, K., Zakaria, R., & Ahmad, H. (2014). Long Wavelength Plasmonic Absorption Enhancement in Silicon Using Optical Lithography Compatible Core-Shell-Type Nanowires. *International Journal of Photoenergy*, 2014, 6.

Sargent Jr, J. F. (2016). Nanotechnology: a policy primer.

Sattler, K. D. (2010). Handbook of nanophysics: *principles and methods*: CRC press.

Scalora, M., Dowling, J. P., Bowden, C. M., & Bloemer, M. J. (1994). Optical limiting and switching of ultrashort pulses in nonlinear photonic band gap materials. *Physical ReviewLletters*, 73(10), 1368.

Schweizer, G., Latka, I., Lehmann, H., & Willsch, R. (1997). Optical sensing of hydrocarbons in air or in water using UV absorption in the evanescent field of fibers. *Sensors and Actuators B: Chemical*, 38(1-3), 150-153.

Sharma, A. K., Jha, R., & Gupta, B. (2007). Fiber-optic sensors based on surface plasmon resonance: a comprehensive review. *IEEE Sensors Journal*, 7(8), 1118-1129.

Sherry, L. J., Chang, S.-H., Schatz, G. C., Van Duyne, R. P., Wiley, B. J., & Xia, Y. (2005). Localized Surface Plasmon Resonance Spectroscopy of Single Silver Nanocubes. *Nano Letters*, 5(10), 2034-2038.

Singh, V., & Aghamkar, P. (2014). Surface plasmon enhanced third-order optical nonlinearity of Ag nanocomposite film. *Applied Physics Letters*, 104(11), 111112.

Soljačić, M., Ibanescu, M., Johnson, S. G., Fink, Y., & Joannopoulos, J. (2002). Optimal bistable switching in nonlinear photonic crystals. *Physical Review E*, 66(5), 055601.

Sommerfeld, A. (1909). Propagation of waves in wireless telegraphy. *Ann. Phys*, 28(3), 665-736.

Sommerfeld, A. (1952). PART I - fundamentals and basic principles of maxwell's electrodynamics *Electrodynamics* (pp. 1-54): Academic Press.

Sparling, B., & Aubin, J. (2007). Assessing Water Content in Insulating Paper of Power Transformers. *Electric Energy Online, July/August.*

Staudenmaier, L. (1898). Verfahren zur darstellung der graphitsäure. *European Journal of Inorganic Chemistry*, 31(2), 1481-1487.

Stern, E., & Ferrell, R. (1960). Surface plasma oscillations of a degenerate electron gas. *Physical Review*, 120(1), 130.

Stewart, G., Jin, W., & Culshaw, B. (1997). Prospects for fibre-optic evanescent-field gas sensors using absorption in the near-infrared. *Sensors and Actuators B: Chemical*, 38(1-3), 42-47.

Strobel, S., Kirkendall, C., Chang, J.-B., & Berggren, K. K. (2010). Sub-10 nm structures on silicon by thermal dewetting of platinum. *Nanotechnology*, 21(50), 505301.

Sukharev, M., & Nitzan, A. (2017). Topical Review: optics of exciton-plasmon nanomaterials. *arXiv preprint arXiv*:1704.05605.

Suresh, S., Ramanand, A., Jayaraman, D., & Mani, P. (2012). Review on theoretical aspect of nonlinear optics. *Rev. Adv. Mater.* Sci, 30, 175-183.

Suwarno, M (2015). Effects of Water Content on Dielectric Properties of Mineral Transformer Oil. *World Academy of Science Engineering and Technology International Journal of Electrical and Computer Engineering*. vol:10, no 10.

Toriumi, M., Yanagimachi, M., & Masuhara, H. (1992). Absorption effects on total-internal-reflection fluorescence spectroscopy. *Applied Optics*, 31(30), 6376-6382.

Tran, P. (1996). Optical switching with a nonlinear photonic crystal: a numerical study. *Optics Letters*, 21(15), 1138-1140.

Van Stryland, E., Sheik-Bahae, M., Said, A., & Hagan, D. (1993). *Characterization of nonlinear optical absorption and refraction. Progress in crystal growth and characterization of materials*, 27(3-4), 279-311.

Van Stryland, E. W., & Sheik-Bahae, M. (1998). Z-scan measurements of optical nonlinearities. *Characterization techniques and tabulations for organic nonlinear materials*, 18(3), 655-692.

Villuendas, F., & Pelayo, J. (1990). Optical fibre device for chemical seming based on surface plasmon excitridon. Sensors and Actuators *A: Physical*, 23(1-3), 1142-1145.

Vivacqua, M., Espinosa, D., & Martins Figueiredo Neto, A. (2012). Application of the Z-scan technique to determine the optical Kerr coefficient and two-photon absorption coefficient of magnetite nanoparticles colloidal suspension. *Journal of Applied Physics*, 111(11), 113509.

Wang, D., Ji, R., & Schaaf, P. (2011). Formation of precise 2D Au particle arrays via thermally induced dewetting on pre-patterned substrates. *Beilstein Journal of Nanotechnology*, 2, 318.

Wei, N., Peng, X., & Xu, Z. (2014). Understanding water permeation in graphene oxide membranes. *ACS Applied Materials & Interfaces*, 6(8), 5877-5883.

Wolfbeis, O. S. (2004). Fiber-optic chemical sensors and biosensors. *Analytical Chemistry*, 76(12), 3269-3284.

Wood, R. W. (1902). On a remarkable case of uneven distribution of light in a diffraction grating spectrum. *Proceedings of the Physical Society of London,* 18(1), 269.

Xia, F., Wang, H., Xiao, D., Dubey, M., & Ramasubramaniam, A. (2014). Two-dimensional material nanophotonics. *Nature Photonics*, 8(12), 899-907.

Xia, F., Yan, H., & Avouris, P. (2013). The interaction of light and graphene: basics, devices, and applications. *Proceedings of the IEEE,* 101(7), 1717-1731.

Yanase, Y., Hiragun, T., Ishii, K., Kawaguchi, T., Yanase, T., Kawai, M., . . . Hide, M. (2014). Surface plasmon resonance for cell-based clinical diagnosis. *Sensors,* 14(3), 4948-4959.

Yang, G., Guan, D., Wang, W., Wu, W., & Chen, Z. (2004). The inherent optical nonlinearities of thin silver films. *Optical Materials,* 25(4), 439-443.

Yang, X., Liu, H., Zhao, H., Zhang, X., Liang, X., & Xiang, W. (2011). Fabrication and third-order optical nonlinearities of Na 2 O–B 2 O 3–SiO 2 glasses containing metallic Bi, Bi 2 O 3 and Bi 2 S 3 crystals. *Materials Chemistry and Physics,* 129(1), 121-129.

Yavari, F., Kritzinger, C., Gaire, C., Song, L., Gulapalli, H., Borca-Tasciuc, T., . . . Koratkar, N. (2010). Tunable bandgap in graphene by the controlled adsorption of water molecules. *Small,* 6(22), 2535-2538.

You, S., Luzan, S. M., Szabó, T., & Talyzin, A. V. (2013). Effect of synthesis method on solvation and exfoliation of graphite oxide. *Carbon*, 52, 171-180.

Zakaria, R., Mezher, M., & Chong, W. (2016a). Investigation of nonlinear optical properties on structures of silver micro-flowers. *Applied Physics A,* 122(7), 1-7.

Zakaria, R., Mezher, M., & Chong, W. (2016b). Investigation of nonlinear optical properties on structures of silver micro-flowers. *Applied Physics A,* 122(7), 664.

Zenneck, J. (1907). Über die Fortpflanzung ebener elektromagnetischer Wellen längs einer ebenen Leiterfläche und ihre Beziehung zur drahtlosen Telegraphie. *Annalen der Physik*, 328(10), 846-866.

Zhang, D., Tong, J., & Xia, B. (2014). Humidity-sensing properties of chemically reduced graphene oxide/polymer nanocomposite film sensor based on layer-by-layer nano self-assembly. *Sensors and Actuators B: Chemical*, 197, 66-72.

Zhang, F., Wang, Z., Wang, D., Wu, Z., Wang, S., & Xu, X. (2016). Nonlinear optical effects in nitrogen-doped graphene. *RSC Advances*, 6(5), 3526-3531.

Zhang, Z., & Ewing, G. E. (2002). Attenuated partial internal reflection infrared spectroscopy. *Analytical Chemistry*, 74(11), 2578-2583.

Zynio, S. A., Samoylov, A. V., Surovtseva, E. R., Mirsky, V. M., & Shirshov, Y. M. (2002). Bimetallic layers increase sensitivity of affinity sensors based on surface plasmon resonance. *Sensors*, 2(2), 62-70.

LIST OF PUBLICATIONS AND PAPERS PRESENTED

1. Mezher, M., et al., Z-scan studies of the nonlinear optical properties of gold nanoparticles prepared by electron beam deposition. *Applied Optics,* 2015. 54(33): p. 9703-9708.
2. Mezher, M., W. Chong, and R. Zakaria, Third-order optical nonlinearity studies of bilayer Au/Ag metallic films. *Laser Physics,* 2016. 26(5): p. 055401.
3. Zakaria, R., M. Mezher, and W. Chong, Investigation of nonlinear optical properties on structures of silver micro-flowers. *Applied Physics* A, 2016. 122(7): p. 664.
4. Mezher, M., W. Chong, and R. Zakaria, Nonlinear optical response of platinum nanostructures and application for water detection in transformer oil. *RSC Advances,* 2016. 6(106): p. 104624-104631.
5. S. F. A. Z. Yusoff, M. H. Mezher, I. S. Amiri, N. Ayyanar, D. Vigneswaran, H. Ahmad, R. Zakaria (2018). Detection Of Moisture Content In Transformer Oil Using Platinum Coated On D-shaped Optical Fiber. *Optical Fiber Technology*. (Accepted)

Conferences Attended

1. M. H. Mezher, W. Y. Chong, and *R. Zakaria, “Investigation of the third order nonlinear optics response on plasmonic structure” Graphene Malaysia 2017, Kuala Lumpur (10 July 2017)